University of West Bohemia
Faculty of Applied Sciences
Department of Physics

Hard alloy films with enhanced resistance to cracking

Ing. Zuzana Čiperová

A thesis submitted for the degree of Doctor of Philosophy in the field of Plasma Physics and Physics of Thin Films

Supervisor: prof. Ing. Jindřich Musil, DrSc.

Plzeň 2021

Západočeská univerzita v Plzni
Fakulta aplikovaných věd
Katedra fyziky

Tvrdé slitinové vrstvy se zvýšenou odolností proti vzniku trhlin

Ing. Zuzana Čiperová

Dizertační práce k získání akademického titulu doktor v oboru Fyzika plazmatu a tenkých vrstev

Školitel: prof. Ing. Jindřich Musil, DrSc.

Plzeň 2021

PREFACE

The thesis is submitted for the degree of Doctor of Philosophy at the University of West Bohemia. I hereby declare that the entire thesis was written by myself using results obtained during my Ph.D. study and the duly cited literature.

My contribution to the presented results and submitted scientific papers published in impacted international journals consists of:

- active participation in the design of the experiments;
- depositing of all the samples together with the necessary measurements of the plasma characteristics;
- analysis of the films – specifically the measurement of the thickness, mechanical properties, resistance to cracking, electrical resistivity and elemental composition;
- active participation in the interpretation of the results;
- active participation in writing the papers including the creation of the figures.

The results included in the thesis were obtained during my Ph.D. study at the Department of Physics and NTIS, European Centre of Excellence, University of West Bohemia, since September 2016. The research was financially supported by the projects SGS–2016–056 (2016 – 2018): New nanostructured thin-film materials formed by plasma technologies, SGS–2019–031 (2019 – 2021): New thin-film materials formed by advanced plasma technologies, and LO1506: Sustainability support of the centre NTIS – New Technologies for the Information Society.

Plzeň, 29/04/2021 Ing. Zuzana Čiperová

ACKNOWLEDGEMENTS

I would like to express my sincere gratitude to my supervisor prof. Ing. Jindřich Musil, DrSc. for the guidance during my study. I appreciate his unsurpassed knowledge and am thankful for all the valuable advice.

My great thanks also belong to prof. RNDr. Jaroslav Vlček, CSc. for his excellent management of the Department of Physics. The friendly atmosphere which he managed to create here was very helpful during all my studies and therefore I would like to also thank all my colleagues not only for the significant help with my research but for the numerous worthwhile discussions as well – special credit belongs to doc. Mgr. Šimon Kos, Ph.D. who helped me not only with the comprehension of the obtained results.

Last but not least, I greatly appreciate all the support of my family and friends.

TABLE OF CONTENTS

1 Introduction 7
2 State of the Art 8
2.1 Magnetron sputtering 8
2.1.1 Dual magnetron system 10
2.2 Film growth 12
2.2.1 Structural zone diagrams 13
2.2.2 Phase diagrams 16
2.3 Thin films with enhanced hardness and resistance to cracking 23
2.3.1 Enhanced hardness 23
2.3.2 Enhanced resistance to cracking 24
2.3.3 The energy delivered to the growing film 25
2.3.4 Hard and flexible alloy films 27
3 Aims of the Thesis 29
4 Experimental Details 30
4.1 Deposition system 30
4.1.1 Deposition chamber 30
4.1.2 Pumping system 31
4.1.3 Power supplies 32
4.2 Substrate preparation 33
4.3 Thin-film characterization 34
4.3.1 Thickness, deposition rate, macrostress 34
4.3.2 Mechanical properties 35
4.3.3 Resistance to cracking 37
4.3.4 Electrical resistivity 38
4.3.5 Structure and phase composition 39
4.3.6 Elemental composition 40
4.3.7 Surface morphology and cross-sections 40
4.4 Deposition conditions 40
4.4.1 Zr-Si films 40
4.4.2 Mg, Si, Mg-Si, Mg-Si-N and Si-N films 41
5 Results and Discussion 44
5.1 Flexible hard Zr-Si alloy films prepared by magnetron sputtering 45
5.1.1 Results and discussion 45

5.1.2 Conclusions 53
5.2 Magnetron sputtering of Mg-Si alloy films and Mg-Si-N nitride films 55
5.2.1 Results and discussion...55
5.2.2 Conclusions 66
5.3 Physical and mechanical properties of SiN_x nitride films prepared by magnetron sputtering 67
5.3.1 Results and discussion...67
5.3.2 Conclusions 74
5.4 Effect of melting temperature T_m on properties of hard alloy coatings resistant to cracking 75
5.4.1 Microstructure vs. pressure p, homologous temperature T_S/T_m and energy $\mathcal{E}_{bi}$..75
5.4.2 Melting temperature T_m vs. elemental composition of binary alloys.................77
5.4.3 Effect of T_m on the coating properties and its experimental demonstration 79
5.4.4 Effect of homologous temperature T_S/T_m of sputtered Zr-Si alloy coatings.......80
5.4.5 Effect of the elemental composition of sputtered Mg-Si-N alloy coatings.........81
5.4.6 The microstructure of sputtered Mg coating from a melted coating material.....85
5.4.7 Conclusions 87
6 Conclusions 89
References 92
List of the author's publications..105
Papers in international journals 105
Participation at international conferences 105
Oral presentations at international conferences 105
Poster presentations at international conferences 106
Abstract 107
Anotace 109

1 INTRODUCTION

Searching for new types of materials allowing application in a wide area of interest has been a great task for centuries. Ever since the first tools were invented, people have been yearning to make them better and better. Many methods and processes have been developed, improved, forgotten and again remembered, upgraded and perfected. Although the trends are changing, e.g. more demands are placed on environmental impacts, the desire is still the same – to be able to produce materials with advanced properties using an optimum process.

An interesting idea is not to tune the bulk material but to improve only its surface so it exhibits the required properties regardless of the behaviour of the whole object. It was shown that a very thin layer of material can effectively improve the properties and quality of the examined sample. Even though the thin-film technology is being called a modern method which has been spread in the last decades, the fact is that golden coatings thinner than 300 nm have been found in the Old Egyptian ancient tombs built more than 5000 years ago. There exist even older examples of thin films but a lot of them were probably made accidentally.

However, the development of vacuum technology, which is crucial in the evolution of thin-film technology, is traced to the 17th century and sputter deposition was first reported in the early 1800s. And it has underwent a long journey to get to the processes similar to the ones being used today.

A tremendous number of various types of coatings can be prepared. Optical coatings only several nanometres thick, smart films changing their properties in a response to some outer effect, nanocomponents for use in integrated circuits – these are only a few examples of thin films which can be produced depending on the method and desired properties.

Hard alloy films with enhanced resistance to cracking are the objective of this thesis. Alloy films can exhibit very interesting properties; however, one of their great drawbacks is their softness and brittleness. Hard films with enhanced resistance to cracking can be used as protective layers on various surfaces such as cutting tools, displays on electronic devices etc. when the hardness is combined with other useful properties. The thesis gives a detailed study of the magnetron sputtering of hard alloy films and the examples of deposition conditions and properties of prepared films.

2 STATE OF THE ART

In this chapter, the basic knowledge important for the context of the thesis is summarized. The first part 2.1 gives a brief insight into the technique of magnetron sputtering; here the dual magnetron system is described in more detail since it is the system used for the preparation of the films presented in this thesis. The second part 2.2 deals with the basics of film growth. Two subsections explain the importance and use of structural zone diagrams (Section 2.2.1) and phase diagrams (Section 2.2.2) since both of these kinds of diagrams are very important for the evaluation of the films investigated in the present thesis (see Chapter 5). The third part 2.3 introduces the main aim of the thesis which are the hard alloy films with enhanced resistance to cracking. Subsection 2.3.1 is therefore devoted to the enhanced hardness, Subsection 2.3.2 is devoted to the enhanced resistance to cracking, Subsection 2.3.3 presents the energy delivered to the growing film and its influence on the film properties since, as will be shown, this is a crucial parameter to control the film properties, and Subsection 2.3.4 gives a brief state of the art of hard and flexible alloy films.

2.1 Magnetron sputtering

Magnetron sputtering is one of the techniques possible to use for thin film deposition. It is classified as a physical method (Physical Vapor Deposition). The fast development of this process was launched by the invention of the planar magnetron by Chapin [1] which rapidly increased the low deposition rate of the conventional diode sputtering systems. For the first time, the magnetic field was used to elongate the trajectories of the electrons in the cathode area which dramatically increased the probability of ionization of the process gas. Industrial and practical demands quickly led to further progress, for example, the introduction of various reactive gases into the deposition chamber [2], [3]; magnetic field configuration (e.g. balanced – unbalanced, closed – mirror) [3], [4]; usage of different types of power supplies (pulsed, AC, HiPIMS) [5]–[7]; geometry and number of magnetrons [3], [8]; and also the combined techniques (e.g. ECR CVD, cathodic arc evaporation, sputtering pulsed laser deposition or cluster gun technique) [9]–[12].

Nowadays, magnetron sputtering and its modifications are used in many practical applications such as hard protective coatings [13], [14], energy conversion [15], optical filters [16], decorative coatings [17] or microelectronics [18]–[20].

The basic principle of magnetron sputtering is the sputtering of the target material (the cathode) by a flux of highly energetic ions from plasma and consequent condensation of the sputtered atoms of the target material onto a substrate (an anode). The ions dispose of very high energy, especially in the cathode sheath since almost the whole voltage drop between the cathode and the plasma potential lies in the cathode sheath. Besides the target atoms, also the secondary electrons are being generated during the sputtering process, and these have a crucial role in sustaining the discharge because they ionize further neutrals.

In a typical sputtering process, the deposition chamber is first evacuated to a high vacuum to eliminate the contamination from the residual background gases. After that, the chamber is filled with a process gas (usually argon). To initiate plasma discharge, high voltage is applied between the cathode and the anode. This low-temperature plasma contains neutral and charged particles both in the ground and excited states. A low degree of ionization (~ 1%) and a state out of the thermodynamics equilibrium are typical for the plasma.

The magnetic field plays an important role in a magnetron sputtering process. Two permanent magnets are placed under the target – so-called inner and outer magnets since both are ring-shaped. They create a magnetic field of a half-toroid shape above the target. Due to the electric field, the electrons being present in the plasma are accelerated away from the cathode surface causing collisions with nearby atoms of the sputtering gas. Due to the magnetic field, the electrons are confined at or near the surface of the target. The most intensive sputtering can be observed in the areas where the magnetic field is parallel to the target surface. This area is called the erosion zone.

The magnetic field can be conventional ("balanced") or unbalanced as can be seen in Figure 2-1. In an unbalanced magnetron (being used for the experiments presented in this thesis), the outer magnet is strengthened relative to the inner pole. Therefore, not all the field lines are closed between the inner and outer poles in the magnetrons, but some are directed towards the substrate. Moreover, some of the secondary electrons can follow the lines, and consequently, the plasma flows out towards the substrate and the high ion currents can be extracted from the plasma without the need to externally bias the substrate [21].

Magnetron sputtering can be also divided according to the sputtering atmosphere. If only an inert process gas (usually argon) is present, the process is called a non-reactive sputtering. It is possible to add a reactive gas (e.g. oxygen, nitrogen) to deposit compound

films such as oxides or nitrides. Then the process is called reactive magnetron sputtering [4].

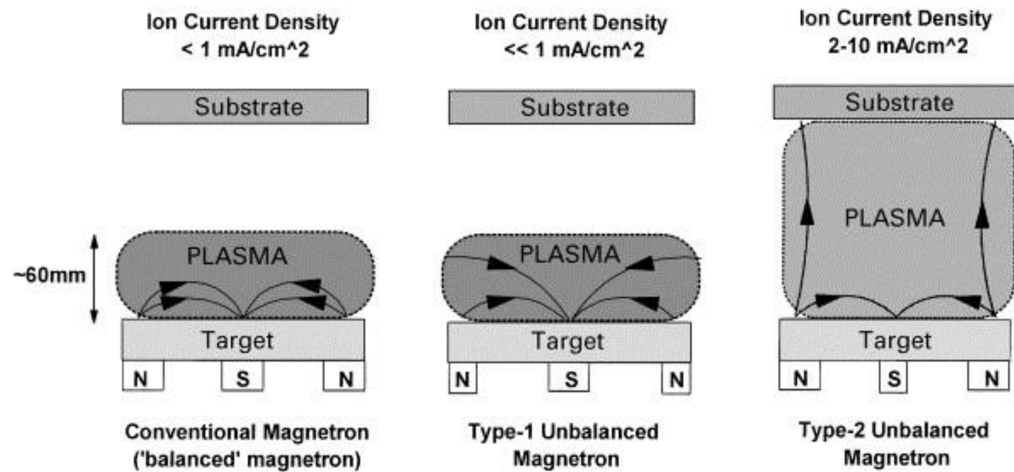

Figure 2-1: Schematic representation of the plasma confinement observed in conventional and unbalanced magnetrons [21].

2.1.1 Dual magnetron system

For many reasons (some of them will be stated further), the configuration of the deposition system with two magnetrons has been frequently used recently. A typical system with a dual magnetron consists of two magnetrons connected to outputs of a power supply (pulsed DC or AC). A schematic diagram of symmetric bipolar pulsed dual magnetron sputtering is shown in Figure 2-2.

The dual magnetron system has numerous advantages. One of them is the elimination of the problem with the disappearing of the anode, which is a common drawback in the reactive sputter deposition, simply by using a pulsed voltage signal. When negative discharge voltage U_d is applied, the magnetron acts as a cathode and the target material is being sputtered while when positive discharge voltage U_d is applied, the magnetron takes the role of an anode and the insulating layer on the surface of the uneroded target area is being removed by the electron bombardment. This is changing periodically according to the pulse length [3], [22]. Using two magnetrons instead of one also enables the increase of the deposition rate, and the elemental composition can be controlled simply by equipping the magnetrons with different target materials and by changing the power target density and the lengths of pulses of each magneton. Another advantage of the dual magnetron system is the elimination of arcing: If the positive charge accumulated on the target surface

is discharged before reaching a critical value at which the electric field across the insulating layer exceeds its dielectric strength. This can be reached only in the case when the frequency of discharging f_r is higher than a critical frequency f_{cr} [3].

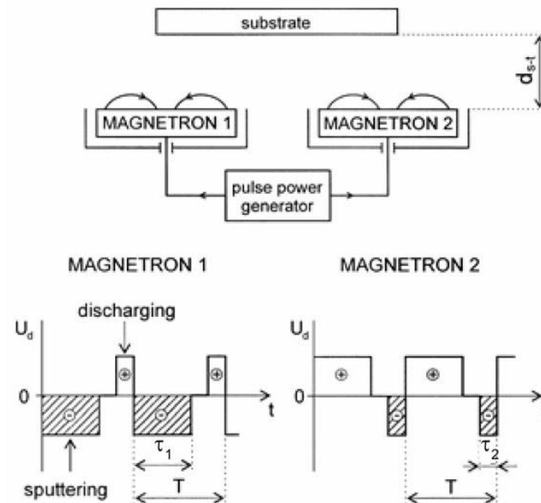

Figure 2-2: Schematic diagram of symmetric bipolar pulsed dual magnetron sputtering [3]. Here d_{s-t} is the substrate-to-target distance, U_d is the discharge voltage, T is the pulse length, and τ_1 and τ_2 are the pulse lengths (the time when magnetron 1 or magnetron 2, respectively, is on).

Some of the other important parameters in the dual magnetron system are: polarities of the magnets, substrate-to-target distance and an angle under which the magnetrons are tilted to the chamber. The magnetic field configuration can be either mirror when the polarities of the inner and outer magnets are the same in both magnetrons or closed when the inner magnets of both magnetrons have the opposite polarity and the outer magnets as well, as can be seen in Figure 2-3.

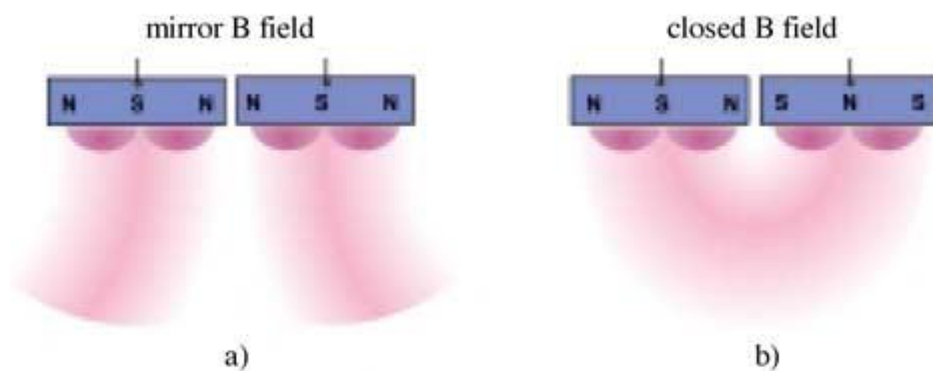

Figure 2-3: Schematic of discharges and polarity of magnets in the dual magnetron operated with (a) mirror B field and (b) closed B field [23].

The dual magnetron system can be either grounded or floating depending on the particular power supply and its connection to the system. In the grounded configuration, the power supply is electrically connected to the chamber and the electric current may flow onto the walls of the chamber or onto the magnetron which currently acts as an anode. In the floating configuration, only the magnetron, that is off, represents the anode of the system.

2.2 Film growth

When a clean substrate is exposed to a flux of the sputtered atoms, a film starts to grow on it. Not all the atoms sputtered from the surface target condense on the substrate. Some of them bounce from the surface of the substrate, some are incorporated into the substrate, and some of them are lost to the walls of the deposition chamber. The angle of the flux of the atoms is influenced mostly by the system geometry, and their energy is influenced e.g. by the sputtering gas pressure (number of collisions) or by target material constants (sputtering yield) and has to be controlled by adequate and complex deposition conditions settings, as will be described in the further sections.

The incoming atoms with proper energies form chemical bonds with the atoms on the surface of the substrate. First of all, an interface between the substrate and the film is formed, which is important for good adhesion. Three types of interfaces can be distinguished: coherent or partially coherent interfaces with a "boundary phase" and interaction-free interfaces [24]. The first one is characterized by a low energy of the interface. Metallic films and compound films containing metals (such as nitrides, carbides, or borides of the transition metals) deposited on metal substrates usually possess such interfaces. The low-energy interface between such materials results in good adhesion. On the other hand, a combination of, for example, metal and ceramic materials usually leads to a high-energy interface and therefore to poor adhesion.

The crucial part of the growing film is its "bulk part". This part influences the properties of the film which are dependent mainly on the elemental and phase composition, microstructure and residual macrostress. As was already stated, the properties are controlled by a whole set of deposition conditions.

The third part of the growing film is its surface. It can be covered with contaminating particles – e.g. a thin oxide layer and the elemental composition can

be different than that of the bulk part of the film. The surface layer is very important when the enhanced tribological properties are desired.

The thin film growth exhibits the following features [25]:

- The first stage of the growth is a random nucleation process (island, layer-by-layer, or its combination (Stranski-Krastanov) – see Figure 2-4).
- The nucleation and growth stages are dependent upon various deposition conditions (substrate temperature, growth rate, substrate surface chemistry).
- The nucleation can be modified by external processes, such as ion or electron bombardment.
- The crystal phase and crystal orientation of the thin films are governed by the deposition conditions.
- Film microstructure, as well as defect structure, and film stress depend on the deposition conditions of the nucleation stage.

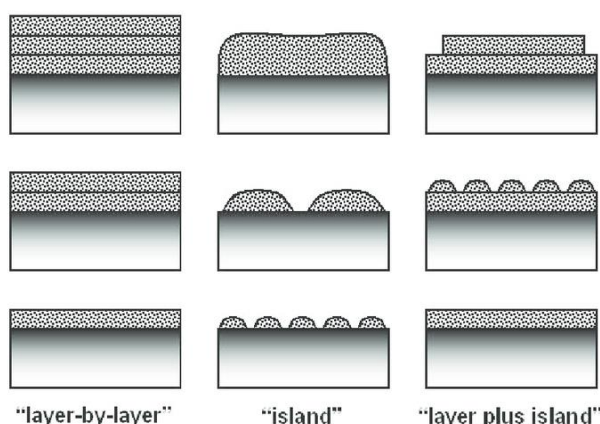

Figure 2-4: Layer grown on a substrate with the (a) layer-by-layer growth mode, (b) island growth mode and (c) Stranski-Krastanov growth mode [26].

2.2.1 Structural zone diagrams

To understand the influence of different factors on the microstructure of the film, structural zone diagrams have been proposed. They show the resulting microstructure as a function of various deposition parameters. A very significant zone diagram presented by Thornton [27] can be seen in Figure 2-5, it is divided into four zones according to sputtering-gas pressure and the substrate temperature. This parameter expressed as a T/T_m ratio is called homologous temperature; T is the substrate temperature and T_m is the melting point of the coating material, both on an absolute temperature scale.

The importance of the homologous temperature was first recognized by Movchan and Demchishin [28] and by Thornton [29], [30]. In these pioneering works, they demonstrated a universal dependence of the coating microstructure on the homologous temperature for metals and alloys with diverse physical and chemical properties as coating materials. A correspondingly universal dependence of mechanical properties on the homologous temperature has been also studied [31]–[33] and is also an important part of the investigation in the present thesis as will be shown in detail in Chapter 5.

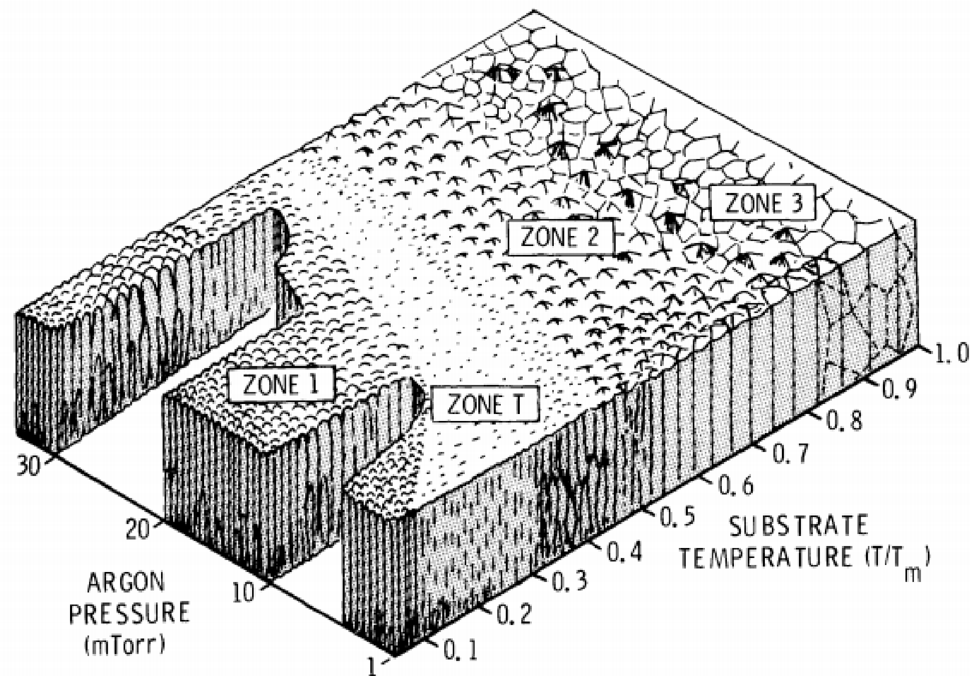

Figure 2-5:Thornton structure zone model [27].

The four zones of the diagram are the following:

- Zone I ($T/T_m < 0.2 - 0.3$) corresponds to the case where mobility of the atoms impacting the substrate surface is very low, atomic shadowing dominates the growth, and the structure consists of isolated fibrous columns.
- Zone II ($0.3 < T/T_m < 0.5$) is characterized by the densification of the microstructure and by the growth of the grains. Surface diffusion is appreciable and the microstructure consists of columnar grains with impervious boundaries. The grain size is typically not higher than the film thickness.
- Zone III ($T/T_m > 0.5$) is the zone where surface diffusion is even more rapid, volume diffusion starts to be the dominant process, grain boundaries

and dislocations are mobile so that recrystallization and grain growth becomes important. The microstructure consists of well-defined crystals which can be bigger than the film thickness and thus the structure is not columnar anymore but exhibits crystalline behaviour.

- Zone T ($T/T_m \approx 0.3$) is the transition region between zone I and zone II. It is characterized by a densified crystalline structure with small grains achieved by the bombardment of the surface by high-energy neutral particles at low pressures.

Although this simple model is still used to predict the microstructure of the films, there was a need for extended zone diagrams. Anders [34] suggested a structural zone diagram applicable for energetic deposition by adding the influence of the energy of impacting particles, which is represented by the pressure in the Thornton diagram. This structure zone diagram is shown in Figure 2-6.

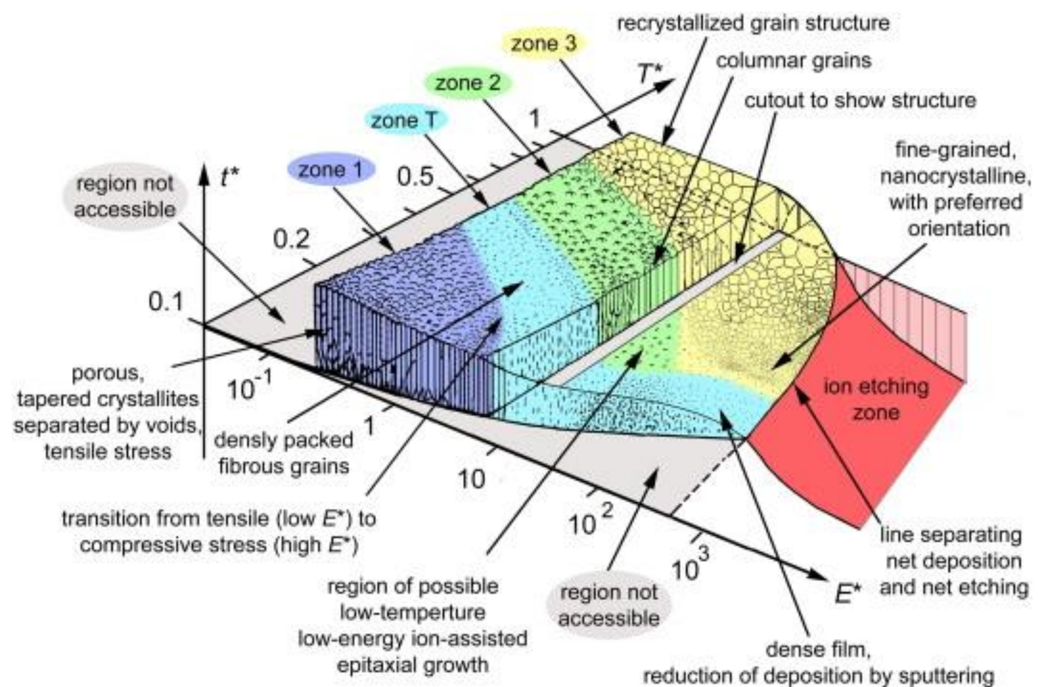

Figure 2-6: Structure zone model applicable to energetic deposition [34].

The temperature is presented by the generalized parameter combining substrate temperature with a temperature shift caused by the potential energy of particles arriving on the substrate surface $T^* = T_h + T_{pot}$, where T_h is the homologous temperature (substrate temperature to melting temperature of the coating material ratio) and T_{pot}

is the characteristic temperature of a heated region affected the rearrangement of N_{moved} atoms: $T_{pot} = E_{pot}/(kN_{moved})$, where k is the Boltzmann constant. The kinetic energy of arriving positive ions is comprised of an initial component from the plasma, E_0, plus a change due to acceleration in the sheath, $E_{kin} = E_0 + QeV_{sheath}$, where Q is the ion charge state number, e is the elementary charge, and V_{sheath} is the voltage drop between the plasma and the substrate surface.

Also, the z-axis was added representing the film thickness; therefore it can be seen that intensive bombardment results in thickness reduction and it shows the ion etching area (“negative thickness”) as well.

2.2.2 Phase diagrams

As was shown in the previous section and will be demonstrated in Chapter 5 on the particular experiments, the microstructure crucially influences the properties of the films. In turn, the microstructure is related to the constitution, which specifies the number of phases present, their proportion, and their elemental composition. A phase diagram is a way to determine the constitution.

In a solid, microstructure typically consists of grains of phases that are adjacent to each other. While the grains are always single-phase, the microstructure can be either a single-phase, when the grains consist of only one-phase, or a polyphase, when the grains consist of many phases.

A phase diagram is a type of chart used to specify conditions at which thermodynamically distinct phases (solid, liquid or gaseous) occur and coexist at equilibrium. The independent state variables that control the phases present in a given phase diagram are the number of elements, the chemical composition, the temperature, the external pressure, etc. Simple phase diagrams generally involve only two state variables, specifically temperature and elemental composition in the present study.

The number of elements in the system classifies and gives a name to the system. All the phase diagrams shown and mentioned in Chapter 5 are binary phase diagrams consisting of two elements (e.g. Zr-Si, Mg-Si).

A phase diagram is a graphical expression of each single-phase field. Three states of equilibrium are distinguished: stable, metastable and unstable. Stable equilibrium exists when the object is in its lowest energy conditions, metastable equilibrium exists when additional energy (ΔG) has to be introduced to reach the stability, and unstable

equilibrium exists when no additional energy is needed to reach metastability or stability as can be seen in Figure 2-7. Equilibrium phase diagrams show only stable phases, however also metastable phases can be present during sputtering. The Gibbs free energy values of all possible phases that can exist in the given system for all possible combinations of the variables are determined by the state variables selected to control this system. The stability and the extent of solid solubility of phases, the temperature dependence of stability, and the choice of structures that are observed in phase diagrams result from competition among possible structures that could be stable in a given system. The values of the Gibbs free energy of each competing phase and the variation of this energy with temperature (and/ or other extensive parameters) influences this competition. Free energy can be written as follows:

$$G = H - TS,$$

where H is the enthalpy, T is the absolute temperature, and S is the entropy.

The major contribution to the entropy is from the statistical mixing of atoms but there can be additional contributions from vibrational effects, distribution of magnetic moments, clustering of atoms and various long-range configurational effects [35]. The main contributions to the enthalpy result from atomic mixing and these are related to the interaction energies between neighbouring and more distant atoms in a given structure and are based upon electronic, elastic, magnetic and vibrational effects.

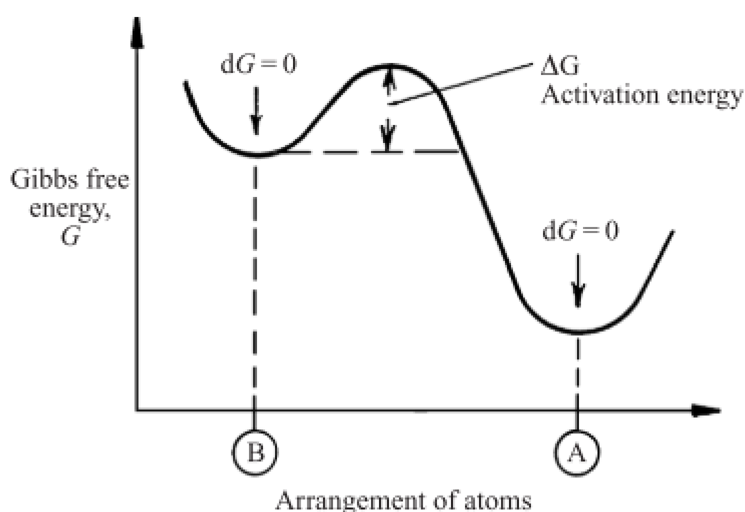

Figure 2-7: Free energy as a function of the arrangements of atoms in phases. A: stable configuration, B: metastable configuration [35].

In a binary system, the free energy G of a given phase typically has a parabolic dependence on the elemental composition as can be seen in Figure 2-8a. In the case that the two structures of the two elements are different, two free energy curves may have to be considered as illustrated in Figure 2-8b. Such curves will become displaced as temperature changes, and at each temperature, the lowest free energy configuration across the diagram will determine which phase is stable at each composition.

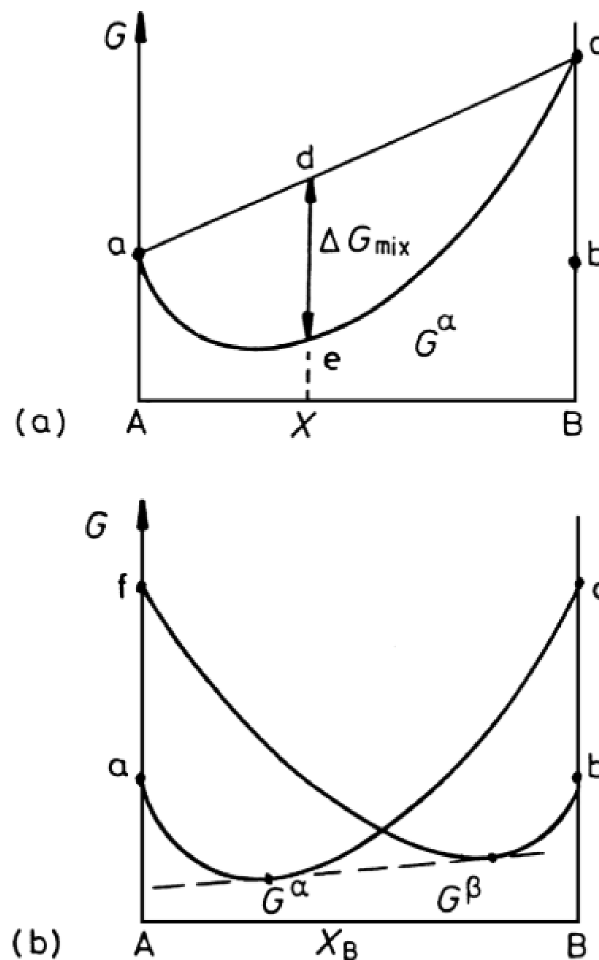

Figure 2-8: (a) Molar free energy curve for the α phase; b) molar free energy curves for α and β phases [36].

A result of such comparison of Gibbs free energy G is a phase diagram in a form of pairs of two single-phase fields with a two-phase field within. The boundary between the liquid field and the two-phase field is called the liquidus; that between the two-phase field and the solid field is called the solidus. A liquidus represents the temperatures at which alloys of the various compositions of the system begin to freeze on cooling, or finish melting on heating; a solidus represents the temperatures at which the various

alloys finish freezing on cooling or begin melting on heating. The phases in equilibrium across the two-phase field (the liquid and the solid solutions) are called conjugate phases [35].

The simplest case of the multicomponent system is that which is completely miscible in both the liquid and solid states. A schematic system together with its relation to the Gibbs free energy is shown in Figure 2-9. An analogous Figure 2-10 shows a eutectic form of phase diagram: two free energy curves are involved in the solid phases. Both binary phase diagrams discussed later in the present thesis are such types of phase diagrams (see Mg-Si phase diagram in Figure 5-8 on page 59 and Zr-Si phase diagram in Figure 5-20 on page 78). The specific examples of the phase diagrams will be given in the following Subsection 2.2.2.1.

According to the phase rule, a two-component system can consist of not more than four phases in contact. The number of degrees of freedom of such a system is two if there are two phases, one for three phases, and none for four phases. The states in which two phases are in equilibrium are then represented by points forming a surface in the 3D coordinate system; the states with three phases (triple points) by points forming a line and states with four phases by isolated points [37].

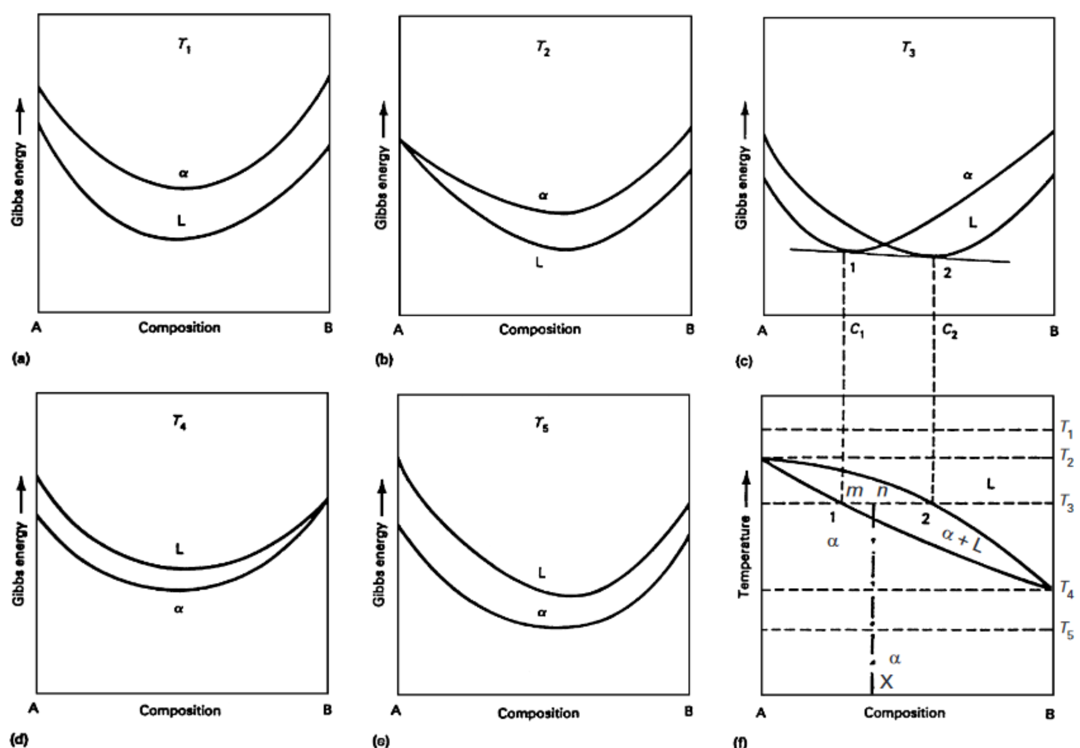

Figure 2-9: Derivation of a phase diagram with complete liquid and solid miscibility from free energy curves [38].

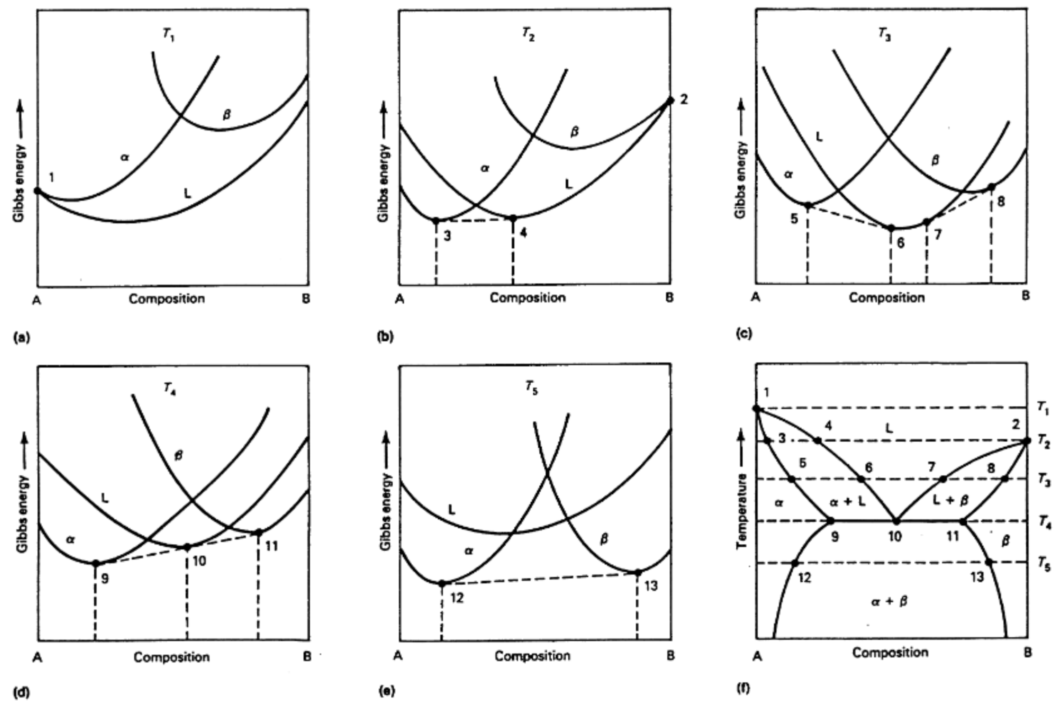

Figure 2-10: Derivation of a eutectic phase diagram (partially miscible) involving free energies of α, β and liquid phases [39].

In 2D diagrams, the lines of intersection of the equilibrium surface with the planes of constant temperature or pressure can be drawn and these lines are called equilibrium curves. The point on an equilibrium curve at which the concentration becomes equal in the two phases can be called either a critical point when all other properties of two phases also become equal (i.e. the phases become identical) or a point of the equal equilibrium concentration [37]. Both critical points and points of equal concentration lie on a curve on the equilibrium surface.

Near a critical point, the equilibrium curve has the form that is shown in Figure 2-11a or a similar form with a minimum at the critical point K. Points lying within this curve in the hatched region represent states in which there is the separation into two phases, the points of intersection of the curve with the appropriate horizontal line determine the concentration in these phases. At point K, the two phases coalesce.

Near a point of equal concentration, the equilibrium curves must have the form shown in Figure 2-11b, or a similar form with a minimum at the point K. The two curves meet at the maximum (or minimum). Analogically, the region between the two phases is where the separation into phases occurs. The concentrations of the two phases in equilibrium become equal at point K, but the different phases continue to exist because

any path between the points which coincide at point K must pass through the region of the separation into two phases.

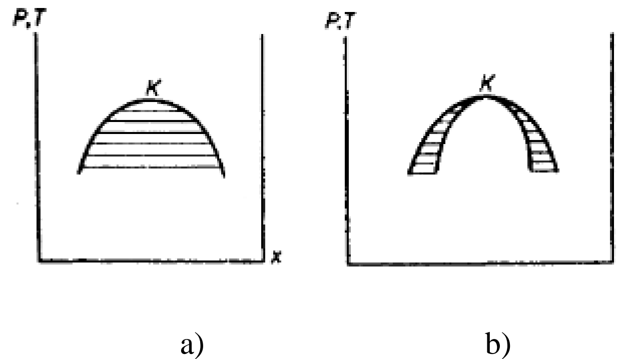

a) b)

Figure 2-11: a) Critical point; b) Point of equal concentration [37].

2.2.2.1 Examples of phase diagrams

At the end of this section, simple examples of the phase diagrams will be given. These curves may have many forms but in most cases, they belong to one of the types that will be briefly described or are a combination of more than one of them. As was written above, the hatched regions are the regions of separation into phases, the remaining regions are those of homogeneous states. The point of intersection of horizontal lines with the curves separating the phases determine the composition of the phases into which the separation occurs.

The simplest case of the phase diagrams has the cigar shape – see Figure 2-12a. There are two phases, each can have any concentration, i.e. the two elements mix in any proportion in both phases. A very similar type of phase diagram is that with a point of equal concentration – see Figure 2-12b.

Another case is the phase diagram with limited miscibility. The two elements mix in any proportions in the liquid state but in the solid state, they do not mix in any proportions. It involves a triple point. Depending on the temperature where the triple point lies, the phase diagram looks like Figure 2-12c or Figure 2-12d: Figure 2-12c when the temperature where the triple point lies is below the pure-element phase equilibrium temperature, Figure 2-12d when it lies between the temperatures of the pure-element phases (point A and C). The region above the curve ABC (Figure 2-12c) or ADC (Figure 2-12d) is the region of liquid states; the hatched region is the region of separation into either a liquid phase and one of the solid states (above DE in Figure 2-12c and BE in Figure 2-12d) or two solid states (below this level); the remaining region is the region

of homogeneous solid phases (solid solutions). Point B in Figure 2-12c is called a eutectic point, which means that a liquid mixture whose concentration corresponds to this point freezes completely without a change of concentration (at other concentrations a solid mixture freezes out with a different concentration than that of the liquid).

A special case is when the two elements do not mix in the solid state at all forming only a chemical compound of definite composition – see Figure 2-12e. The straight line DE gives the composition of the chemical compound. At two triple points (B and G), there is an equilibrium between the liquid phase, the solid chemical compound, and the solid phase of one of the pure elements. D is a point of equal concentration.

If a chemical compound decomposes at a certain temperature before it melts, see Figure 2-12f, then the straight line defining the composition of this compound cannot terminate at a point of equal concentration since it does not reach the melting point, and therefore it terminates at a triple point (A).

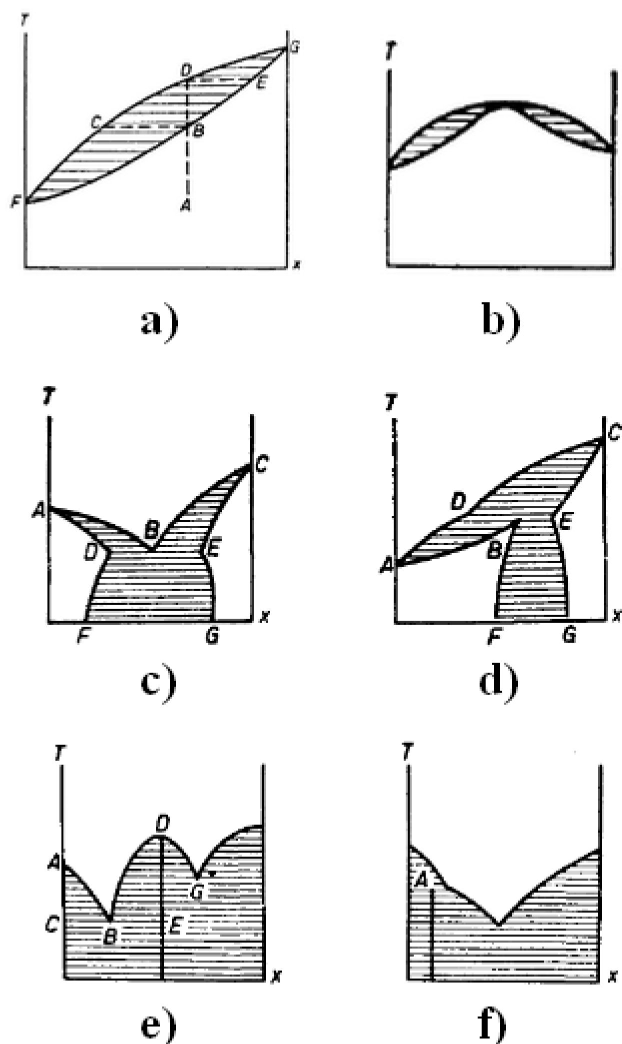

Figure 2-12: Examples of phase diagrams [37].

2.3 Thin films with enhanced hardness and resistance to cracking

2.3.1 Enhanced hardness

Hard thin films have a great potential to be used as protective coatings and magnetron sputtering is a suitable process to be used for their formation both in research and in industrial production. Therefore it is not surprising that magnetron sputtering of hard thin films has been the subject of intensive research over the past 40 years [40]–[55].

The films are usually divided into two groups: hard thin films having a Vickers hardness below 40 GPa and superhard thin films having a hardness higher than 40 GPa. Compared to a large number of hard materials, there are only a few superhard materials, e.g. c-BN, a-CN_x, amorphous diamond-like carbon (DLC), and polycrystalline diamond [49]. These superhard materials lack thermodynamical stability which strongly limits their utilization in some applications.

The understanding of the physics behind the formation and the development of hard thin films is crucial for success in this field. The high hardness of the film can be achieved by correct control of its elemental and phase composition, nano-structure, macrostress generated during the growth, and/ or strong covalent bonds between atoms [56]. Regarding structure, the films can be divided into three groups: crystalline films, nanocomposite films, and amorphous films. All these three kinds of films can exhibit enhanced hardness since properties of the films are further influenced by the size of the grains, the separation distance between grains, the elemental composition of the grains and their crystallographic orientation, the chemical and electronic bonding between the atoms inside grains, and the atoms in neighbouring phases. Even though amorphous films are solids without a long-range order of atoms, they can contain crystalline regions with a short-range order of atoms caused by the chemical bonding between atoms. In the case of strong covalent bonds between the atoms, a high hardness of about 20 GPa can be achieved – which is comparable with that of nanocomposite thin films [57]. There are two groups of nanocomposite films that can be hard: the hard phase/ hard phase nanocomposites such as nc-Me_1N/a-XN and hard phase/ soft phase nanocomposites such as nc-Me_1N/Me_2; here Me_1 = Ti, Ur, W, Ta, Cr, Mo, Al, etc. are elements forming hard nitrides, X = Si, B, C, etc., and Me_2 = Cu, Ni, Ag, Au, Y, etc. are soft metals [56].

2.3.2 Enhanced resistance to cracking

The toughness of the material is defined as its resistance to cracking under an external loading force, so it is the ability of the material to absorb the deformation energy without its cracking. When the deformation of material (the strain ε) is increased, a critical value $\varepsilon = \varepsilon_{cr}$ at which the fracture of the material occur is reached, however. Therefore the resistance of the material to its fracture is called the fracture toughness and is defined by the critical strain ε_{cr} at its failure. The value of ε_{cr} has to be increased in order to enhance the toughness of the material.

The tensile strain is given by Hooke's law

$$\sigma = E \cdot \varepsilon,$$

where σ is the tensile stress (proportional to the hardness), E is the Young's modulus and ε is the strain (deformation). Young's modulus E is furthermore used for calculation of effective Young's modulus E^*:

$$E^* = \frac{E}{1 - \nu^2},$$

see also Chapter 4.3.2.

Figure 2-13 illustrates schematically the stress σ vs. the strain ε dependence for superhard, hard and tough, resilient, and ductile films. It shows that superhard materials are very brittle while the hard thin films exhibit high elastic and low plastic deformation. The fully resilient hard films exhibit lower hardness and no plastic deformation, thus 100% elastic recovery ($W_e = 100\%$). The ductile films are soft and exhibit low elastic deformation and high plastic deformation [56].

Based on Hooke's law, which says that the material with given hardness exhibits the highest elastic deformation ε at the lowest Young's modulus, and detailed continuous research on this subject, four necessary conditions to be fulfilled when preparing the hard thin films with enhanced resistance to cracking were stated as follows [45], [56], [58]:

1. The material of the film must have a low effective Young's modulus E^* ensuring a high ratio $H/E^* \geq 0.1$.
2. The material of the film must exhibit a high elastic recovery $W_e \geq 60\%$.
3. The microstructure of the film must be non-columnar, dense, and voids-free.
4. The film must exhibit a compressive macrostress ($\sigma < 0$).

These findings are of general validity. The films satisfying these conditions can be prepared by the addition of selected material into the base material of the film

or by the delivery of a sufficient energy $\mathcal{E}$ into the film during its growth – see the following Section 2.3.3.

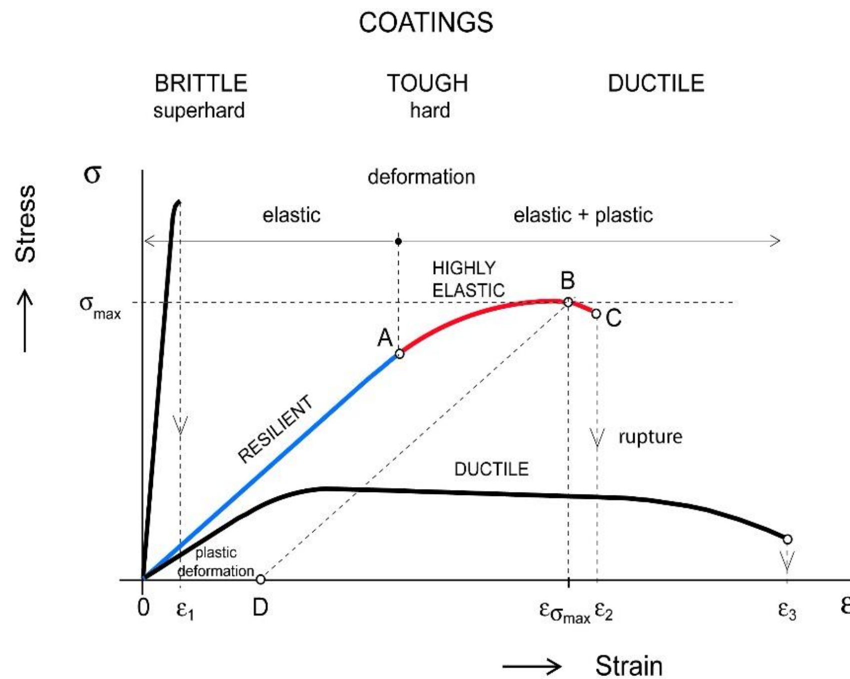

Figure 2-13: Schematic illustration of the stress σ vs. the strain ε dependence of superhrad (brittle), hard (tough), hard (resilient), and ductile films. The resilient films exhibit no plastic deformation (line 0A) [45].

2.3.3 The energy delivered to the growing film

As indicated in the previous sections, the energy $\mathcal{E}$ delivered into the film during its growth has a crucial effect on its structure, microstructure, elemental and phase composition, and physical properties [59]–[63]. The energy $\mathcal{E}$ can be delivered by

- the substrate heating $\mathcal{E}_{sh}$,
- the conversion of the kinetic energy of particles $\mathcal{E}_{p}$, i. e. by the energy of bombarding ions $\mathcal{E}_{bi}$ and/ or fast neutrals $\mathcal{E}_{fn}$ impacting the surface of the growing film,
- the heat evolved during the formation of the compound $\mathcal{E}_{ch}$ (the energy released in exothermic chemical reactions),
- the heating from the sputtered magnetron target $\mathcal{E}_{mt}$,
- the radiation from the plasma $\mathcal{E}_{rad}$.

The total energy $\mathcal{E}_T$ delivered to the growing film can be expressed by the following formula [42]:

$$\mathcal{E}_T = \mathcal{E}_{sh}(T_S, t_D) + \mathcal{E}_p(U_S, i_S, a_D, p_T, t_D) + \mathcal{E}_{ch}(T_S, t_D) + \mathcal{E}_{mt}(W_d, t_D, d_{s\text{-}t}) + \mathcal{E}_{rad}(t_D),$$

where T_S is the substrate temperature, t_D is the time of the film deposition, U_S is the substrate bias, i_S is the substrate current density, a_D is the deposition rate, $p_T = p_{Ar} + p_{RG}$ is the total pressure of the sputtering gas mixture, p_{Ar} and p_{RG} are the partial pressures of argon and reactive gas, respectively; $W_d = U_d \cdot I_d/S$ is the magnetron target power density, U_d and I_d are the magnetron current and voltage, respectively, S is the whole area of the magnetron target and $d_{s\text{-}t}$ is the substrate-to-target distance.

The energy delivered to the growing film by incident particles $\mathcal{E}_p$ consists of two terms:

$$\mathcal{E}_p = \mathcal{E}_{bi} + \mathcal{E}_{fn}.$$

The energy of fast neutrals $\mathcal{E}_{fn}$ can play an important role in low-pressure sputtering. It increases with decreasing pressure during deposition p_T due to prolongation of the mean free path λ due to the reduction of collisions between atoms. According to Dalton's law for the mean free path:

$$\lambda = 0.4\ [\mathrm{cm \cdot Pa}]/\ p_T.$$

In the conventional magnetron sputtering process in the higher pressures, the number of collisions increases and therefore $\mathcal{E}_{fn} \rightarrow 0$ and the energy of ion bombardment $\mathcal{E}_{bi}$ is dominant.

Following this, in collisional discharge, the energy delivered to the growing film by incident particles $\mathcal{E}_p$ can be expressed in the form [4], [64]:

$$\mathcal{E}_p = \mathcal{E}_{bi} = \mathcal{E}_i(\nu_i/\nu_{ca}),$$

where $\mathcal{E}_i$ is the energy of one ion and ν_i and ν_{ca} is the flux of ions and condensing atoms, respectively.

In a collisional plasma discharge, the energy of ion bombardment $\mathcal{E}_{bi}$ delivered per unit volume of the deposited film can be expressed in the following form [4], [64]:

$$\mathcal{E}_{bi} \approx \frac{(U_p - U_S) \cdot i_S}{a_D} \cdot N_{i,max}, \qquad (1\text{-}1)$$

where U_p is the plasma potential, U_S is the substrate bias, i_S is the substrate current density, a_D is the deposition rate and $N_{i,max}$ is the probability of an ion arriving at the substrate with the maximum energy. For a collisional discharge, $N_{i,max}$ can

be calculated as $N_{i,max} = \exp(-L/\lambda)$, where L is the sheath thickness determined by the Child-Langmuir equation for a collision-less sheath [65].

For typical DC magnetron sputtering discharges ($U_d \approx 500$ V, $I_d \approx 0.5$ A, $p_T \approx 1$ Pa), $|U_S| >> |U_p|$ and $N_{i,max} \sim 1$ and therefore the equation (1-1) can be simplified into

$$\mathcal{E}_{bi} \approx \frac{U_S \cdot i_S}{a_D}. \quad (1\text{-}2)$$

Equation (1-2) can be useful despite its simplicity.

2.3.4 Hard and flexible alloy films

Many projects have dealt with magnetron sputtering of (Me_1, Me_2) alloy films containing two Me_1 and Me_2 metallic elements in recent times [66]–[75]. However, these (Me_1, Me_2) alloy films are soft and exhibit a low hardness H < 10 GPa, a high effective Young's modulus E^*, and a low resistance to cracking. One of the main reasons why the (Me_1, Me_2) alloy films easily crack is the low ratio $H/E^* \leq 0.1$. The low hardness of (Me_1, Me_2) alloy films and low resistance to cracking strongly limit their use in many practical applications. Therefore, it is an important task to find an optimal elemental composition of alloy films and correct deposition conditions which will increase their hardness and enhance resistance to cracking.

One of the possible ways how to increase the hardness of the alloy films is to exchange one of the metallic elements for a metalloid. A metalloid is a chemical element with properties between those of typical metals and non-metals. The metalloid elements are in the middle of the periodic table at the point where the metals and non-metals meet, see Figure 2-14. Typical metalloids have a metallic appearance but they are brittle and only fair conductors of electricity. Chemically, they behave mostly as non-metals. Even though metalloid elements are brittle they can form flexible hard (TM, Met) alloy materials in a combination with transition metal (TM) elements.

Metalloid elements were already successfully used in many films, for example, MeC carbides, TMB_2 diborides, MeCN carbonitrides, ternary (Me, Met)N and quaternary (Me_1, Me_2, Met)N nitrides, (Me, Met)O oxides, SiBCN boron carbon nitrides, etc. Metalloids can improve various film properties, e.g. the hardness of the protective nc-Me/a-Si_3N_4 nanocomposite films with a low Si content (≤ 10 at.%) [76], the thermal stability and oxidation resistance of nc-Me/a-Si_3N_4 nanocomposite films with a high Si content (≥ 15 at.%) at temperatures above 1000 °C [77]–[84] and amorphous a-SiBCN

films with strong covalent bonds [57], [85], [86] or the diffusion barrier capability [87]. In the case of a high Si content (≥ 20 at.% Si) when nc-MeN crystallites were embedded in a-Si_3N_4 matrix the $TMeN_x$ nitrides were X-ray amorphous (here TMe = Ti, W, Zr, Cr, etc.). This fact strongly increased their hardness and also improved their other properties such as thermal stability, oxidation and corrosion resistance, wear, and resistance to cracking [77]–[79], [83], [88]–[95].

	13	14	15	16	17
2	B Boron	C Carbon	N Nitrogen	O Oxygen	F Fluorine
3	Al Aluminium	Si Silicon	P Phosphorus	S Sulfur	Cl Chlorine
4	Ga Galium	Ge Germanium	As Arsenic	Se Selenium	Br Bromine
5	In Indium	Sn Tin	Sb Antimony	Te Tellurium	I Iodine
6	Tl Thalium	Pb Lead	Bi Bismuth	Po Polonium	At Astatine

Figure 2-14: Classification of metalloid elements: (1) commonly recognized (93%): B, Si, Ge, As, Sb, Te (blue), (2) irregularly recognized (44%): Po, At (red), (3) less commonly recognized (24%): Se (yellow) and (4) rarely recognized (7%): C, Al (green) [96].

Also, some research on (Me, Si) films – which was one of the main goals of the present work – has been done [97]–[115]. Some of these reported (Me, Si) films exhibit a low ratio H/E^* and easily crack. However, most of the papers are devoted to the optical and electronic properties of the films and the investigation of their mechanical properties is lacking.

A detailed characterization of mechanical properties related to the deposition conditions of the hard alloy films with enhanced resistance to cracking is reported in Chapter 5 of the thesis.

3 AIMS OF THE THESIS

The main aim of the Ph.D. thesis is the detailed investigation of the physical and mechanical properties of alloy films prepared by magnetron sputtering to find the deposition conditions enabling the formation of hard protective coatings with enhanced resistance to cracking. All the sputtered films are prepared using a pulsed dual magnetron system. The detailed characterization of the deposition conditions, the properties of the films and their relationship is given.

The common goal of the presented projects is to determine the deposition conditions at which the necessary requirements for the formation of hard, super-elastic protective alloy films are met ($H/E^* > 0.1$, $W_e \geq 60\%$, low compressive macrostress ($\sigma \leq |2\ \text{GPa}|$) and dense, voids-free microstructure corresponding to the zone T at Thornton‘s structural zone; here H is the hardness, E^* is the effective Young‘s modulus, σ is residual macrostress generated in the film during its growth).

The individual tasks are as follows:

1. Magnetron sputtering of Zr-Si alloy films containing hard element Zr with a high melting point ($T_{m(Zr)} = 2125$ K).
2. Magnetron sputtering of Mg-Si alloy films containing soft element Mg with a low melting point ($T_{m(Mg)} = 922$ K) and hardness enhancement of Mg-Si alloy films from ca. 10 GPa up to 25 GPa by addition of nitrogen into the films and formation of Mg-Si-N nitride alloy films.
3. Magnetron sputtering of Si-N nitride films and further enhancement of the hardness of the Mg-Si-N films.
4. Characterization of the role of the homologous temperature (T_S/T_m, here T_S is the substrate temperature and T_m is the melting point) controlling the mechanical properties of alloy films.

4 EXPERIMENTAL DETAILS

This chapter is divided into four parts – Section 4.1 describes the deposition system, Section 4.2 briefly summarizes the substrate preparation prior to the deposition, Section 4.3 introduces the analytical methods used for characterization of the films and Section 4.4 gives the lists of deposition conditions of the Zr-Si, Mg-Si, Mg-Si-N and Si-N films.

4.1 Deposition system

The main components of the deposition system are: the deposition chamber, the pumping system, the power supplies, the magnetrons and the targets, the appliances for controlling and measurement of the process parameters (e.g. substrate temperature, bias voltage, total and partial pressure(s), gas flow, etc.). Their description follows in the subsequent sections.

4.1.1 Deposition chamber

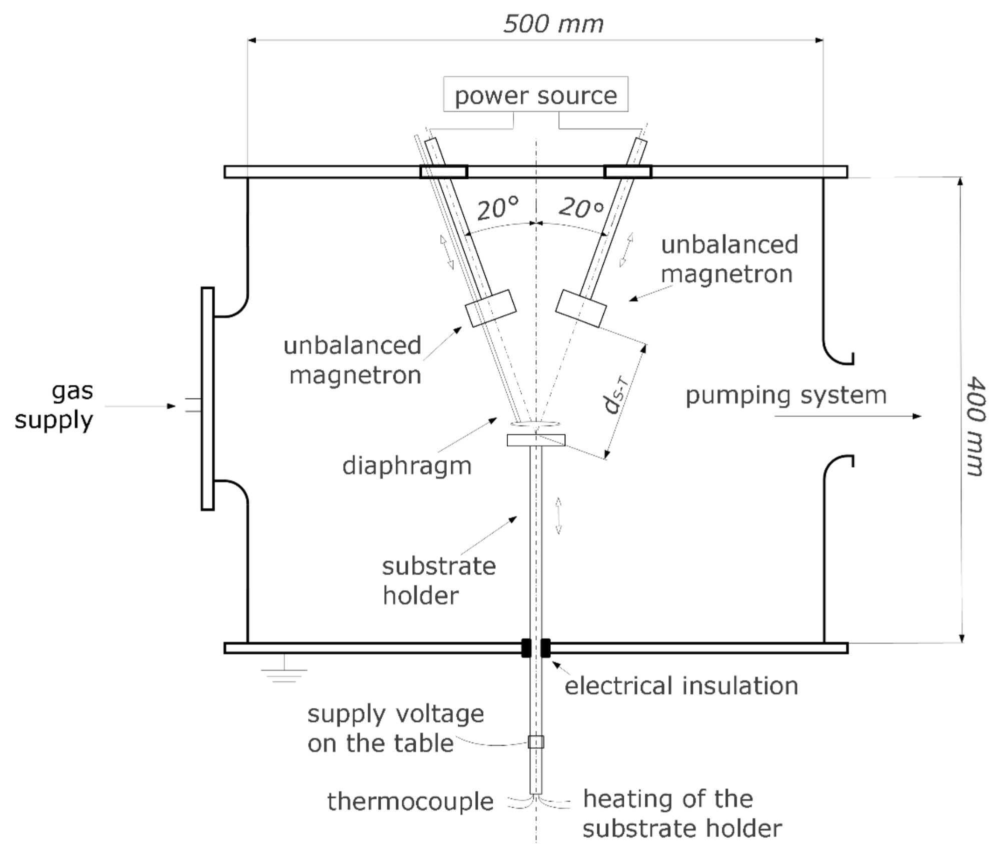

Figure 4-1:Technical drawing of the deposition chamber.

The deposition chamber is schematically illustrated in Figure 4-1. It is made of stainless steel with duraluminium flanges and has a cylindrical shape with a diameter of 500 mm and a height of 400 mm. Two magnetrons in a closed magnetic field configuration are mounted in the top flanges and are tilted at the angle of 20° to the vertical axis and equipped with inner and outer permanent magnets. The substrate holder is installed in the bottom flange of the chamber and can be ohmically heated up to 500 °C (the substrate temperature is monitored by a K-type NiCr-NiAl thermocouple), shifted in the vertical direction, and biased using an external power supply.

4.1.2 Pumping system

Evacuating the chamber to a sufficiently low base pressure is a crucial task for reducing contamination in the films. For this purpose, a two-stage pumping system is employed. A rotary vane pump with a pumping speed of 6.9 l/s can evacuate the system from atmospheric pressure down to ≈ 1 Pa. It serves as a fore-pump to provide sufficiently low pressure for the operation of the turbomolecular pump, which requires a maximum pressure at the output < 1300 Pa. The pumping speed of the turbomolecular pump is 290 l/s. Depending on the pumping time, substrate holder temperature, and deposited materials, such a two-stage system can reach a base pressure of $p_0 < 1\cdot10^{-3}$ Pa.

Various types of pressure gauges are used for monitoring the pressure before and during the deposition. Three Pirani gauges indicate the pressure in the deposition chamber, between the gate valve and the turbomolecular pump, and between the turbomolecular pump and the rotary pump. The range of the operation of the Pirani gauge lies between atmospheric pressure and $5\cdot10^{-2}$ Pa. Its accuracy is below 0.1 Pa. The Pirani gauge is calibrated to operate in air, O_2, N_2, and CO and therefore it can not be properly used when the mixture of argon and reactive gas is introduced into the system. The Penning gauge measures the pressure in a lower range and it is used to calibrate the capacitance Baratron gauge. When a sufficiently low base pressure is achieved (typically $1\cdot10^{-3}$ Pa in the experiments described in this thesis), the Baratron gauge is set to zero value and after that, various gases may be introduced into the system. The Baratron gauge is a gas-independent gauge, so it is suitable for monitoring the total pressure during deposition.

The flow of the working gas, which is argon of 99.999% purity, and reactive gases (nitrogen, 99.999%, and oxygen 99.995%) is controlled by mass-flow controllers (MKS Mass-Flo Type 1179A). The maximum flow rates are 139 sccm for Ar, 100 sccm for N_2 and 19.9 sccm for O_2. Bellows-sealed valves are installed between the mass-flow controllers and the deposition chamber for the ease of maintenance and to avoid possible contamination of the gas mixture by gases that are not currently used. The mass-flow controllers are controlled by a multi-gas controller (MKS 647 C) unit. It is possible to control the flow rates of up to four different gases in various modes. In the independent mode, the flow rate is set to the demanded setpoint value. The PID mode is the feedback mode in which the multi-gas controller compares the setpoint value of the total pressure with the actual pressure measured by the Baratron gauge and using a feedback algorithm the flow rate of reactive gas is adjusted to achieve the setpoint value of the total pressure while the flow rate of the working gas is set constant. Such a procedure is repeated continuously and automatically to maintain the desired total pressure during the whole time of the deposition. In this way, the partial pressure of the reactive gas p_{RG} (RG = O_2 or N_2) can be calculated as a simple difference between the total pressure p_T and the partial pressure of argon p_{Ar} measured before introducing the reactive gas. The total pressure may also be regulated by a control gate valve (VAT 64244-PE52) as well as the partial pressures of working and reactive gases. The cross-section of this gate valve can be varied in 1000 discrete steps ranging from fully open to fully closed. It allows changing the pressure value while keeping the flow rate(s) constant.

4.1.3 Power supplies

For the experiments described in this thesis, two different power supplies were used: (i) pulsed DC power supply RMP 10 (Huttinger Elektronik) for powering the dual magnetron and (ii) pulsed DC power supply IAP 1010 (EN Technologies) for biasing the substrates.

4.1.3.1 RMP 10 (Hüttinger Elektronik)

RMP 10 is a floating pulsed DC power supply consisting of two DC power sources and a MOSFET switch-based section responsible for modulating the DC output signal to the desired shape (DC, rectangular or trapezoidal). The maximum power it can provide is 10 kW – either with a maximum current of 12.5 A at 800 V or 25 A at 400 V. The power

supply can operate in three different regimes depending on the output parameter chosen to be constant (current/ voltage/ power). The pulse repetition frequency f_r can range between 4 and 100 kHz and the duty cycle (i. e. the ratio of negative voltage pulse length τ and the pulse period T) can be set to 20 – 80%. The dual magnetron operates either in a single or a dual magnetron regime. In the single magnetron regime, only one magnetron target is sputtered in a DC or pulsed mode. In the dual magnetron regime, the voltage periodically changes and both magnetrons are sputtered – see Section 2.1.1 for more details.

The process parameters used in the thesis are defined as follows. I_d represents the average cathode current in the pulse-on time. U_d represents the average potential difference (i.e. average voltage) between magnetron 1 and magnetron 2 in the pulse-on time. To simplify, these two parameters are referred to as discharge current and discharge voltage throughout the thesis. The average target power in a pulse P_d can be calculated by a simple multiplication of I_d and U_d, therefore

$$P_d = I_d \cdot U_d \,.$$

The target power loading can also be expressed in terms of average target power density in pulse

$$W_t = \frac{P_d}{S},$$

where S = 19.63 cm^2 is the surface area of the target.

4.1.3.2 IAP 1010 (EN Technologies)

For biasing the substrates, the pulsed DC IAP 1010 power supply was used. It can be operated in three various modes – DC, unipolar and bipolar. The frequency can be ranged between 5 and 50 kHz and the duty cycle can be varied between 2 and 90%. The maximum output power is 10 kW – the output voltage can be set between 50 and 1000 V, the output DC current can be set up to 10 A, and the output pulse current can be up to 20 A (duty cycle 50%).

4.2 Substrate preparation

Si(100) substrates of dimensions of 20 x 20 x 0.525 mm^3 were used for evaluation of the mechanical properties, for XRD measurements, and investigation of the electrical properties. Si(100) stripes of dimensions of 30 x 5 x 0.525 mm^3 were used as substrates

for measurements of the residual macrostress. Before deposition, all substrates were immersed in acetone and placed into an ultrasonic bath for 10 minutes.

The pre-deposition etching of substrates was performed in the pulsed discharge (generated between the substrate and the substrate holder) at the voltage U = -1000 V and argon pressure p_{Ar} = 1.5 Pa for 10 minutes.

4.3 Thin-film characterization

This section describes the analytical methods used for the characterization of the thin films discussed in this thesis.

4.3.1 Thickness, deposition rate, macrostress

The film thickness, surface roughness, and residual macrostress were determined using a Dektak 8 stylus profilometer (Veeco Metrology Group). The profilometer uses a diamond-tipped stylus to scan the surface of the film with a declared vertical resolution as low as 1 nm. Before every deposition, a part of the substrate is covered with a small piece of Si(100). After removing this fragment, the height of the step between the coated and uncoated part of the substrate can be easily measured by the profilometer. A scan across the step is performed at 3 different locations and the average value gives the film thickness h.

When the film thickness is known, the deposition rate a_D can be easily calculated:

$$a_D = \frac{h}{t},$$

where t is the deposition time.

Concerning the residual macrostress of the film, first, a scan of the uncoated silicon substrate has to be performed before the deposition. After the deposition, the coated substrate is scanned again and the macrostress σ is evaluated using manufacturer-provided software according to Stoney's formula [116]:

$$\sigma = \frac{E_s}{6\,(1-\nu_s)}\frac{h_s^2}{h_f}\left(\frac{1}{R}-\frac{1}{R_0}\right),$$

where E_s is Young's modulus, ν_s the Poisson's ratio and h_s the thickness of the substrate, h_f is the thickness of the film, and R and R_0 are the curvature radii of the substrate after and before the deposition.

Stoney's formula requires the following conditions [117], [118]:

- the thicknesses of the substrate and the coating are smaller than the lateral dimensions;
- deformations and rotations are infinitesimal;
- the thickness of the coating is smaller than the thickness of the substrate;
- the substrate and the coating are homogenous, isotropic, and linear elastic;
- the radius of curvature is equal in all directions (spherical deformation);
- the stress and the radius of curvature are constant on the whole surface of the plate.

According to a convention, when the radius has a convex shape, then the residual mactrostress is considered to be compressive ($\sigma < 0$ GPa), and when the radius is concave, the macrostress exhibits a positive value and is tensile ($\sigma > 0$ GPa).

4.3.2 Mechanical properties

Hardness H, effective Young's modulus E^*, and elastic recovery W_e were determined from load vs. displacement curves measured using a microhardness tester Fischerscope H100 with a Vickers diamond indenter. During the measurement, the diamond indenter is gradually pressed into the surface of the film with an increasing load. A certain hold-on time (creep) can be applied at the maximum load and then the indenter load is decreased. During the process, a load-displacement curve is being drawn showing the indenter depth-load dependence (see Figure 4-2).

For a proper measurement (to avoid the substrate influence), the depth of the indent should not exceed 10% of the film thickness. Therefore the optimum load has to be set.

From the data obtained from the load-displacement curve, the hardness can be calculated using

$$H = \frac{F_{max}}{A_p},$$

where F_{max} is the maximum applied load and A_p is the projected area of contact between the indenter and the tested sample. The projected area A_p for Vickers indenter is obtained from

$$A_p = 24.5\, h_c,$$

$$h_c = h_{max} - \varepsilon(h_{max} - h_s).$$

Here ε is the correction factor for the indenter geometry (0.75 for the Vickers indenter), h_c is the corrected depth of contact of the indenter with the test piece at F_{max},

h_{max} is the maximum penetration depth at a maximum load F_{max} and h_s is the plastic depth given by the intersection of the tangent to the unloading curve at F_{max} with the indentation depth axis [119].

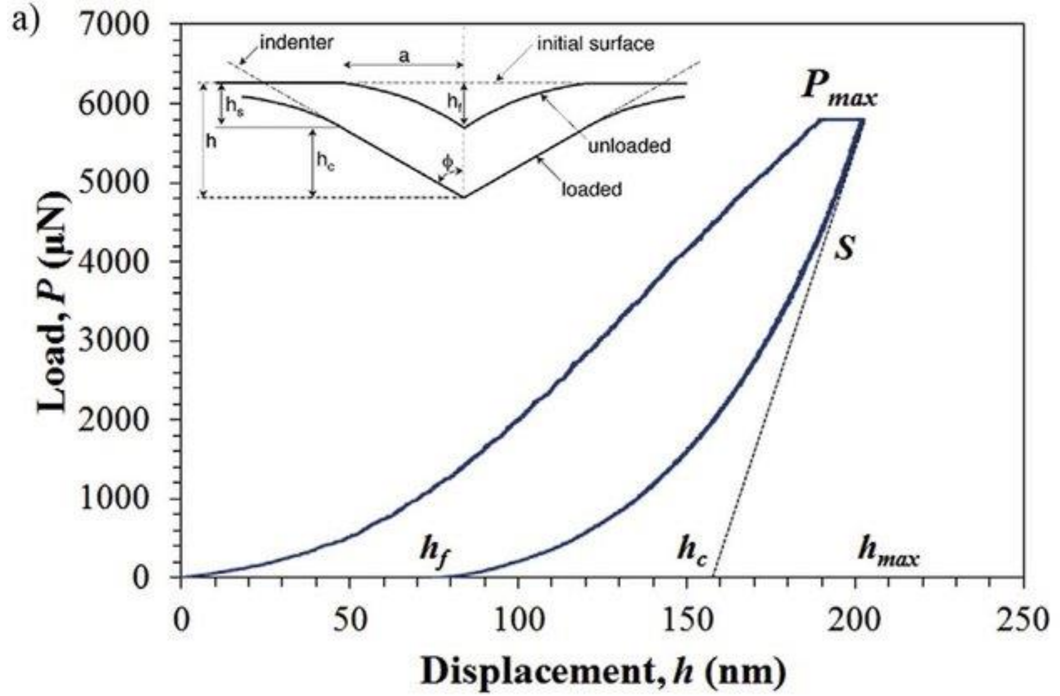

Figure 4-2: Typical load-displacement curve. The inserted schematic of the indentation footprint illustrates the indentation deformation at peak load and the four penetration depths of interest (h, h_s, h_c, and h_f) [120].

The film stiffness can be expressed employing the effective Young's modulus E^*, which is given as

$$E^* = \frac{E}{1 - \nu^2}$$

and is calculated from the following equation

$$E^* = \frac{1}{\frac{1}{E_r} - \frac{1 - \nu_i^2}{E_i}}.$$

Here E is Young's modulus, E_i and ν_i are the indenter Young's modulus and Poisson's ratio, respectively, and the reduced Young's modulus E_r is given by the stiffness S of the upper portion of the unloading curve

$$S = \frac{dP}{dh},$$

where P is the load applied to the indenter and h is its displacement, by the contact area of the impression A_p, and by the geometrical correction factor β (close to 1 for our four-side pyramid indenter) as

$$E_r = \frac{\sqrt{\pi}S}{2\beta\sqrt{A_p}}.$$

These formulas were first introduced in [121].

Another important mechanical characteristic is the elastic recovery W_e. It is the ratio of the elastic deformation work to the total deformation work which provides information about the extent of the elastic deformation of the material. It can be calculated from F = F(h) functions for loading and unloading as follows:

$$W_e = \frac{W_{elast}}{W_{total}} = \frac{W_{elast}}{W_{elast} + W_{plast}},$$

where W_{elast} and W_{plast} are the elastic and plastic components of the total indentation work W_{total}.

H/E^* ratio is another important parameter, which can predetermine some properties of the film, such as wear-resistance [50] and resistance to cracking [14], [45], [56] – see section 2.3.2. The H/E^* is linearly proportional to the elastic recovery W_e: $H/E^* = k \cdot W_e$, where k is a parameter dependent on the indenter load, homogeneity, and structure of the film [122].

4.3.3 Resistance to cracking

The term "resistance to cracking" refers to the resistance of the film against the formation and propagation of cracks under an external load as explained in section 2.3.2. The evaluation of the films used in this study was performed using the indentation test which was shown to be a simple and useful technique for a qualitative comparison of the toughness of thin films [44], [123]. The measurement was carried out using the Fisheroscope H100 microhardness tester with a Vickers diamond indenter. To generate cracks, high indenter loads (ranging between 250 and 1000 mN) were used. The surfaces of the films were subsequently evaluated using an optical microscope so the presence of the cracks could be confirmed or disproved. The standard (idealized) cracks which can be observed are shown in Figure 4-3. In most cases, the radial or lateral

crack occurs in the films. Since it is a qualitative method, only the presence (or absence) of the crack is evaluated together with the load at which it occurred.

The test depends on many parameters such as the film microstructure, the depth of the diamond impress into the film surface that unlike in the measurements mechanical properties of the film does not need to satisfy the 10% rule, and also on the mechanical properties of the substrate.

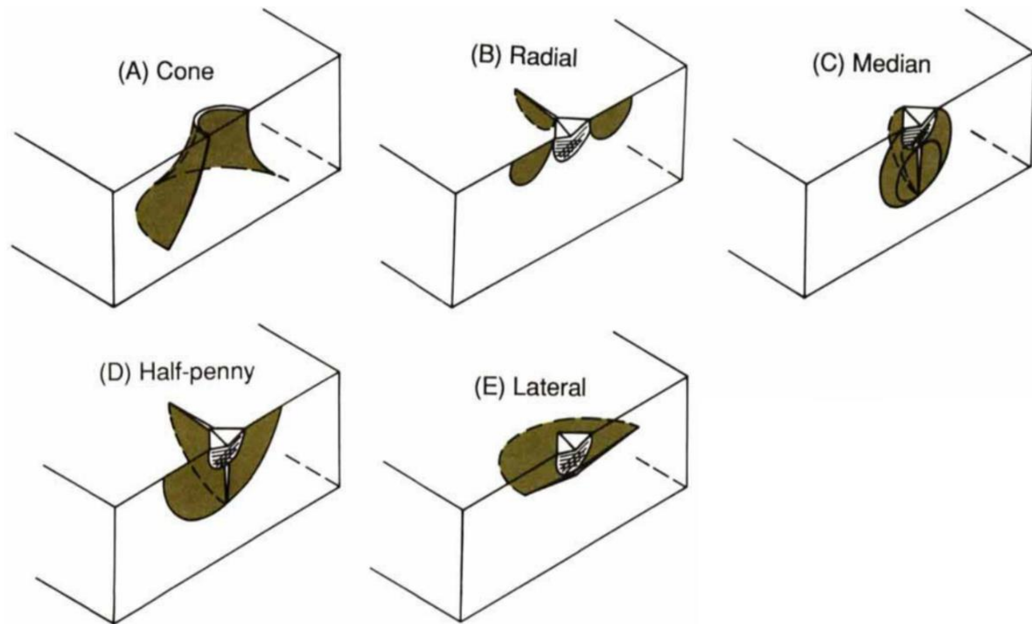

Figure 4-3: Isometric sections of idealized crack morphologies observed at indentation contacts [124].

4.3.4 Electrical resistivity

The electrical resistivity ρ of the films was measured using a standard four-point technique with 1.047 mm spacing between tips. The tungsten tips are perpendicularly attached to the surface of the sample as can be seen in Figure 4-4. Current is applied through the two outer pins 1 and 4 from the external DC current supply 6220 DC Current Source (Keithley). Using voltmeter 6514 System Electrometer (Keithly) it is possible to measure the potential difference between the inner tips 2 and 3.

The electrical resistivity is then calculated using

$$\rho = \frac{\Delta U}{I} \cdot t_f \cdot F \cdot C \cdot K_S \cdot K_T,$$

where ΔU and I are the potential difference between the inner pins and the current between the outer tips, respectively, t_f is the film thickness, F is the thickness correction

($F = 1$ when $t_f < 0.6$), C is the area correction and K_S and K_T are corrections of geometric dimensions of the measuring head and the temperature, respectively. $K_S = 1$ if the tips are placed at least 5 mm far from the edges of the sample and

$$K_T = 1 + 0.01(T_r - 24),$$

where T_r is the room temperature.

For the measurement accuracy, the measurement is carried out at three different spots of the sample and the resulting electrical resistivity is averaged.

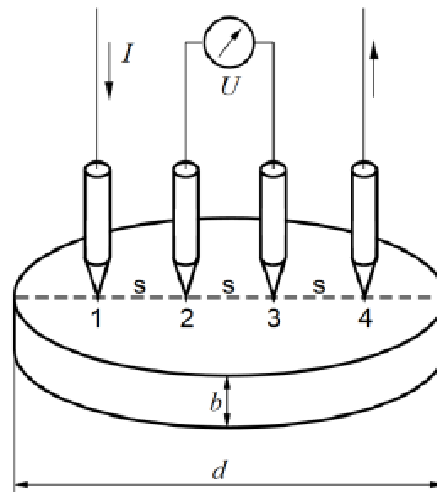

Figure 4-4: Scheme of the four-probe head for the electrical resistivity measurement [125].

4.3.5 Structure and phase composition

The structure of the films was characterized by an X-ray diffraction technique which is based on irradiating a sample of the material with incident X-rays and then measuring the intensities and scattering angles of the X-rays that are scattered by the material. Then the intensity of the scattered X-rays is plotted as a function of the scattering angle. Afterwards, the structure is determined from the analysis of the location and the intensities of scattered intensity peaks, in angle.

The films in this study were measured using a PANalytical X'Pert PRO spectrometer in the Bragg-Brentano configuration with CuKα radiation ($\lambda = 1.54187$ Å) by comparison with powder substrates. The X-ray tube is stationary and the sample moves by an angle θ and the detector (semiconductor detector X´Celerator) moves by the angle 2θ simultaneously. The angle between the sample and the incident beam is the same as the angle between the sample and the diffracted beam, so Bragg's law is fulfilled only

for crystal planes that are oriented parallel to the surface of the sample. Crystal planes that are not parallel with the surface are not detected.

4.3.6 Elemental composition

The elemental composition of sputtered films on Si substrates was analyzed in a scanning electron microscope (SEM, SU-70, Hitachi) operated at a primary electron energy of 5 or 10 keV. The SEM utilizes an accelerated focused electron beam that scans the surface of the sample. Secondary electrons, backscattered electrons, and emission of electromagnetic radiation are the result of the interaction of the electron beam with the sample. Each of these can be analyzed by a specialized detector. For the measurement of the elemental composition, the X-rays are detected by the energy dispersive spectroscopy (UltraDry, Thermo Scientific).

The standard error of the measured values is within 5%.

4.3.7 Surface morphology and cross-sections

Surface morphology of the films after the indentation test was examined by a light optical microscope (Axio Imager.Z2m) using brightfield or circularly polarized light – differential interference contrast.

The fracture cross-sections of the films deposited on Si(100) substrates were investigated by a scanning electron microscope (SEM, SU-70, Hitachi) at an operating voltage of 5 kV.

4.4 Deposition conditions

4.4.1 Zr-Si films

The Zr-Si alloy films, presented in Chapter 5.1, were deposited by a pulsed dual magnetron (PMD) with a closed magnetic field in Ar gas. The dual magnetron was operated with asynchronous pulses and equipped with composed Si/Zr targets (Si round plates of diameter ∅ = 38 mm fixed to the magnetron's cathodes by Zr fixing rings with the same inner diameters ($\varnothing_i$ = 25 mm)). The magnetrons were powered by a pulsed RMP-10 power supply (Hüttinger, Germany) at various repetition frequencies of pulses f_r = 10 kHz and 100 kHz and the duty cycle $\tau/T = 0.5$; here τ is the length of the pulse and $T = 1/f_r$ is the period of pulses.

The films were sputtered onto Si(100) substrates which were held at a temperature T_S = 300 °C and were either floating ($U_S = U_{fl} \approx 3$ V) or DC biased.

The whole list of the deposition parameters is in Table 4-1.

Table 4-1: Deposition parameters of the Zr-Si films.

Parameter	Value
base pressure p_0 [Pa]	$1 \cdot 10^{-3}$
total pressure during deposition $p_T = p_{Ar}$ [Pa]	1.0 and 0.3
substrate temperature T_S [°C]	300
averaged target power density per pulse $W_{tp} = I_{dp} \cdot U_d /S$ [W/cm^2] [1]	20 and 26
repetition frequency f_r [kHz]	10 and 100
substrates-to-targets distance d_{s-t} [mm]	60 and 80
substrate bias voltage U_S [V]	U_{fl} (≈ 3 V) to -200

4.4.2 Mg, Si, Mg-Si, Mg-Si-N and Si-N films

The Mg-Si alloy, Mg-Si-N and Si-N nitride films were also sputtered by a pulsed dual magnetron (PDM) with a closed magnetic field operated with asynchronous pulses. Pure Si, Mg, and composed Mg-Si round plates of a diameter ∅ = 50 mm were used as magnetron targets (see Figure 4-5). The PDM was powered by a pulsed power supply (Huttinger RMP-10) at a repetition frequency $f_r = \tau/T$ = 100 kHz; here $\tau = \tau_1 + \tau_2$, τ_1 and τ_2 is the length of a pulse at the magnetron 1 (M1) and the magnetron 2 (M2), respectively, and T is the period of pulses. The elemental composition of the Mg-Si alloy was controlled by the choice of the targets and the ratio τ_1/τ_2 and the (Mg-)Si-N nitride films were controlled by the amount of N_2 in the Ar + N_2 mixture of sputtering gas. The discharge power density W_t at the magnetron target used in the experiment was calculated from the formula $W_t = (\tau_x/T)(U_{px} \cdot I_{px})/S_t$; here (τ_x/T) is the duty cycle, U_p

[1] Here I_{dp} is the discharge current averaged over the pulse period $T = 1/f_r$, U_d is the discharge voltage, and S is the whole area of the magnetron target.

and I_p are the voltage and the current, respectively, in a pulse and S_t is the target area and x stands for either magnetron 1 (M1) or magnetron 2 (M2).

The films were sputtered on Si(100) substrates located at the substrate-to-target distance d_{s-t} = 120 mm held either at the floating potential $U_S = U_{fl} \approx 3$ V or the pulsed bias with alternating negative and positive pulses $U_S^- = -50$ V/ $U_S^+ = 50$ V with frequency $f_{rs} = 5$ kHz and ratio $\tau^-/\ \tau^+ = 25/\ 75$ using pulsed DC power supply IAP 1010 (EN Technologies).

Table 4-2 gives a list of deposition parameters of the Mg, Si, Mg-Si, Mg-Si-N, and Si-N films discussed in Chapter 5.2 and Table 4-3 lists deposition parameters of Si-N films discussed in Chapter 5.3.1.

The technical drawing of the table with substrates and their position to magnetrons is shown in Figure 4-6.

Figure 4-5: Composed Mg-Si targets with two various diameters (25 mm and 38 mm) and pure Mg target with a diameter of 50 mm.

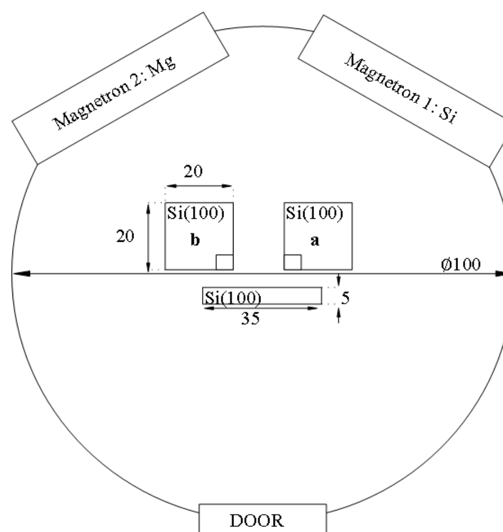

Figure 4-6:Technical drawing of the table with substrates and magnetrons.

Table 4-2: Deposition parameters of the Mg, Si, Mg-Si, Mg-Si-N, and Si-N films.

base pressure p_0 [Pa]	$1 \cdot 10^{-3}$
total pressure during deposition $p_T = p_{Ar} + p_{N2}$ [Pa]	0.3, 0.5, 1.0
substrate temperature T_S [°C]	200
repetition frequency f_r [kHz]	100
substrates-to-targets distance d_{s-t} [mm]	120
substrate bias voltage U_S [V]	U_{fl} (≈ 3 V)

Table 4-3: Deposition parameters of the Si-N films.

base pressure p_0 [Pa]	$1 \cdot 10^{-3}$
total pressure during deposition $p_T = p_{Ar} + p_{N2}$ [Pa]	0.3
substrate temperature T_S [°C]	RT – 500
repetition frequency f_r [kHz]	100
substrates-to-targets distance d_{s-t} [mm]	120
substrate bias voltage U_S [V]	pulsed bias

5 RESULTS AND DISCUSSION

This chapter is devoted to the individual aims of the thesis and discussion of the results. The main goal was to find the conditions under which it is possible to sputter thin alloy films with high hardness and enhanced resistance to cracking.

Two types of alloy films are introduced in detail: Zr-Si and Mg-Si films. Furthermore, nitride Mg-Si-N and Si-N films are presented. Both the deposition conditions and their relation to the properties of the films were investigated and are described thoroughly. The overall insight on all the present experiments is then given in the last part of this chapter where the effect of the homologous temperature T_S/T_m on the mechanical properties of the alloy films is discussed.

I carried out all of the presented depositions using the techniques described in Chapter 4. I measured and interpreted the following film properties: thickness h, residual macrostress σ, mechanical properties (hardness H, effective Young's modulus E^*, elastic recovery W_e), resistance to cracking and elemental composition according to the methods described in Chapter 4.3. The XRD measurements and analysis were carried out by Ing. Radomír Čerstvý, Ph.D., the cross-sectional images were carried out by RNDr. Stanislav Haviar, Ph.D., and the AFM measurements of the topography of the films were carried out by Ing. Jiří Rezek, Ph.D. The obtained data were discussed with prof. Ing. Jindřich Musil, DrSc. and doc. Mgr. Šimon Kos, Ph.D. to find the best comprehension and interpretation.

5.1 Flexible hard Zr-Si alloy films prepared by magnetron sputtering

This chapter deals with the investigation of the mechanical properties of Si-rich Zr-Si alloy films deposited by magnetron sputtering. The main aim of this investigation is to develop flexible hard Zr-Si alloy films with enhanced resistance to cracking. The Zr-Si films were formed by a pulsed dual magnetron discharge. Mechanical properties and elemental composition of sputtered Zr-Si films were tuned by a negative substrate bias U_S, i.e. by the energy $\mathcal{E}_{bi}$ delivered to the growing film by bombarding ions. It was found that using of pulsed dual magnetron discharge makes it possible to deposit flexible hard Zr-Si alloy films with high values of hardness $H \approx 20$ GPa, ratio $H/E^* > 0.1$, elastic recovery $W_e > 60\%$, compressive macrostress ($\sigma < 0$) and dense, voids-free microstructure. These alloy films contain approximately the same amount of Zr and Si in at.% and exhibit strongly enhanced resistance to cracking.

The results presented in this chapter were published in a special issue of Thin Solid Films honouring Professor Joe Greene (*J. Musil, Z. Čiperová, R. Čerstvý, and S. Haviar, Flexible hard (Zr, Si) alloy films prepared by magnetron sputtering, Thin Solid Films, (2019)).*

5.1.1 Results and discussion

The $ZrSi_x$ films were sputtered at high and low argon pressure p = 1 and 0.3 Pa as a function of the negative substrate bias U_S at a target power density $W_{tp} = 20$ W/cm^2 and 26 W/cm^2, respectively. The decrease of pressure was accompanied by the increase of repetition frequency from fr = 10 kHz at p = 1 Pa to fr = 100 kHz at p = 0.3 Pa. The reason for this change was that the deposition system does not allow operating a stable discharge at low pressure with the simultaneous use of low repetition frequency. By increasing the repetition frequency from 10 to 100 kHz, the discharge was stable. The overview of the deposition conditions is listed in Table 4-1 on page 41.

The structure, elemental composition, and physical and mechanical properties of the $ZrSi_x$ films strongly depend on the energy $\mathcal{E}_{bi}$ delivered to the growing film by bombarding ions, see Figure 5-1 and Table 5-1. The energy was calculated from equation (1-2) on p. 27: $\mathcal{E}_{bi}$ [J/unit volume] = $(U_S \cdot i_s)/a_D$; here U_S is the substrate bias, i_s is the substrate ion current density and a_D is the film deposition rate. The energy $\mathcal{E}_{bi}$ is controlled by the negative substrate bias U_S and sputtering gas pressure p since pressure

influences the ratio i_s/a_D. $\mathcal{E}_{bi}$ increases with increasing negative U_S and decreasing p. The increase of $\mathcal{E}_{bi}$ with increasing negative U_S is accompanied by a decrease of the stoichiometry x = Si/Zr of the $ZrSi_x$ films and an increase of their hardness H, see Figure 5-1. The change of the stoichiometry is probably caused by respusttering of light Si atoms from the growing film caused by the increased substrate bias voltage.

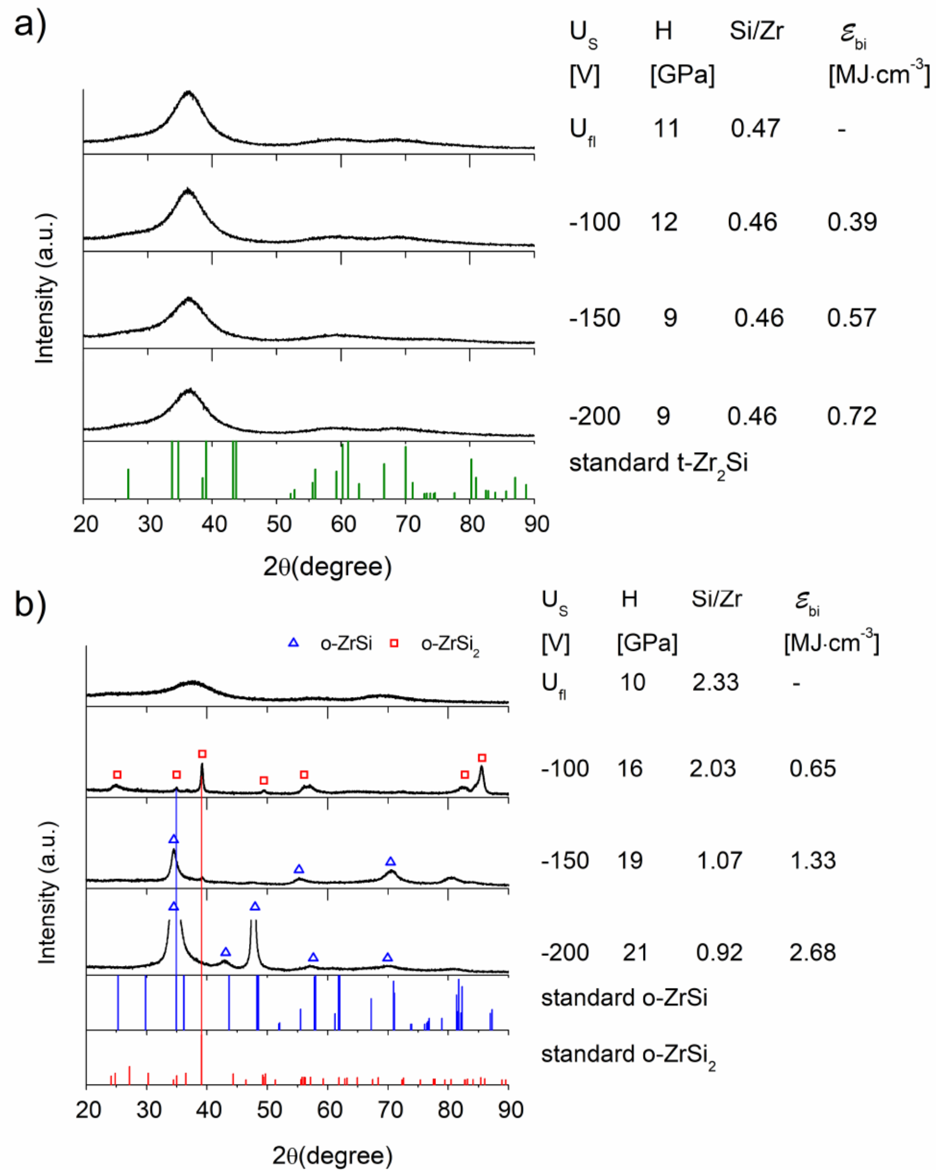

Figure 5-1: Evolution of XRD patterns of the $ZrSi_x$ films with (a) a low ratio Si/Zr ≈ 0.5 and high p = 1.0 Pa and (b) a high ratio Si/Zr ≥ 1 and low p = 0.3 Pa with increasing negative substrate bias U_S.

Table 5-1: Elemental composition, physical and mechanical properties and electrical resistivity of the $ZrSi_x$ alloy films pulsed sputtered at T_S = 300 °C, d_{s-t} = 80 mm and (i) p = 1.0 Pa, U_d = 360 V, W_{tp} = 20 W/cm² and f_r = 10 kHz and (ii) p = 0.3 Pa, U_d = 490 V, W_{tp}= 26 W/cm² and f_r = 100 kHz as a function of negative substrate bias U_S.

U_S [V]	h [nm]	a_D [nm/min]	i_s [mA/cm²]	$\mathcal{E}_{bi}$ [MJ/cm³]	Si [at.%]	Zr [at.%]	Si/Zr	H [GPa]	E^* [GPa]	W_e [%]	H/E^*	σ [GPa]	ρ [Ω·cm]
p = 1 Pa, f_r = 10 kHz													
U_{fl}	2320	77	-	-	29.6	63.2	0.47	11	144	46	0.08	0.74	$2\cdot10^{-4}$
-100	2300	77	0.50	0.39	28.6	62.3	0.46	12	140	50	0.09	-0.40	$2\cdot10^{-4}$
-150	2350	78	0.50	0.57	25.9	55.7	0.46	9	114	50	0.08	-0.29	$3\cdot10^{-4}$
-200	2770	92	0.55	0.72	26.1	56.4	0.46	9	112	50	0.08	-0.54	$3\cdot10^{-4}$
p = 0.3 Pa, f_r = 100 kHz													
U_{fl}	2330	70	-	-	66.8	28.7	2.33	10	145	41	0.07	-0.17	$3\cdot10^{-4}$
-100	1420	69	0.75	0.65	65.0	32.1	2.03	16	187	55	0.09	-0.43	$3\cdot10^{-4}$
-150	2010	51	0.75	1.33	48.8	45.5	1.07	19	182	64	0.10	-1.42	$3\cdot10^{-4}$
-200	2160	36	0.75	2.68	44.7	48.5	0.92	21	178	71	0.12	-2.35	$2\cdot10^{-4}$

From Figure 5-1 and Table 5-1 the following can be observed:

1. The $ZrSi_x$ alloy films sputtered at high pressure p = 1.0 Pa are nanocrystalline, composed of small t-Zr_2Si nanograins of about 1.7 nm. These films are soft ($H \approx 10$ GPa) and exhibit the same stoichiometry $x \approx 0.5$, low values of H/E^* < 0.1 and $W_e \approx 50\%$.
2. The $ZrSi_x$ films sputtered at low pressure p = 0.3 Pa and a floating potential $U_S = U_{fl}$ are X-ray amorphous and soft.
3. The $ZrSi_x$ films sputtered at low pressure p = 0.3 Pa and a negative substrate bias $U_S < 0$ are polycrystalline composed of o-ZrSi or o-$ZrSi_2$ grains. These films are hard ($H > 15$ GPa). They exhibit high values of H, $H/E^* \geq 0.1$, and $W_e > 50\%$ increasing with decreasing x.
4. All the sputtered $ZrSi_x$ alloy films regardless of different stoichiometry are electrically conductive and exhibit a low electrical resistivity of about $2 \cdot 10^{-4}$ Ω·cm. It is worth noting that this value is close to the Mott-Ioffe-Regel limit [126], which says that electrical resistivity corresponds to the wavelength (which is comparable to the mean free path) regardless of detailed structure arrangement.

5.1.1.1 *The microstructure of the sputtered $ZrSi_x$ films*

SEM images of the cross-section microstructure of soft and hard $ZrSi_x$ films sputtered at p = 0.3 Pa are compared, see Figure 5-2.

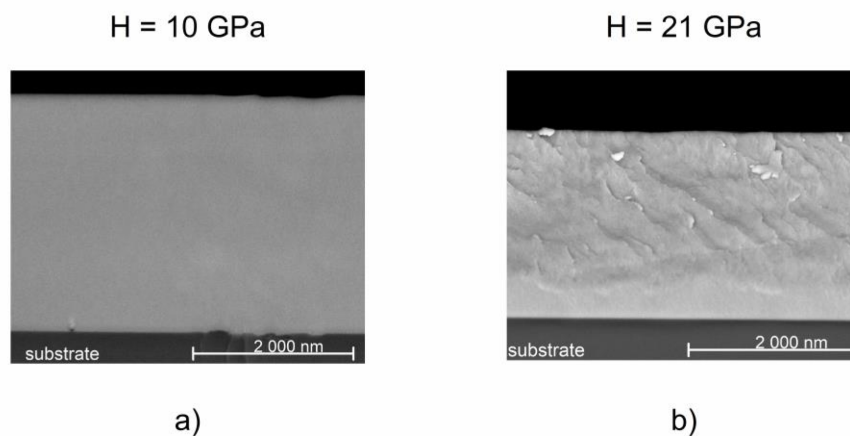

Figure 5-2: SEM images of cross-section microstructure of (a) the soft $ZrSi_x$ alloy film sputtered at $U_s = U_{fl}$ and (b) the hard $ZrSi_x$ alloy film sputtered at $U_s = -200$ V. Both films were deposited on Si(100) substrates at p = 0.3 Pa.

Figure 5-2a displays the soft film with H = 10 GPa sputtered at $U_S = U_{fl}$. Figure 5-2b displays the hard film with H = 21 GPa sputtered at $U_S = -200$ V. The soft film is X-ray amorphous and was created under simultaneous electron and ion bombardment. The hard film is polycrystalline and was created under an ion bombardment at quite high energy $\mathcal{E}_{bi} = 2.68$ MJ/cm^3. Both films exhibit a non-columnar microstructure.

5.1.1.2 The resistance of the sputtered $ZrSi_x$ films to cracking

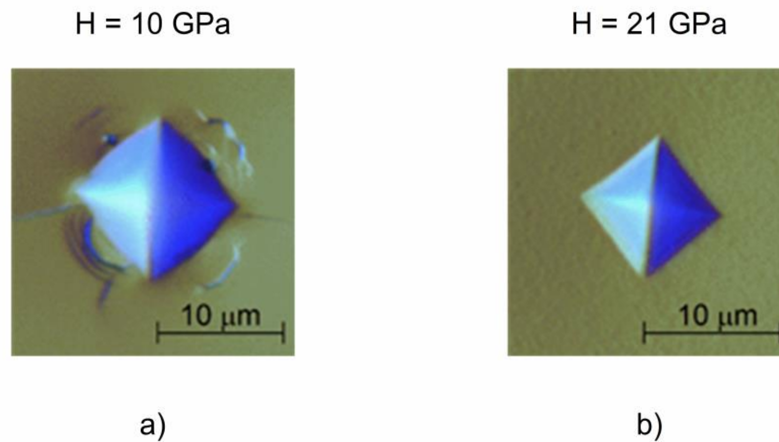

Figure 5-3: Surface morphology of the $ZrSi_x$ films sputtered on Si(100) substrate at p = 0.3 Pa after indentation test with diamond indenter at a high load L = 0.75 N. a) The soft $ZrSi_x$ alloy film with high ratio Si/Zr = 2.33 and H = 10 GPa and low ratio $H/E^* = 0.07$ sputtered at $U_S = U_{fl}$ and (b) the hard $ZrSi_x$ alloy film with Si/Zr = 0.92, H = 21 GPa, and $H/E^* = 0.12$ sputtered at $U_S = -200$ V.

The resistance of the sputtered $ZrSi_x$ film to cracking strongly depends not only on their mechanical properties but also on their microstructure. This fact is illustrated in Figure 5-3 where the resistance to cracking of the soft and hard $ZrSi_x$ alloy films (the same films as in Figure 5-2) is compared. The resistance of the film to cracking is characterized by the imprints of the diamond indenter into the surface of the film under the load L = 0.75 N (see Section 4.3.3). Figure 5-3 clearly shows that while the soft $ZrSi_x$ alloy film with X-ray amorphous structure and non-columnar microstructure cracks, the hard $ZrSi_x$ alloy film with polycrystalline structure and dense, voids-free non-columnar microstructure does not crack under the same diamond indenter load L = 0.75 N. The hard $ZrSi_x$ alloy film exhibits enhanced resistance to cracking due to high values of the ratio $H/E^* = 0.12$, the high elastic recovery $W_e = 71\%$ and the high but still acceptable compressive stress $\sigma = -2.35$ GPa.

5.1.1.3 Properties of the $ZrSi_x$ films controlled by the substrate-to-target distance

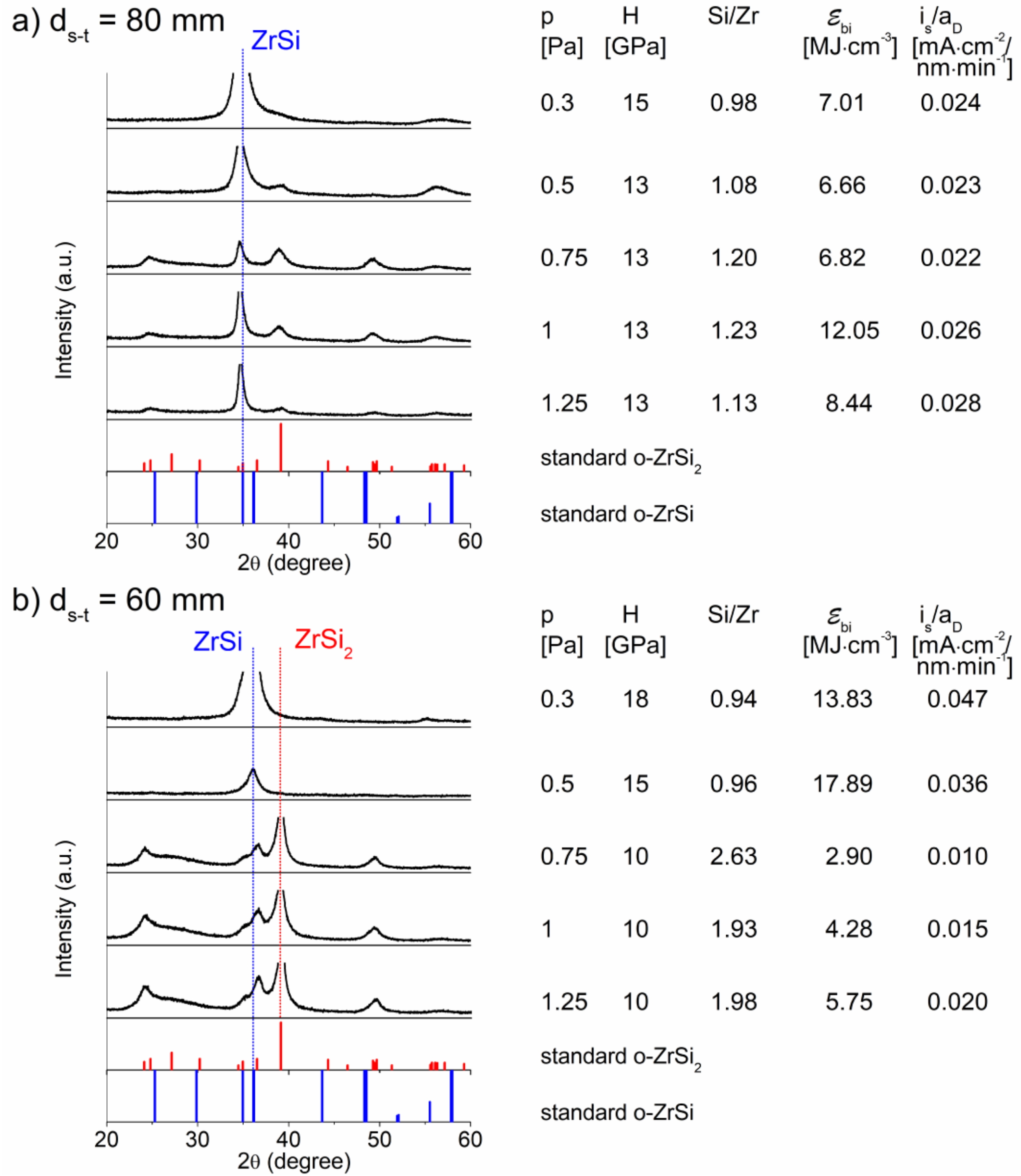

Figure 5-4: XRD patterns of the $ZrSi_x$ films sputtered at T_S = 300 °C, U_S = −500 V, f_r = 100 kHz, τ/T = 0.5, W_{tp} ≈ 21 W·cm^{-2}, (a) d_{s-t} = 80mm and (b) d_{s-t} = 60 mm as a function of argon pressure p.

The properties of the $ZrSi_x$ film strongly depend on its stoichiometry x = Si/Zr and the energy $\mathcal{E}_{bi} \approx (|U_S| \cdot i_s)/a_D$ delivered into the film during its growth. Therefore, both these parameters x and $\mathcal{E}_{bi}$ must be optimized in a sputtering process to form hard $ZrSi_x$ films with H ≥ 15 GPa, W_e ≥ 60%, H/E^* ≥ 0.1 and enhanced resistance to cracking. In this optimization process, the substrate-to-target d_{s-t} distance also plays a great role. The $ZrSi_x$ films were sputtered at W_{tp} = 21 W/cm^2, f_r = 100 kHz, U_S = −500 V and pressure p

ranging from 0.3 to 1.25 Pa, see Figure 5-4 and Figure 5-5. From Figure 5-4 the following main results can be drawn:

1. The hardness H of the sputtered $ZrSi_x$ films correlates well with the ratio i_s/a_D, i.e. with the second term in the equation (1-2) on p. 27: $\mathcal{E}_{bi} \approx (|U_S| \cdot i_S)/a_D$ delivered into the unit volume of the growing film by bombarding ions. It indicates that the ratio i_s/a_D also plays an important role in the analysis of the film properties. The hardness H increases with increasing i_s/a_D.
2. The $ZrSi_x$ films sputtered at $i_s/a_D \leq 0.020$ $mA \cdot cm^{-2}/nm \cdot min^{-1}$ exhibit $x \approx 2$ and preferred o-$ZrSi_2$ texture.
3. The $ZrSi_x$ films sputtered at $i_s/a_D > 0.020$ $mA \cdot cm^{-2}/nm \cdot min^{-1}$ exhibit $x \approx 1$ and preferred o-ZrSi texture.

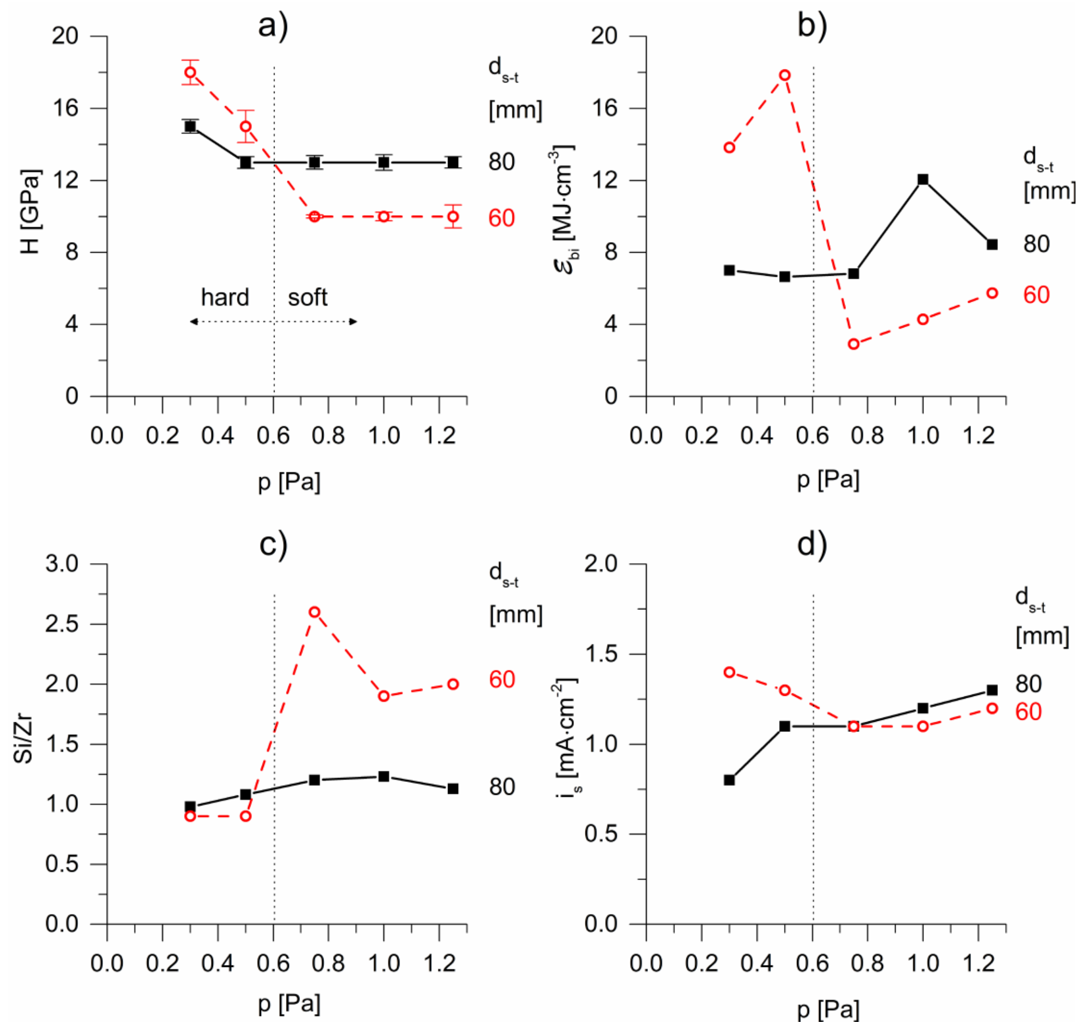

Figure 5-5: Properties of the $ZrSi_x$ film sputtered at $U_S = -500$ V as a function of argon pressure p.
(a) Hardness H, (b) energy $\mathcal{E}_{bi}$, (c) stoichiometry x = Si/Zr and (d) substrate ion current density i_s.

5.1.1.4 Properties of the $ZrSi_x$ films controlled by Ar pressure

Figure 5-5 displays (a) the hardness H of the $ZrSi_x$ films, (b) the energy $\mathcal{E}_{bi}$, (c) the stoichiometry x = Si/Zr of the $ZrSi_x$ films, and (d) the substrate ion current density i_s, as a function of argon pressure p at two values of the substrate-to-target distance, d_{s-t} = 60 and 80 mm. All these dependencies clearly show a strong effect of d_{s-t} on H and x of the sputtered $ZrSi_x$ films due to changes of i_s and $\mathcal{E}_{bi}$ with increasing p. Figure 5-5a shows that the hard $ZrSi_x$ films are formed at low $p \leq 0.6$ Pa due to an increase of i_s and $\mathcal{E}_{bi}$, see Figure 5-5b and d. The transition from soft to hard $ZrSi_x$ films at $p \approx 0.6$ Pa correlates well with the transition from o-$ZrSi_2$ to o-ZrSi preferred texture.

5.1.1.5 Correlations among properties of the $ZrSi_x$ films

The correlations among the properties of ZrS_x films, excluding their dependence on the deposition conditions used in their sputtering, i.e. H, σ, and the ratio Si/Zr, are displayed in Figure 5-6. Measured values of H are compared with those calculated from the rule of mixture (denoted in the following as H theory), i.e. $H_{cal} = H_{Si} \cdot V_{Si} + H_{Zr} \cdot V_{Zr}$; here his = 13.2 GPa and H_{Zr} = 0.9 GPa stand for the hardness of Si and Zr, respectively and V_{Si} and V_{Zr} is the volume of Si and Zr phase, respectively.

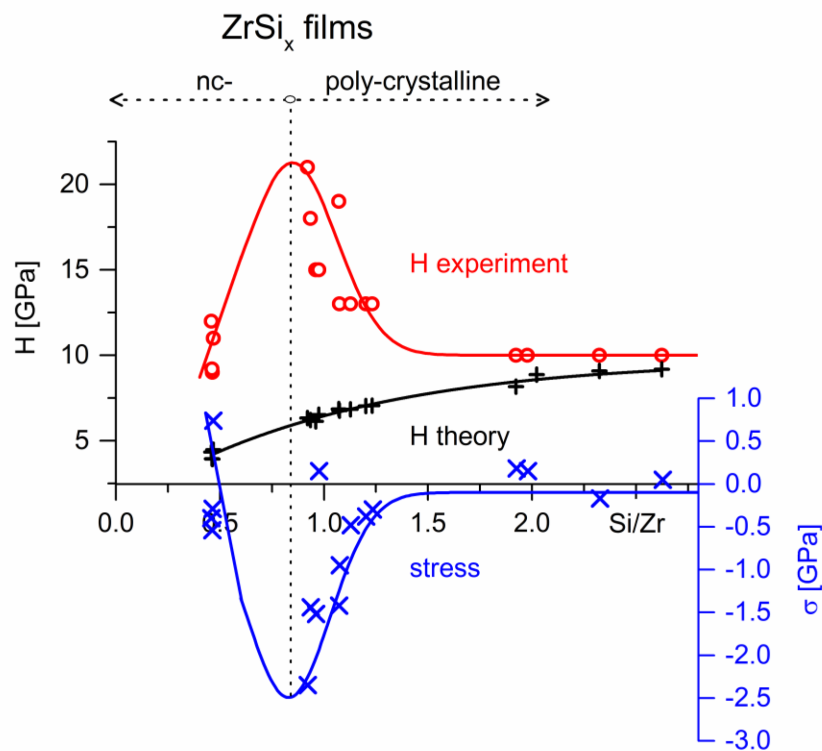

Figure 5-6: Correlations between the mechanical properties and the ratio Si/Zr of $ZrSi_x$ alloy films sputtered on Si(100).

Figure 5-6 gives a new insight into the correlations between the mechanical properties (H, σ) and the elemental composition (x = Si/Zr) of the $ZrSi_x$ films. From this figure the following important results are observed:

1. The hardness approximately follows the rule of mixture only in the case of soft $ZrSi_x$ films with high ratio Si/Zr > 1.5, low hardness (H ≈ 10 GPa) and very low stress σ ≈ 0.
2. The hardness of the $ZrSi_x$ film increases with increasing compressive stress (σ < 0).
3. The $ZrSi_x$ films with Si/Zr slightly below 1 (≈ 0.9) exhibit maximum hardness up to H ≈ 20 GPa.
4. The hardest $ZrSi_x$ films exhibit the highest compressive stress of about −2.5 GPa but still acceptable for protective films.
5. The hardness of the $ZrSi_x$ films with Si/Zr ≤ 0.8 decreases due to a decrease in compressive stress.

5.1.2 Conclusions

This chapter reports on a detailed investigation of the mechanical and electrical properties of the $ZrSi_x$ alloy films sputtered by a dual magnetron. The main aim of this investigation was to find out if there are conditions under which flexible hard Zr-Si alloy films resistant to cracking in the (TM, Met) system can be formed. It was found that the properties of these films strongly depend on their stoichiometry x = Si/Zr, the energy $\mathcal{E}_{bi}$ delivered into the films during their growth and their deposition conditions. The main obtained results are the following.

1. The $ZrSi_x$ alloy films with x = Si/Zr ≈ 1 composed of one metalloid and one metallic element (Met, Me) are hard and resistant to cracking and exhibit considerably higher values of the hardness H, H/E^* ratio and elastic recovery W_e compared with soft and brittle (Me_1, Me_2) alloy films composed of two metallic elements, for instance, the (Zr, Ti) films. A metalloid element tends to create a covalent bond while a metal element creates a metallic bond and this combination has the potential of a stronger bond. Therefore it can be seen that the elemental composition plays an important role and influences the mechanical properties of the (Met, Me) alloy films.

2. The flexible hard $ZrSi_x$ alloy films with $x \approx 1$ exhibit high values of $H \geq 18$ GPa, $H/E^* \geq 0.1$, $W_e \geq 60\%$, non-columnar dense, voids-free microstructure and compressive macrostress ($\sigma < 0$). The high hardness and enhanced crack resistance of films result from a combined action of their elemental composition and compressive stress.
3. The experiment reported in this study shows that the replacement of one metal element in the soft brittle (Me_1, Me_2) alloy film by a metalloid element can remove its brittleness and strongly increase its hardness and resistance to cracking. However, more experiments need to be carried out to demonstrate that this concept of the formation of flexible hard (Me, Met) alloy is of general validity.

5.2 Magnetron sputtering of Mg-Si alloy films and Mg-Si-N nitride films

The following chapter reports on the mechanical properties of Mg-Si alloy films prepared by magnetron sputtering. Cracking is a great drawback of alloy films because it strongly limits many of their practical applications. As was introduced in Chapter 2.3.2, it is shown that hard alloy films resistant to cracking must be superelastic and exhibit a high ratio $H/E^* \geq 0.1$; here H is the hardness and E^* is the effective Young's modulus of the film. As examples, mechanical properties of the Mg-Si-based hard alloy films with enhanced resistance to cracking are given. The effect of the addition of Si and N elements into the single element Mg film on its hardness, and physical and further mechanical properties were investigated in detail.

Presented results are accepted in a special issue of Vacuum "Advances in Vacuum" honouring Professor John S. Colligon.

5.2.1 Results and discussion

5.2.1.1 Physical and mechanical properties of Si and Mg single element, Mg-Si alloy and Mg-Si-N alloy nitride films

The Si and Mg single-element films, the Mg-Si alloy films, and the Mg-Si-N nitride films were investigated in detail to find reasons for the great difference in their physical and mechanical properties. The main aim of this study was to find conditions that allow forming the hard alloy films with a high hardness H ranging from ~15 to ~ 25 GPa and enhanced resistance to cracking, i.e. with high values of the ratio H/E^* (≥ 0.1), elastic recovery W_e ($\geq 60\%$), compressive macrostress ($\sigma < 0$) around -1 GPa that enhances the hardness of the film but does not negatively affect any other film properties such as adhesion of the film to the substrate, and a dense, voids-free non-columnar microstructure (see Chapter 2.3.2). All Mg, Si, Mg-Si, Mg-Si-N, and Si-N films were deposited by a pulsed magnetron sputtering onto Si substrates, which prevents a large mismatch between the mechanical properties of the film and the substrate.

Pure Si and Mg films were sputtered by PDM equipped with M1 made of pure Si and M2 made of pure Mg. During sputtering of Si the magnetron M2 (Mg) was off, during sputtering of Mg the magnetron M1 (Si) was off. Films were sputtered at the substrate temperature $T_S = 200$ °C (473 K), argon pressure $p_T = p_{Ar} = 0.5$ Pa, floating substrate bias

$U_S = U_{fl} \approx 3V$ and substrate-to-target distance $d_{s-t} = 120$ mm. The overview of the deposition conditions is listed in Table 4-2 on page 43.

The deposition rates of sputtered films were $a_{D(Si)} = 33$ nm/min and $a_{D(Mg)} = 133$ nm/min, see Table 5-2. The deposition rate of Mg is considerably higher than that of Si ($a_{D(Mg)} = 4.03\ a_{D(Si)}$). It is in agreement with sputtering yields $\gamma_{Mg} = 2.8\ \gamma_{Si}$ ($\gamma_{Mg} = 1.4$, $\gamma_{Si} = 0.5$). The ratio $a_{D\ Mg}/\ a_{D\ Si}$ is not equal to the ratio $\gamma_{Mg}/\ \gamma_{Si}$ because the discharge power densities on each magnetron were not equal as will be shown further. The hardness of Mg and Si also strongly differ: $H_{Mg} = 1$ GPa and $H_{Si} = 11$ GPa ($H_{Si} = 11\ H_{Mg}$). The data are close to the hardnesses of the bulk materials $H_{Mg} = 0.4$ GPa [127] and $H_{Si} = 12$ GPa [128], however, it can be seen that the hardness of Mg thin film is more than two times higher than that of bulk material which shows the great influence of microstructure of the material on the mechanical properties. The melting temperatures T_m of both elements also strongly differ: $T_{m(Mg)} = 650$ °C (923 K) and $T_{m(Si)} = 1414$ °C (1687 K), i.e. $T_S/T_m = 0.513$ and 0.281 for Mg and Si, respectively. Deposition parameters of sputtered films and their physical and mechanical properties are given in Table 5-2.

From Table 5-2 the following important trends in the evolution of physical and mechanical properties of sputtered films can be observed:

1. The deposition rate a_D of the Mg-Si alloy film composed of two elements decreases if the amount of the second element with a lower sputtering yield added into the first element with higher sputtering yield increases.
2. The soft alloy films exhibit low hardness $H < 10$ GPa and low values of the ratio $H/E^* < 0.1$, $W_e < 60\%$, and tensile ($\sigma > 0$) or a very low compressive macrostress.
3. The addition of N into the Mg-Si alloy film strongly increases its H and the films exhibit high values of ratio $H/E^* \geq 0.1$, $W_e \geq 60\%$, and compressive stress ($\sigma < 0$).
4. Mg films are electrically conductive. The electrical conductivity of the Mg films decreases with the increasing content of Si. The Mg-Si-N and the Si-N films are electrically non-conductive.

Table 5-2: Deposition parameters and properties of the Mg, Mg-Si, Si, Mg-Si-N, and Si-N films sputtered using dual magnetron operated in a pulsed mode (f_r = 100 kHz) at $p_T = p_{Ar} + p_{N2}$, d_{s-t} = 120 mm, T_S = 200 °C and floating substrate bias voltage $U_S = U_{fl}$.

film	p_{Ar} [Pa]	p_{N2} [Pa]	h [μm]	a_D [nm/min]	H [GPa]	E^* [GPa]	W_e [%]	H/E^*	σ [GPa]	Mg [at.%]	Si [at.%]	N [at.%]	T_S/T_m	ρ [Ω·cm]
Mg	0.5	0	2.0	133	1.0	108	6	0.01	0.15	100	0	0	0.513	$7\cdot10^{-5}$
90Mg-10Si	0.5	0	2.3	50	1.3	86	13	0.02	0.33	90	10	0	0.410	$5\cdot10^{-5}$
80Mg-20Si	0.5	0	2.5	56	1.8	92	15	0.02	0.31	80	20	0	0.369	$8\cdot10^{-5}$
35Mg-65Si	0.5	0	2.3	38	6	101	38	0.06	-0.11	35	65	0	0.342	$7\cdot10^{-1}$
15Mg-85Si	1	0	2.8	23	7	109	51	0.06	-0.06	15	85	0	0.299	$8\cdot10^{-1}$
Si	0.5	0	2.0	33	11	125	54	0.09	-0.03	0	100	0	0.281	$2\cdot10^{0}$
20Mg-20Si-60N	0	0.3	1.9	8	21	167	74	0.13	-0.28	20	20	60	0.218 [2]	$> 10^8$
12Mg-24Si-64N	0	0.3	2.2	12	23	176	77	0.13	-0.62	12	24	64	0.218 [2]	$> 10^8$
33Si-67N	0	0.3	2.5	8	26	197	78	0.13	-1.0	0	33	67	0.218 [2]	$> 10^8$

[2] For all Mg-Si-N alloy nitride films the melting temperature $T_{m(Si3N4)}$ = 2173 K was used in the calculation of the homologous temperature T_S/T_m.

The evolution of the hardness H, effective Young's modulus E^* and the ratio H/E^* of sputtered films and their homologous temperatures T_s/T_m as a function of the elemental composition of the Mg-Si alloy and $MgSiN_x$ alloy nitride films is displayed in Figure 5-7.

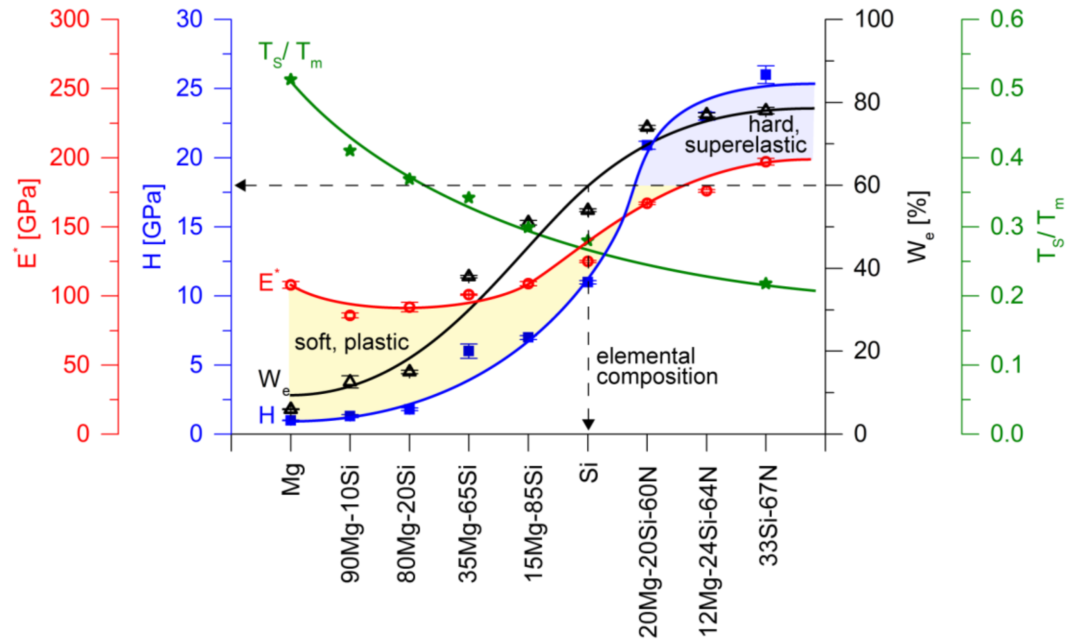

Figure 5-7: Hardness H, effective Young's modulus E^*, elastic recovery W_e, and homologous temperature T_S/T_m of ~2000 nm thick Mg, Mg-Si, Si, Mg-Si-N and Si-N films sputtered using a pulsed dual magnetron (f_r = 100 kHz) at a substrate bias voltage $U_S = U_{fl}$. Hard, superelastic films resistant to cracking are in the region in blue with H ≥ 17 GPa, H/E^* ≥ 0.1 and W_e ≥ 60% and soft, plastic films with high plastic deformation are in the region in yellow with H < 17 GPa, H/E^* < 0.1 and W_e ≤ 55%. The error bars showing the standard deviation have been provided by the software controlling the tester.

Figure 5-7 clearly illustrates three very important facts:

1. The hardness H of the Mg-Si-N increases at first with increasing content of added Si (up to ~10 GPa) and then with the addition of N. For compositions displayed to the left of Si the values of H appear below those of E^* and the elastic recovery W_e are lower than 60%. The addition of Si into Mg is, therefore, still insufficient to form the hard, superelastic (W_e > 60%) Mg-Si films with a high ratio $H/E^* \geq 0.1$ which exhibit enhanced resistance to cracking.
2. The hardness H of the Mg-Si-N films increases with decreasing homologous temperature T_S/T_m and is maximum when the ratio T_S/T_m is minimum. This fact is of key importance for a selection of the elemental composition of a protective alloy film which should be hard, superelastic, and resistant

to cracking. The influence of the homologous temperature on the film properties will be further discussed in detail in Chapter 5.4.

3. The minimum hardness H_{min} of the Mg-Si-N alloy nitride films with enhanced resistance to cracking, i.e. with high values of $H/E^* \geq 0.1$ and $W_e \geq 60\%$ is $H_{min} \approx 17$ GPa.

5.2.1.2 The microstructure of Si, Mg single-element and Mg-Si alloy films

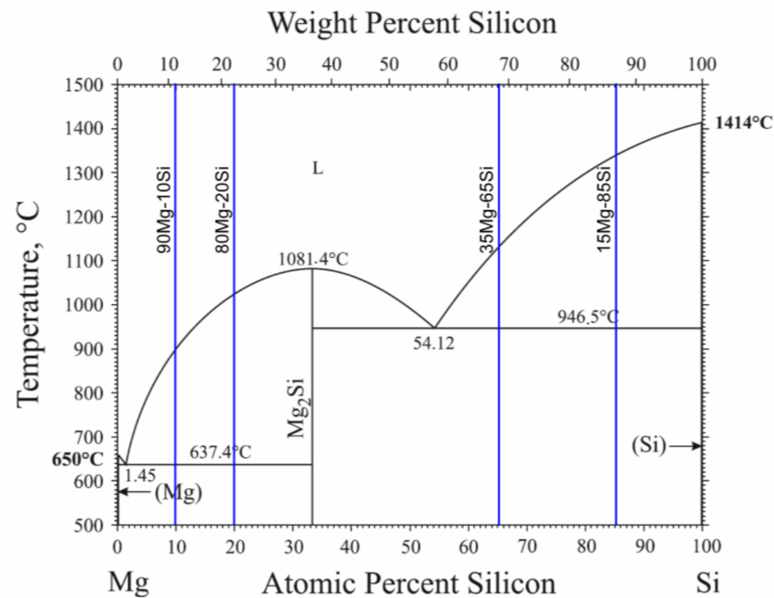

Figure 5-8: Binary phase diagram of the Mg-Si bulk alloy where the discussed Mg-Si films are labelled.

Figure 5-7 shows that the elemental composition of the Mg-Si alloy films strongly influences not only their mechanical properties but also their homologous temperature T_S/T_m. Therefore, it can be expected that the microstructure of the Mg-Si alloy films will depend also on T_S/T_m varying at different Si content. According to the phase diagram of the Mg-Si alloy, the sputtered Mg-Si films are two-phase films composed of ductile and brittle phases. The films with Si content lower than that corresponding to the Mg_2Si phase are composed of a ductile Mg phase and a more brittle Mg_2Si phase and the films with Si content higher than that corresponding to the Mg_2Si phase are composed of that same Mg_2Si phase and a yet more brittle Si phase, see Figure 5-8. The vertical lines in phase diagrams marking a compound, in general, mean that there are nonhomogeneous

phases around the compound (see Chapter 2.2.2). The ductile phases exhibit high values of T_S/T_m due to low melting temperatures and therefore these phases are melted when the films are sputtered at these high values of T_S/T_m. This fact is clearly demonstrated by the evolution of the microstructure of the Mg-Si films displayed in Figure 5-9.

The microstructure of the films prepared at high values T_S/T_m of about ~0.5 to ~0.35 indicates that the film material is formed from its partially melted state. The typical features of the film microstructure displayed in the photos decrease with decreasing T_S/T_m. The microstructure of the film sputtered at T_S/T_m= 0.342 is featureless. The microstructure of the film sputtered at T_S/T_m = 0.280 is similar to that known from a non-melted film material deposited by a standard magnetron technology. The cross-sections thus confirm the expectation stated at the beginning of this section that the homologous temperature provides a link between the microstructure and the mechanical properties of the films.

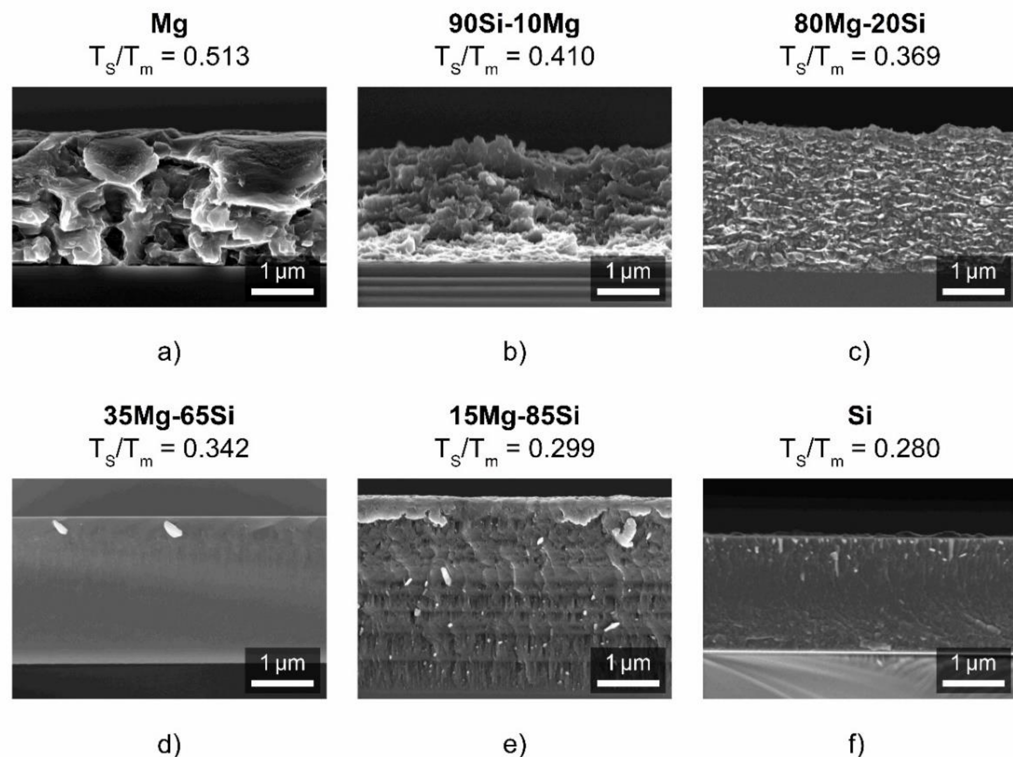

Figure 5-9: Cross-section microstructure of Mg and Si single element films, and the Mg-Si alloy films with increasing Si content deposited on Si(100) substrate.

Figure 5-10 displays the evolution of the structure of sputtered Mg-Si alloy films as a function of increasing Si content and the effect of nitrogen addition into the Mg-Si

alloy on its structure. This figure shows that pure Mg film and Mg-Si alloy films with low Si content are crystalline and that their crystallinity decreases with increasing Si content. Already 65 at.% Si is sufficient to form an X-ray amorphous Mg-Si alloy film. But the sample 15Mg-85Si containing 85 at.% Si violates this trend. Due to the change in deposition parameters (higher pressure p = 1 Pa and lower deposition rate a_D = 23 nm/min), this film is nanocomposite, composed of small Mg and Mg_2Si grains (see the three rather small peaks between about 35° and 40°) embedded in an X-ray amorphous matrix. A pure Si film and all Mg-Si alloy films containing nitrogen are X-ray amorphous again.

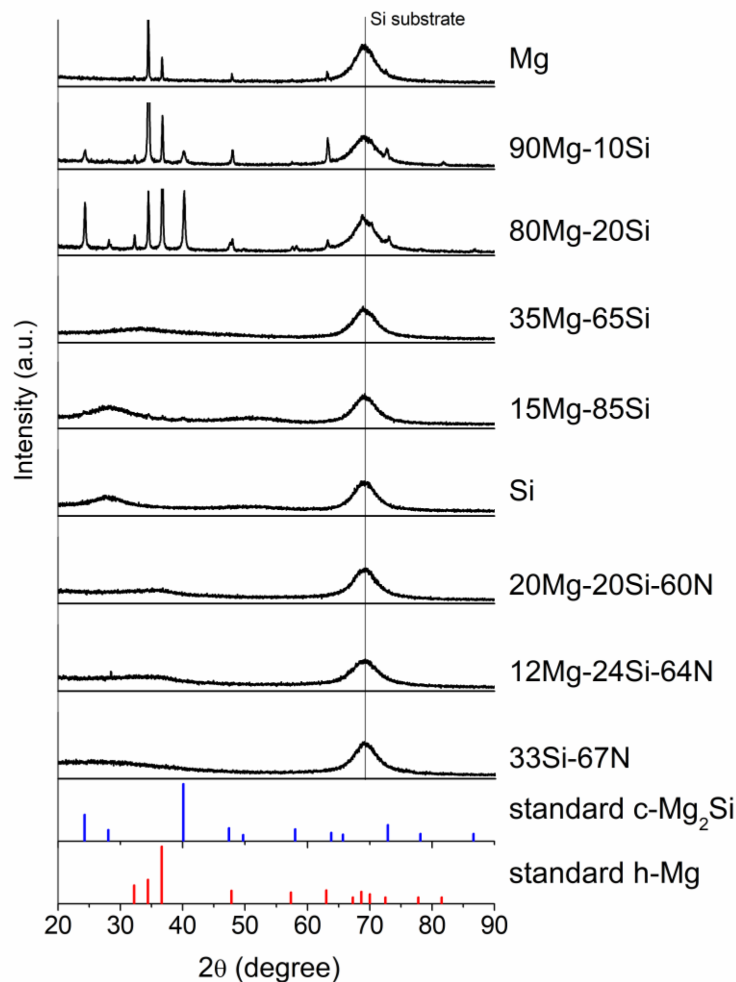

Figure 5-10: XRD patterns of ~2000 nm thick Mg, Mg-Si, Si, Mg-Si-N, and Si-N films sputtered using a dual magnetron system operated in a pulsed mode (fr = 100 kHz) at the floating substrate bias voltage $U_S \approx U_{fl}$.

The hardness H increases with the increasing content of both Si and N and achieves up to 23 GPa for 12Mg-24Si-64N alloy nitride film. Figure 5-11 shows that the microstructure of the 20Mg-20Si-60N alloy film is columnar. The addition of N into Mg-Si alloy films with a ratio Mg/Si ≤ 1 results in the conversion of a columnar microstructure into a dense, feature-less one and in a strong increase of their (i) hardness above 20 GPa up to 27 GPa and (ii) resistance to cracking. This follows the zone diagram interpretation of the transition from columnar to dense microstructure.

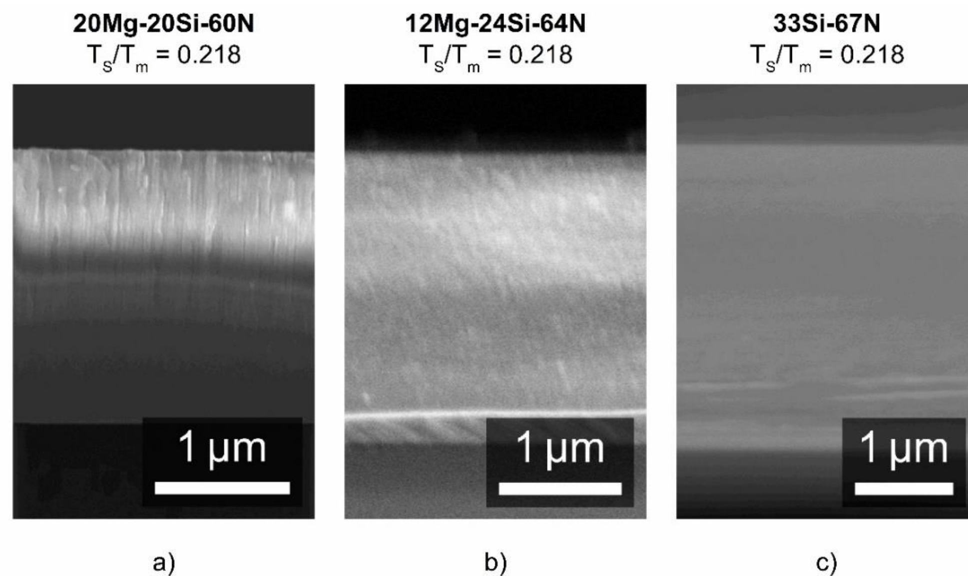

Figure 5-11: Cross-section microstructure of the Mg-Si-N nitride films. Deposition parameters and properties of films are given in Table 5-2.

5.2.1.3 The resistance of Mg-Si alloy and Mg-Si-N nitride alloy films to cracking

The resistance of Mg-Si alloy and Mg-Si-N nitride alloy films to cracking was assessed by an indentation test (see Section 4.3.3). In this test, the surface of the film was loaded normally by a diamond indenter under a high load L of several hundred mN to see whether cracks or deformation zones developed as a result of the loading. Four films were investigated in detail: (1) the Mg film sputtered at $T_S/T_m = 0.513$, (2) the 80Mg-20Si alloy film sputtered at $T_S/T_m = 0.369$, (3) the 12Mg-20Si-60N nitride alloy film sputtered at $T_S/T_m = 0.218$ and (4) the 33Si-67N silicon nitride film sputtered also at $T_S/T_m = 0.218$. The results of these tests are displayed in Figure 5-12, Figure 5-13 and Figure 5-14.

In these figures, photos of the SEM images of the film cross-section microstructure and indentation impresses in its surface are given.

Figure 5-12 illustrates mechanical behaviour of the soft, strongly plastic Mg and 80Mg-20Si films with H = 1 and 1.8 GPa, $W_e \approx 6$ and 15%, and tensile stress $\sigma = 0.15$ and 0.31 GPa, respectively, and significantly different microstructure. Both films exhibit similar behaviour due to their high plasticity. Around the diamond impression, a round diffused deformation zone is formed. The radius of the deformation zone increases with increasing load L. The film material is squeezed out above the film surface, see the pile-up pattern in Figure 5-13. No radial cracks are formed despite that the tip of the diamond indenter already penetrates the substrate. The substrate influences the diamond impression mainly by the effective Young's modulus of the substrate ($E_s^* \approx 200$ GPa for Si(100)) if the ratio E_f^* /E_s^* is close to 1; here E_f^* and E_s^* is the effective Young's modulus of the film and the substrate, respectively. This phenomenon was already demonstrated for transition metal nitride $TMeN_x$ films, see [62]. The plastic 80Mg-20Si alloy films with a dense microstructure exhibit a smaller impression compared with those of the Mg films with voids in the microstructure.

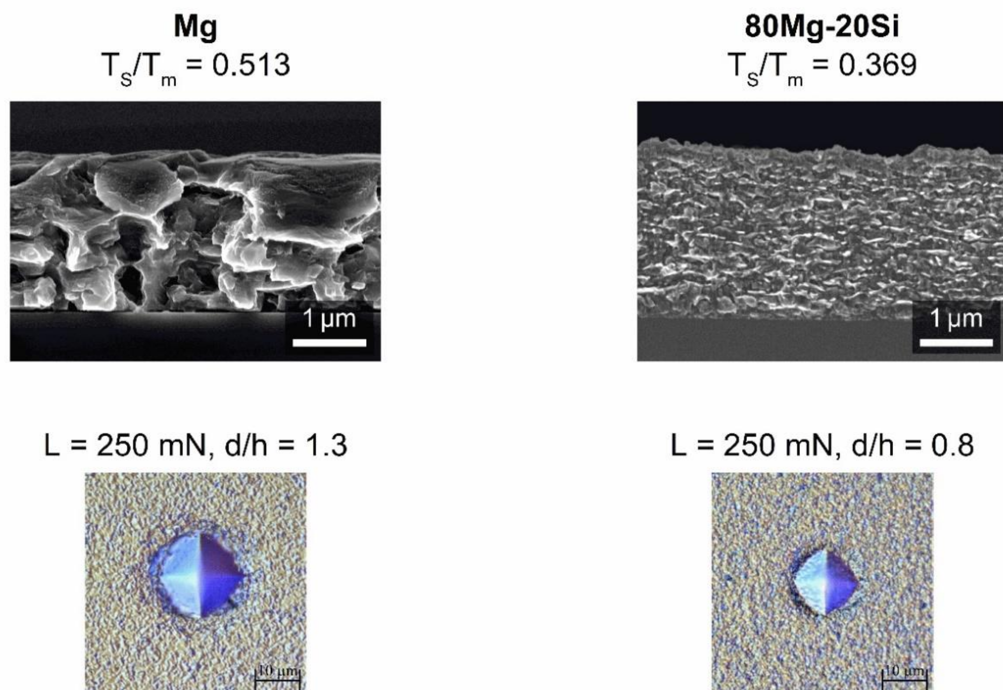

Figure 5-12: Photos of the SEM images of cross-section microstructure and optical images of indentation impression on the surface of soft superplastic (We = 6%) Mg and 80Mg-20Si film deposited on the Si(100) substrate with rare (voids) and dense microstructure at indenter diamond load L = 250 mN. d/h is the ratio of the impression depth d to the film thickness h.

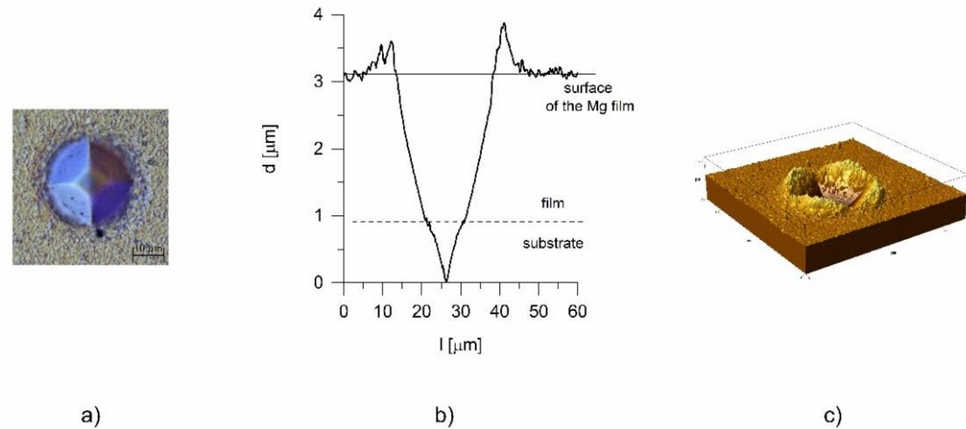

Figure 5-13: a) Optical image of the diamond impress into the surface of soft, superplastic (We = 6%), pure Mg film, (b) its depth profile, and (c) imprint topography surface taken by atomic force microscope.

Figure 5-14 illustrates the mechanical behaviour of the hard, superelastic ($W_e > 60\%$) 12Mg-20Si-60N alloy nitride and 33Si-67N silicon nitride films with H = 21 GPa and 26 GPa and W_e = 74 and 78%, compressive stress σ = -0.28 and -1.0 GPa, and columnar and dense microstructure, respectively. Both films exhibit similar behaviour due to their high hardness and elasticity. The films were investigated by an indentation test at RT and load L ranging from 250 mN to 1000 mN. It was found that:

1. The 20Mg-20Si-60N alloy nitride film exhibits low resistance to cracking and cracks occur already at L = 250mN. Cracks in the corners of the diamond impress are clearly seen. This film is brittle and its cracking is caused by its columnar microstructure. The superelasticity of these films is insufficient to prevent their cracking. This finding is of key importance; for more details see [45], [46].
2. The 33Si-67N silicon nitride film exhibits dense, non-columnar microstructure and exhibits no cracks even at L = 1000 mN. These films are hard, superelastic, and exhibit enhanced resistance to cracking.
3. The increase of the diamond indenter load L results in an increasing area of the diamond impression.

Figure 5-15 shows the details of the indentation pattern analogous to those shown in Figure 5-13, but for the hard superelastic Si-N nitride film from Figure 5-14. Hence neither the pile-up pattern nor the radial cracks are observed.

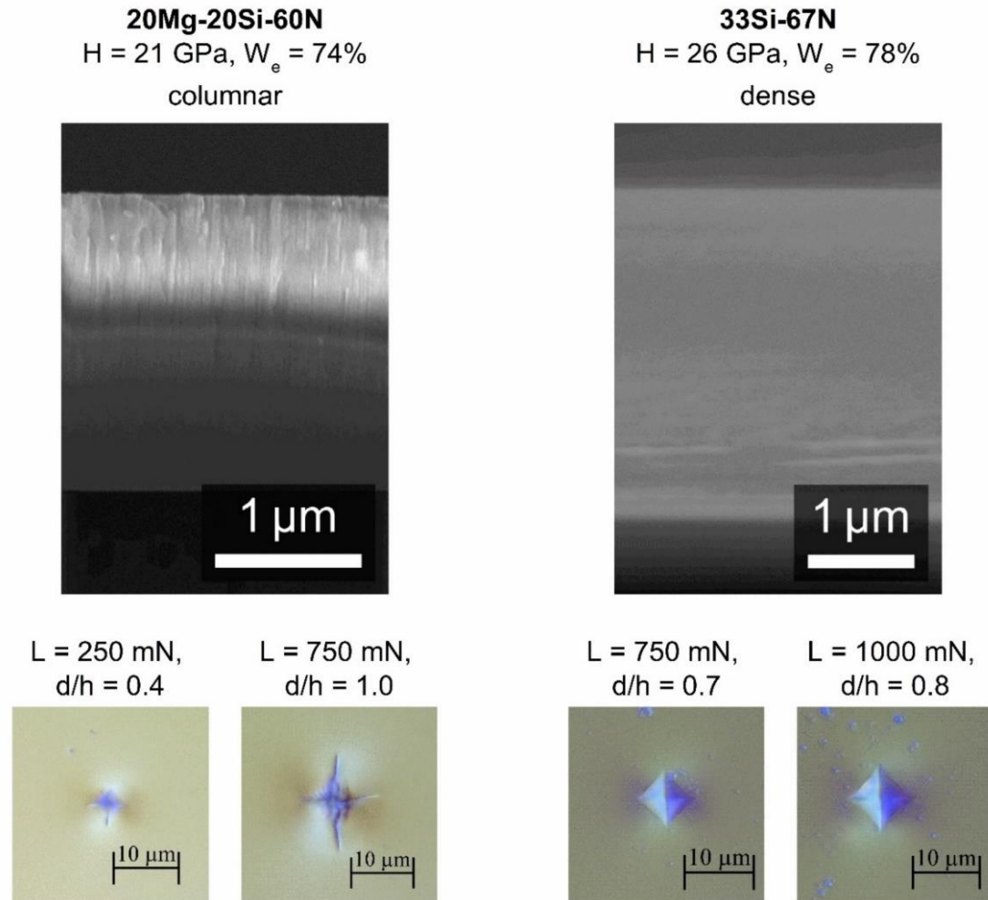

Figure 5-14: Photos of the SEM images of cross-section microstructure and optical images of indentation impression on the surface of hard superelastic (We >60%) Mg-Si-N and Si-N nitride films deposited on the Si(100) substrate with columnar and dense microstructure at indenter diamond load L ranging from 250 to 1000 mN. d/h is the ratio of the depth impression d to the film thickness h.

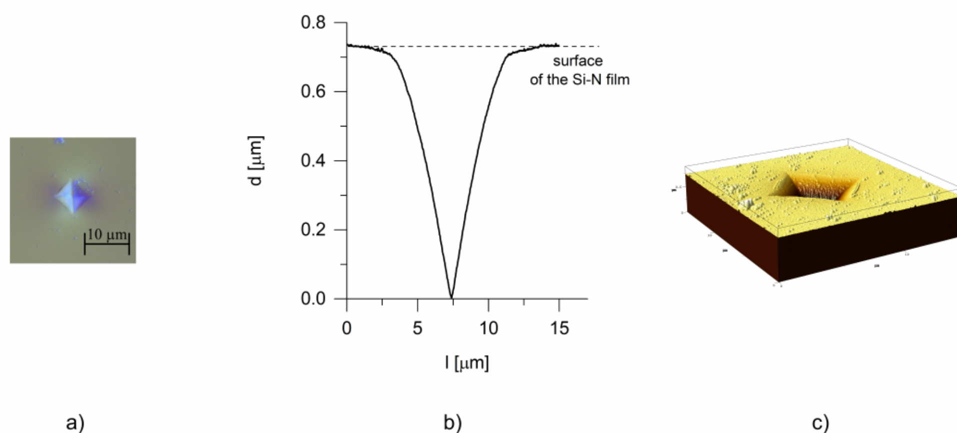

Figure 5-15: a) Optical image of the diamond impress into the surface of hard, superelastic (We > 60%), pure Si-N nitride film, (b) its depth profile, and (c) imprint topography surface taken by atomic force microscope.

5.2.2 Conclusions

These experiments clearly demonstrated that Mg-Si alloy films are soft with maximum hardness H < 10 GPa, exhibit low values of the ratio H/E^* < 0.1, W_e < 60%, tensile macrostress and columnar microstructure and easily crack. The hardness H of Mg-Si alloy films and their resistance to cracking can be increased only in the case when N is incorporated into Si or the Mg-Si alloy film and the SiN_x or $MgSiN_x$ nitride film is formed. The main obtained results can be briefly summarized as follows:

1. The hardness H of the alloy film strongly depends on the homologous temperature T_S/T_m of its material.
2. The hardness H of a single element or an alloy film can be increased above ~10 GPa in the case when the element with a higher melting temperature T_m is added into the single element or the alloy film.
3. The highest hardness of the single element or a soft alloy film is achieved if T_S/T_m is minimum.
4. The Si and N are typical elements that strongly increase the H of sputtered films. This fact was experimentally demonstrated in the sputtering of Zr-Si alloy film (see Chapter 5.1) and Mg-Si-N nitride alloy film in this study.
5. The addition of Si and N into the Mg single element film is a very effective way to sputter hard alloy films with H up to ~ 27 GPa resistant to cracking.

In summary, it can be concluded that the addition of Si and N into an alloy with two or more elements convert soft brittle alloy into hard, superelastic alloy resistant to cracking even at room temperature.

5.3 Physical and mechanical properties of SiN_x nitride films prepared by magnetron sputtering

This section is devoted to the study of SiN_x films, especially to the correlations between their deposition parameters and properties. It is shown that it is possible to reactively sputter SiN film with high hardness up to 32 GPa and enhanced resistance to cracking. The influence of the substrate temperature and partial pressure of nitrogen during the deposition on the mechanical properties are discussed in detail. This study is linked to the previous research discussed in Chapter 5.2, these two chapters together constitute one project focused on hard films with enhanced resistance to cracking and the results are also part of the paper accepted in a special issue of Vacuum "Advances in Vacuum" honouring Professor John S. Colligon.

5.3.1 Results and discussion

The sputtering of SiN_x nitride films was investigated with the aim to increase their (i) adhesion to Si(100) substrates and (ii) hardness H using an ion bombardment during their growth. Special attention was also devoted to the effect of the energy of ion bombardment $\mathcal{E}_{bi}$ on the evolution of mechanical properties of the SiN_x films with increasing substrate temperature T_S, i.e. with increasing homologous temperature T_S/T_m induced by the substrate heating and with increasing N content in the SiN_x film; x = N/Si. The overview of the deposition conditions is listed in Table 4-3 on page 43.

5.3.1.1 Substrate bias voltage

The hardness of Mg-Si-N films achieved maximum values of 23 GPa (see Table 5-2 on page 57 and Figure 5-7 on page 58). For further increase of hardness, the Si-N films without the addition of Mg were prepared. To investigate the effect of the energy of ion bombardment $\mathcal{E}_{bi}$, the Si-N films were sputtered with a pulsed bias voltage with alternating negative and positive pulses. Firstly, a repetition frequency f_{rs} = 50 kHz was used but the transition time between negative and positive pulse was too long (see Figure 5-16a) and the macrostress relaxation that occurs due to electron bombardment during the positive pulse was not sufficient. Therefore the repetition frequency was decreased to f_{rs} = 5 kHz – see Figure 5-16b. It can be clearly seen that the transition between positive and negative pulse is much less significant compared to the time of the pulses. The next

parameter which had to be set carefully is the duty cycle. When the pulsed bias voltage was applied with $\tau^{-}/\tau^{+} = 50/50$, the adhesion of the films to the substrate was very poor due to a high value of compressive macrostress, here τ^{-} and τ^{+} stand for the length of the negative and positive pulse. To decrease the compressive stress, the duty cycle was changed to $\tau^{-}/\tau^{+} = 25/75$. A decrease of the time of the negative pulse results in a decrease of the compressive macrostress from -1.68 GPa to lower negative values and the adhesion to the substrate was increased – see Table 5-3. During negative pulses, the growing film is densified but its compressive stress also increases, which results in its delamination from the substrate. Therefore, during positive pulses, the compressive stress must be relaxed by electron heating to prevent the delamination of the film from the substrate.

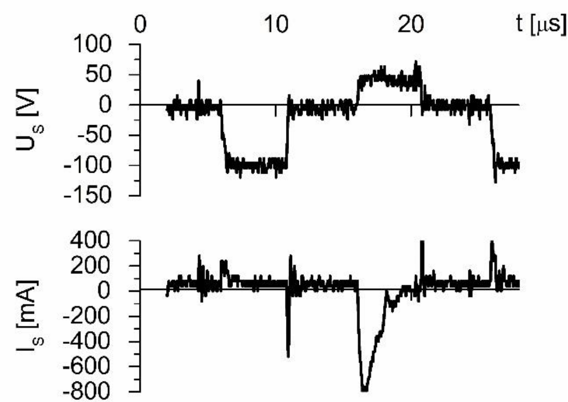

a) $f_{rs} = 50$ kHz

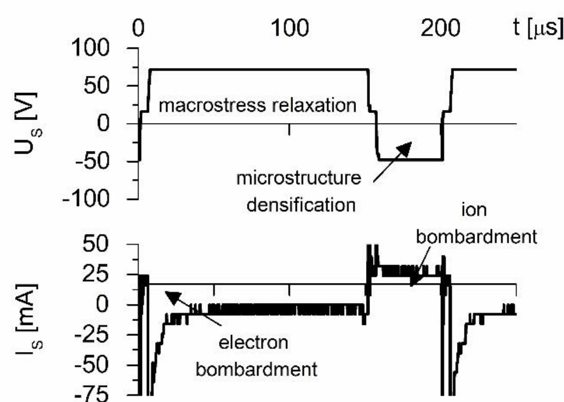

b) $f_{rs} = 5$ kHz

Figure 5-16: Waveforms of the pulsed bias at a repetition frequency of a) $f_{rs} = 50$ kHz, b) $f_{rs} = 5$ kHz.

Table 5-3: Deposition parameters and properties of Si-N films sputtered using dual magnetron operated with asynchronous pulses at f_r = 100 kHz, τ/T = 0.5 at $p_T = p_{N2}$ = 0.3 Pa, d_{s-t} = 120 mm, pulsed substrate bias voltage $U_S = U_S^-$ or U_S^+ with lengths of negative pulse τ^- and positive pulse τ^+ at f_{rs} = 5 kHz.

U_S [V]	τ^-/τ^+	T_S [°C]	h [µm]	a_D [nm/mm]	i_s [mA/cm^2]	$\mathcal{E}_{bi}$ [MJ/cm^3]	i_s/a_D [mA/cm^2/ nm·min^{-1}]	H [GPa]	E^* [GPa]	W_e [%]	H/E^*	σ [GPa]	delamination
U_{fl} ≈ 3 V	-	200	2.53	8	-	-	-	26	197	78	0.13	-1.00	no
-50/+50	50/50	200	2.36	7	0.20	0.759	0.025	28	197	82	0.14	-1.68	yes
-50/+50	25/75	100	2.30	9	0.338	1.189	0.040	26	192	79	0.14	-1.64	no
-50/+50	25/75	200	2.18	8	0.338	1.254	0.042	27	193	80	0.14	-1.25	no

5.3.1.2 Mechanical properties of Si-N films and their correlation to energy on ion bombardment

The energy of ion bombardment delivered to the growing film $\mathcal{E}_{bi}$ increases the substrate temperature T_S and thus increases the ratio T_S/T_m. A higher energy $\mathcal{E}_{bi}$ providing material heating as an alternative to the substrate heating quantified by T_S not only increases the H of the sputtered film but also can lower its mismatch with the substrate to avoid its delamination from the substrate.

It was shown that the SiN_x films with high values of H ≈ 26 GPa, $H/E^* = 0.14$ and $W_e = 80\%$ can be sputtered under ion bombardment during their growth. As was explained above, this deposition process requires to select correctly the length of negative and positive pulses, see Table 5-3. The energy delivered into the growing film can be calculated from the formula (1-2) $\mathcal{E}_{bi} = (U_S i_s)/a_D$; here U_S and i_s are the bias voltage and the substrate ion current density on the growing film during the negative pulse.

Figure 5-17 shows the evolution of the hardness H of the SiN_x as a function of increasing a) substrate temperature T_S at a constant nitrogen pressure $p_{N2} = 0.3$ Pa and b) the content of N at a constant substrate temperature $T_S = 100$ °C. The constant values of p_{N2} and T_S were chosen because a) $p_{N2} = 0.3$ Pa enables sputtering of Si-N films with the desired elemental composition and highest hardness, b) the properties of the films sputtered at low homologous temperatures T_S/T_m are important for this research as was shown in Chapter 5.2 and as will be further investigated in detail in the following Chapter 5.4, so the low $T_S = 100$ °C was used. The deposition parameters are summarized in Table 5-4 and Table 5-5. Figure 5-17 thus compares the evolution of H, E^*, H/E^* and σ of the SiN_x films as a function of T_S and as a function of p_{N2}. This comparison shows that:

1. The films in the dependence $SiN_x = f(T_S)$ exhibit high values of H > 20 GPa, $H/E^* > 0.1$ and $W_e > 60\%$ and compressive macrostress ($\sigma < 0$). It means that the SiN_x nitride films are hard, superelastic, and exhibit enhanced resistance to cracking.
2. The ratio H/E^* of films in the dependence $SiN_x = f(p_{N2})$ increases with increasing p_{N2} and only at $p_{N2} \geq 0.15$ Pa achieves $H/E^* > 0.1$. It means that for the formation of SiN_x films with enhanced resistance to cracking a higher content of N is necessary.
3. The compressive macrostress can be reduced by decreasing (i) the substrate temperature T_S or (ii) the content of N in the SiN_x film. It means that

the formation of hard, superelastic SiN_x film resistant to cracking must be optimized.

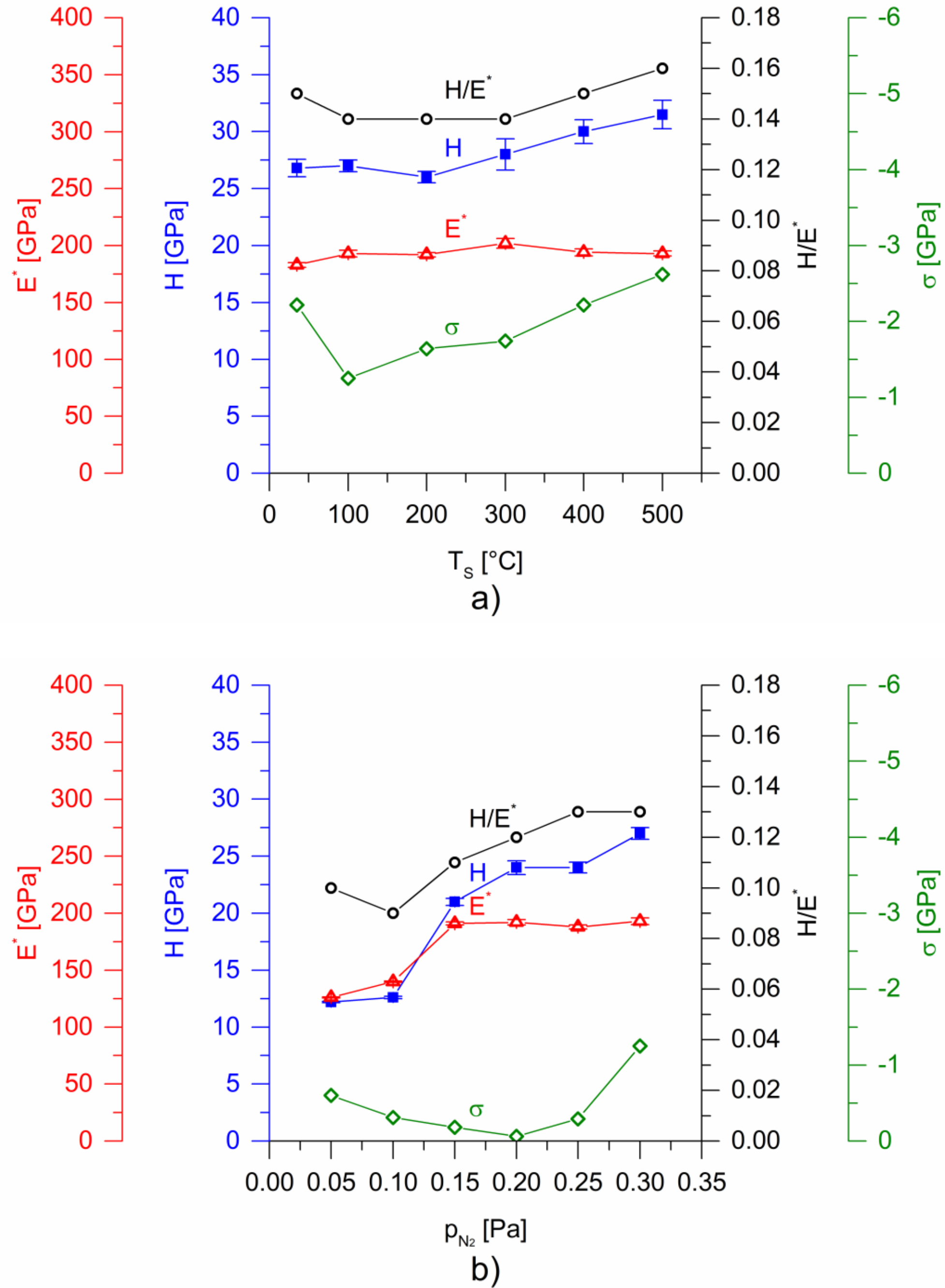

Figure 5-17: Hardness H and effective Young's modulus E^* of the ~2000 nm thick Si-N films sputtered using dual magnetron system operated in a pulsed mode (f_r = 100 kHz) at a pulsed substrate bias voltage $U_S \approx$ -50 /+50 V, $p_T = p_{Ar} + p_{N2}$ = 0.3 Pa as a function of a) substrate temperature T_S and b) partial pressure of nitrogen p_{N2}.

Table 5-4: Deposition parameters and properties of Si-N films with ~33 at.% Si and ~67 at.% N sputtered using dual magnetron operated with asynchronous pulses at f_r = 100 kHz, τ/T = 0.5 at $p_T = p_{N2}$ = 0.3 Pa, d_{s-t} = 120 mm, pulsed substrate bias voltage with alternating negative and positive pulses $U_S = U_S^-$ (-50 V) or U_S^+ (+50 V) with lengths of negative pulse τ^- and positive pulse τ^+ at f_{rs} = 5 kHz, where τ^-/τ^+ = 25/75 as a function of the substrate temperature T_S.

T_S [°C]	h [µm]	a_D [nm/min]	i_s [mA/cm^2]	$\mathcal{E}_{bi}$ [MJ/cm^3]	i_s/a_D [mA/cm^2/ nm·min^{-1}]	H [GPa]	E^* [GPa]	W_e [%]	H/E^*	σ [GPa]
RT	2.30	9	0.388	1.365	0.045	27	183	82	0.15	-2.22
100	2.18	8	0.338	1.254	0.042	27	193	80	0.14	-1.25
200	2.30	9	0.338	1.189	0.040	26	192	79	0.14	-1.64
300	1.99	7	0.338	1.374	0.046	28	202	82	0.14	-1.74
400	2.01	7	0.388	1.562	0.052	30	194	87	0.15	-2.22
500	2.07	8	0.363	1.418	0.047	32	193	90	0.16	-2.62

Table 5-5: Deposition parameters and properties of Si-N films sputtered using dual magnetron operated with asynchronous pulses at f_r = 100 kHz, τ/T = 0.5 at $p_T = p_{N2} + p_{Ar}$ = 0.3 Pa, T_S = 100 °C, d_{s-t} = 120 mm, $T_S/T_{m(Si3N4)}$ = 373/2173 = 0.17, pulsed substrate bias voltage with alternating negative and positive pulses $U_S = U_S^-$ (-50 V) or U_S^+ (+50 V) with lengths of negative pulse τ^- and positive pulse τ^+ at f_{rs} = 5 kHz, where τ^-/τ^+ = 25/75 as a function of partial pressure of nitrogen p_{N2}.

p_{N2} [Pa]	p_{Ar} [Pa]	h [μm]	a_D [nm/min]	i_s [mA/cm^2]	$\mathcal{E}_{bi}$ [MJ/cm^3]	H [GPa]	E^* [GPa]	W_e [%]	H/E^*	σ [GPa]	Si [at.%]	N [at.%]
0.05	0.25	2.13	30	0.125	0.123	12	126	58	0.10	-0.60	85	15
0.10	0.20	2.51	28	0.300	0.323	13	140	56	0.09	-0.31	75	25
0.15	0.15	3.98	22	0.300	0.419	21	191	68	0.11	-0.18	37	63
0.20	0.10	2.95	11	0.388	1.064	24	192	76	0.12	-0.06	33	67
0.25	0.05	2.26	8	0.325	1.165	24	188	75	0.13	-0.29	34	66
0.30	0	2.18	8	0.338	1.254	27	193	80	0.13	-1.25	34	66

Besides the investigation of the mechanical properties, the resistance to cracking of the Si-N film was assessed by an indentation test. As can be seen in Figure 5-14 and Figure 5-15 on page 65, the Si-N films exhibit dense, voids-free microstructure and do not crack even at very high load L = 1000 mN.

5.3.2 Conclusions

The conclusions obtained in Chapter 5.1 and especially in Chapter 5.2 were confirmed. The previous research on Mg-Si(-N) films was followed up by the present study on Si-N films. It was shown that at precisely controlled deposition conditions it is possible to reactively sputter Si-N films which are hard with H up to 32 GPa, superelastic, and exhibit enhanced resistance to cracking. A critical parameter is the compressive macrostress which on the one side enhances the hardness; however, when it is too high, it can lead to delamination of the film from the substrate.

The main results are:

1. It is possible to reproducibly sputter hard Si-N film with high hardness H = 32 GPa, high ratio H/E^* = 0.16, high elastic recovery W_e = 90% and dense, voids-free microstructure. The Si-N films exhibit enhanced resistance to cracking.
2. Low values of T_S/T_m can be achieved either by a high T_m of film material or by a decrease of T_S. However, the use of a high T_S is not optimal for the production of hard alloy films because a crystalline material is formed by slow cooling from the melted film material at high T_S. In this case, a high energy $\mathcal{E}_{bi}$ must be delivered into a growing film that is accompanied by a strong increase in its compressive stress and problems with the film delamination from the substrate.

5.4 Effect of melting temperature T_m on properties of hard alloy coatings resistant to cracking

The results in the following sections put together findings from previous experiments (presented in previous chapters) in order to find a generally valid method to sputter hard alloy film with enhanced resistance to cracking. The homologous temperature T_S/T_m and its influence on the mechanical properties of the alloy films are discussed in detail.

The structural zone diagram (SZD) of coatings provides a dependence of their microstructure on the melting temperature T_m via the dependence on (i) the homologous temperature T_S/T_m and (ii) the energy $\mathcal{E}_{bi}$ delivered into them by bombarding ions as was described in Section 2.2.1; here T_s is the substrate temperature. The melting temperature T_m of hard coatings strongly varies with their elemental composition as can be seen from the composition-temperature phase diagrams of the coating materials. It means that the elemental composition influences microstructure and mechanical properties of coatings deposited at the same value of T_S. It was found that the minimum value of $(T_S/T_m)_{min}$ of the curve $T_S/T_m = f$ (elemental composition) determines an optimal elemental composition of the coating with a maximum hardness H_{max}. This finding makes it possible to find easily the correct elemental composition which ensures that the binary alloy coating composed of two elements with H_{max} can be formed. This fact was experimentally demonstrated in sputtering of hard, superelastic ZrSi alloy and Mg-Si-N alloy nitride coatings with enhanced resistance to cracking at room temperature (RT) (see previous Chapter 5.1 and Chapter 5.2). Deposition conditions under which such coatings can be created are given.

The results are prepared for publication.

5.4.1 Microstructure vs. pressure p, homologous temperature T_S/T_m and energy $\mathcal{E}_{bi}$

The dependence of the coating microstructure on the argon pressure p, homologous temperature T_S/T_m, and the energy $\mathcal{E}_{bi}$ is schematically illustrated in Figure 5-18. This figure shows the structural zone diagram (SZD) of sputtered films proposed by J.A. Thornton in 1977 [29]. As was described in Section 2.2.1, there are five main characteristics of the film microstructure:

1. There are four zones: (1) zone 1 – columnar microstructure, (2) transition zone T – dense, voids-free, non-columnar microstructure, (3) zone 2 composed of the columnar grains separated by dense inter-crystalline boundaries [28] and (4) zone 3 composed of the recrystallized grain structure.
2. The borderlines between individual zones increase with increasing pressure p.
3. The films created at the boundary curve $(T_s/T_m)_{\sigma=0} = f(p)$ between the zone 1 and the zone T exhibit zero macostress ($\sigma = 0$).
4. The films in zone 1 are in tension ($\sigma > 0$) and those in the zone T are in compression ($\sigma < 0$).
5. The boundary curve $(T_S/T_m)_{\sigma=0} = f(p)$ is created at the critical energy $\mathcal{E}_{bi} = \mathcal{E}_c$ [129] and can be shifted to lower values T_S/T_m at $\mathcal{E}_{bi} > \mathcal{E}_c$ and to higher values T_S/T_m at $\mathcal{E}_{bi} < \mathcal{E}_c$ what means that the zone 1 can be compressed or expanded.

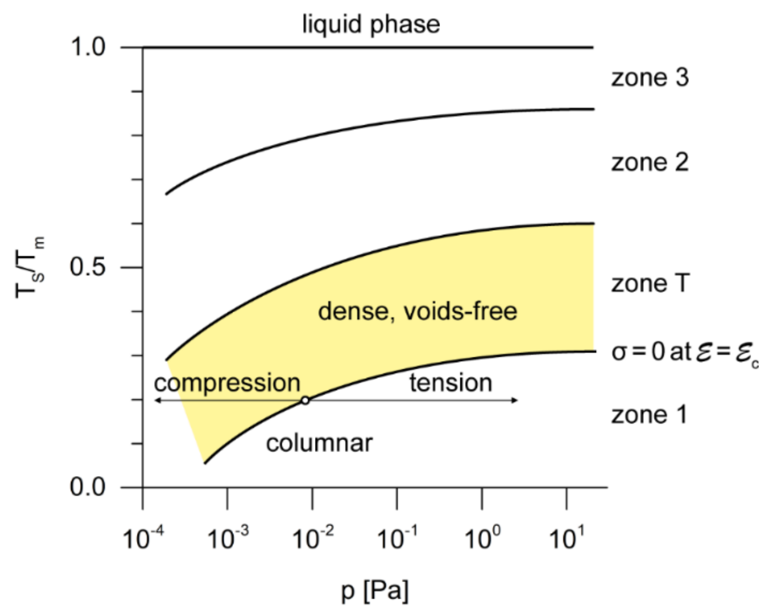

Figure 5-18: Structural zone model (SZD) of sputtered films proposed by J.A. Thornton. Adapted after Ref. [29].

The dependence of the critical energy $\mathcal{E}_c$ on the value of T_S/T_m was demonstrated experimentally for the α-Ti(N) and δ-$TiN_{x\approx1}$ films sputtered in $Ar+N_2$ mixture at $T_S = 350$ °C and constant pressure $p_T = p_{Ar}+p_{N2} = 5$ Pa, see Figure 5-19. This figure shows the evolution of the macrostress σ of Ti(N) and δ-$TiN_{x\approx1}$ films as a function of the energy $\mathcal{E}_{bi}$. This experiment clearly demonstrates that:

1. There is a critical energy $\mathcal{E}_c$ at which the sputtered coating exhibits zero stress, i.e. $\sigma = 0$ at $\mathcal{E}_{bi} = \mathcal{E}_c$.
2. The value of $\mathcal{E}_c$ decreases with decreasing T_S/T_m ratio.
3. The coatings sputtered at $\mathcal{E}_{bi} < \mathcal{E}_c$ exhibit tensile stress ($\sigma > 0$). On the other hand, the coatings sputtered at $\mathcal{E}_{bi} > \mathcal{E}_c$ exhibit compressive stress ($\sigma < 0$).
4. The stress σ increases with increasing T_S/T_m ratio.
5. The films in tension exhibit a columnar microstructure but only in the case when $\mathcal{E}_{bi}$ is sufficient for their crystallization and those in compression exhibit dense, voids-free non-columnar microstructure.

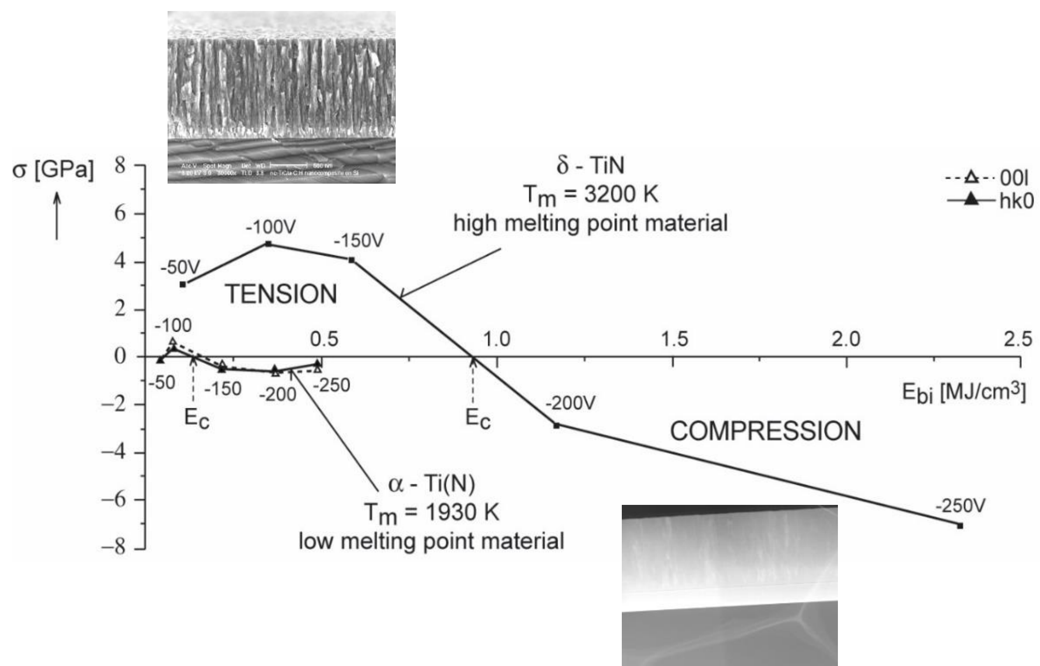

Figure 5-19: Macrostress σ and microstructure of sputtered α-Ti(N) and δ-$TiN_{x\approx1}$ films as a function of the energy $\mathcal{E}_{bi} = U_s i_s/a_D$ at $p_T = p_{Ar} + p_{N2} = 5$ Pa and $T_S = 350$ °C, i.e. at $T_S/T_m = 0.32$ and 0.19 for α-Ti(N) and δ-$TiN_{x\approx1}$, respectively. Adapted after reference [129].

5.4.2 Melting temperature T_m vs. elemental composition of binary alloys

To illustrate the general concept of the dependence of the melting temperature T_m of alloy on its elemental composition, we shall consider the simplest case of binary alloys. We shall use the $ZrSi_x$ alloy as an example (see Chapter 5.1); here x = Si/Zr is the alloy stoichiometry, see its phase diagram in Figure 5-20. There are several solid zirconium-silicide compounds. As was explained in Section 2.2.2, the highest temperature of stability of each such compound is either a point of equal concentration or a triple

point. In the case of $ZrSi_x$ the highest temperature of only one compound, βZr_5Si_4, close to the middle of the composition range at $x_{max} = 0.8$ or 55.6 at.% Zr and at 2250 °C, point A in Figure 5-20, is a point of equal concentration with the liquid. The highest temperatures of all the other compounds give rise to triple points with only mild decreases of the melting-curve slope, in absolute value, at these points. The $ZrSi_x$ alloy possesses additional two triple points with eutectic points close to pure elements (in each case at about 10 at.% of the minority element) and at similar temperatures of 1370 °C and 1570 °C, points B and C, respectively, in Figure 5-20. Due to all these facts, the composition-temperature binary phase diagram of the $ZrSi_x$ alloy shows a pronounced dependence of the melting temperature T_m on the composition of approximately parabolic form with a single maximum close to the middle of the composition range. Hence the $ZrSi_x$ alloy is a good system for illustration of the composition dependence of the mechanical properties.

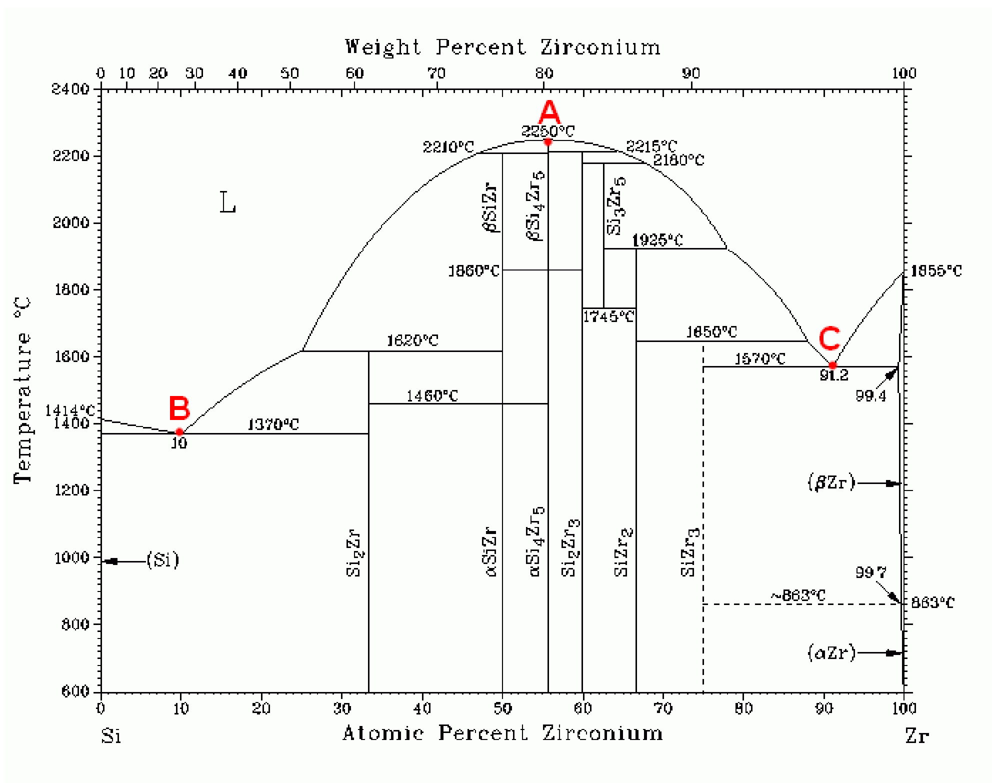

Figure 5-20: Binary phase diagram of the $SiZr_x$ with x = Zr/Si alloy or the $ZrSi_x$ with x = Si/Zr.

5.4.3 Effect of T_m on the coating properties and its experimental demonstration

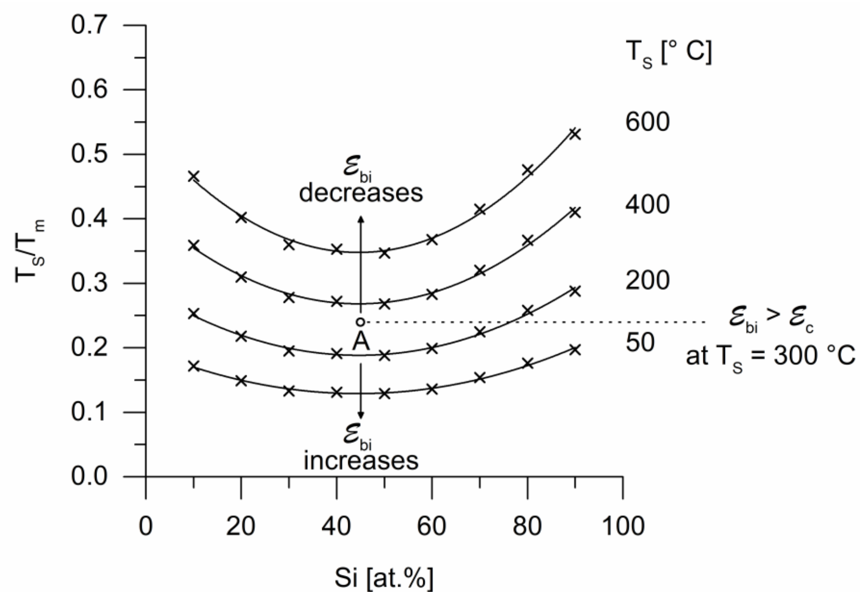

Figure 5-21: T_S/T_m of the ZrSi alloy as a function of the Si content at four values of the substrate temperature T_S = 50, 200, 400, and 600 °C at pressure p = const.

Figure 5-21 brings together the points from the discussion in the previous two sections and displays the evolution of the homologous temperature T_S/T_m as a function of the Si content in the $ZrSi_x$ alloy at four values of the substrate temperature T_S = 50, 200, 400 and 600 °C. Regions of the films with microstructure corresponding to zone T for pressure on the order 0.1 – 1 Pa typical for magnetron sputtering at low energies ε_{bi} (T_S/T_m = ~0.3 to ~0.4, see Figure 5-18) and at high ε_{bi} (T_S/T_m = ~0.2 to ~0.3) are marked too. This figure shows three important facts:

1. The function T_S/T_m = f (x) of the $ZrSi_x$ alloy is a parabolic curve with a minimum value $(T_S/T_m)_{min}$ at x = 0.8 corresponding to 44.4 at.% Si (point A in Figure 5-20) which corresponds to the highest value of the melting temperature T_m of the $ZrSi_x$ alloy.
2. The film produced at 44.4 at.% Si above the parabolic curve at $\varepsilon_{bi} > \varepsilon_c$ (point A) is hard, dense, voids-free and exhibits the microstructure corresponding to the zone T of the SZD. Point A decreases with increasing ε_{bi} and increases with decreasing ε_{bi}. All films sputtered in close vicinity above the parabolic curve exhibit either a microstructure corresponding to the zone T if they

are produced from solid material or a ductile microstructure if they are produced from a melted material when T_s/T_m is too high.

3. The films produced at T_S/T_m below parabolic curve from a non-melted material exhibit columnar microstructure corresponding to the SZD.

These facts indicate that the delivery of a correct amount of energy by $\mathcal{E}_{bi}$ and T_S is of key importance in the creation of alloy films with the highest hardness. Sputtering of Zr-Si alloy films as a function of at.% Si fully confirms these predictions.

5.4.4 Effect of homologous temperature T_S/T_m of sputtered Zr-Si alloy coatings

In the present section, the general principles described in the previous Sections 5.4.1 – 5.4.3 are applied to the specific examples. The $ZrSi_x$ alloy films were sputtered by a dual magnetron – see Chapter 5.1. The $ZrSi_x$ alloy film with 44.4 at.% Si sputtered at the substrate bias voltage U_S = -200 V, substrate ion current density i_s = 2.68 mA/cm^2 and T_S = 300 °C, i.e. at $(T_S/T_m)_{min}$ as can be seen in Figure 5-21, exhibits the highest hardness H = 21 GPa, see Figure 5-6 on page 52. It means that the highest hardness of the $ZrSi_x$ film exactly corresponds to the minimum homologous temperature $(T_S/T_m)_{min}$ in zone T of the SZD. Moreover, the hardness H increases with increasing negative substrate bias U_S, i.e. with increasing $\mathcal{E}_{bi}$. It indicates that the achievement of the highest hardness requires to decrease $(T_S/T_m)_{min}$ as much as possible, see the shift from point A to lower values of T_S/T_m, see Figure 5-21. The $ZrSi_x$ films with the highest hardness H = 21 GPa are super-elastic with elastic recovery $W_e \geq 60\%$ and exhibit a high ratio $H/E^* \geq 0.1$. These are key parameters for films resistant to cracking as was introduced in Section 2.3.2. However, the resistance to cracking is also strongly dependent on the film microstructure. Therefore, cross-section microstructure was investigated and indentation tests with diamond indenter at high load were performed, see Figure 5-2 on page 48 and Figure 5-3 on page 49. It was found that while the soft $ZrSi_x$ alloy film with X-ray amorphous structure and non-columnar microstructure cracks, the hard $ZrSi_x$ alloy film with polycrystalline structure and dense, voids-free non-columnar microstructure does not crack under the same diamond indenter load. This way it was demonstrated, for the first time, that it is possible to produce alloy films resistant to cracking even at room temperature (RT). More details on the sputtering of the Zr-Si

alloy films and their properties, namely their hardness and microstructure are given in Chapter 5.1.

In summary, it can be concluded that:

1. the highest hardness H of sputtered $ZrSi_x$ alloy films is achieved at the lowest ratio T_S/T_m which increases with the energy $\mathcal{E}_{bi}$,
2. the sputtered $ZrSi_x$ films with the highest H = 21 GPa with a high ratio $H/E^* \geq 0.1$ are super-elastic and resistant to cracking. This finding is of key importance because it clearly demonstrates that it is possible to produce alloy films resistant to cracking even at RT, and
3. the quantity $(T_S/T_m)_{min}$ is a good parameter that makes it possible to find easily the correct elemental composition of alloy film with the highest hardness.

5.4.5 Effect of the elemental composition of sputtered Mg-Si-N alloy coatings

As was stated in Section 2.3.4, the main drawback of all soft alloy films is their brittleness and easy cracking. It is caused by low values of their hardness H, ratio $H/E^* < 0.1$ and elastic recovery $W_e \leq 60\%$, mainly caused by a low value of T_m of the coating material. Therefore, finding conditions under which it is possible to achieve a high hardness H which will result in high values of high ratio $H/E^* \geq 0.1$ and elastic recovery $W_e \geq 60\%$ at a low value of T_m of the coating material is very important.

Recently, it was demonstrated that the increase of H can be achieved by the addition of Si into a single element film transition metal (TMe), for instance, Zr-Si alloy – see the previous Section 5.4.4 and Chapter 5.1. Therefore, the effect of the elemental composition on the coating hardness on mechanical properties of sputtered Si-based hard alloy coatings was investigated. The addition of Si into soft Mg single element was investigated in detail – see Chapter 5.2. As was shown, the Mg-Si(-N) and Si-N coatings were sputtered by a pulsed dual magnetron (PDM) with a closed magnetic field operated with asynchronous pulses. The coatings were sputtered on Si(100) substrates at six values of the substrate temperature (T_S = RT, 100, 200, 300, 400, and 500 °C), the substrate-to-target distance d_{s-t} =120 mm held either at the floating potential $U_S = U_{fl} \approx 3$ V or at the pulsed bias with alternating negative and positive pulses

U_S^- =-50 V/ U_S^+ = 50 V with the repetition frequency f_r = 5 kHz and ratio τ^-/τ^+ = 25/ 75 using pulsed DC power supply IAP 1010 (EN Technologies); here τ^- and τ^+ is the length of the negative and positive pulse, respectively. The effect of the addition of Si into the Mg film sputtered at a floating substrate bias $U_S = U_{fl}$ of Mg-Si alloy film on its mechanical properties is shown in Table 5-6. The effect of the addition of N into the Mg–Si alloy films sputtered at (i) a floating substrate bias $U_S = U_{fl}$ and T_S = 200 °C on its mechanical properties and the homologous temperature T_S/T_m, and (ii) the pulsed substrate bias U_S^-/ U_S^+ and six values of T_S = RT, 100, 200, 300, 400, and 500 °C on homologous temperature T_S/T_m and the energy $\mathcal{E}_{bi}$ is shown in Table 5-7. More details are given in Chapter 5.2 and Chapter 5.3.

Table 5-6: Mechanical and physical properties of sputtered Mg-Si alloy films sputtered by PDM at $U_S = U_{fl} \approx 3$ V and T_S = 200 °C.

film	p_{Ar} [Pa]	H [GPa]	E^* [GPa]	W_e [%]	H/E^*	σ [GPa]	T_S/ T_m
Mg	0.5	1.0	108	6	0.01	0.15	0.513
90Mg-10Si	0.5	1.3	86	13	0.02	0.33	0.410
80Mg-20Si	0.5	1.8	92	15	0.02	0.31	0.369
35Mg-65Si	0.5	6	101	38	0.06	-0.11	0.342
15Mg-85Si	1	7	109	51	0.06	-0.06	0.299
Si	0.5	11	125	54	0.09	-0.03	0.281

Table 5-7: Mechanical and physical properties of sputtered (Mg-)Si-N alloy films sputtered by PDM at (i) $U_S = U_{fl} \approx 3$ V and $T_S = 200$ ℃ and (ii)) the pulsed substrate bias U_S^-/U_S^+, $p_T = p_{Ar} + p_{N2} = p_{N2} = 0.3$ Pa and six values of T_S = RT, 100, 200, 300, 400, and 500℃ on homologous temperature T_S/T_m and the energy $\mathcal{E}_{bi}$.

film	p_{Ar} [Pa]	p_{N2} [Pa]	T_S [°C]	H [GPa]	E^* [GPa]	W_e [%]	H/E^*	σ [GPa]	T_S/T_m	$\mathcal{E}_{bi}$ [MJ/cm^3]
$U_S = U_{fl} \approx 3$ V										
20Mg-20Si-60N	0	0.3	200	21	167	74	0.13	-0.28	0.218 [3]	-
12Mg-24Si-64N	0	0.3	200	23	176	77	0.13	-0.62	0.218 [3]	-
33Si-67N = SiN	0	0.3	200	26	197	78	0.13	-1.0	0.218 [3]	-
Pure SiN films, pulsed substrate bias at f_{rs} = 5 kHz										
SiN	0	0.3	RT	27	183	82	0.15	-2.22	0.136	1.365
SiN	0	0.3	100	27	193	80	0.14	-1.25	0.171	1.254
SiN	0	0.3	200	26	192	79	0.14	-1.64	0.218	1.189
SiN	0	0.3	300	28	202	82	0.14	-1.74	0.264	1.374
SiN	0	0.3	400	30	194	87	0.15	-2.22	0.310	1.562
SiN	0	0.3	500	32	193	90	0.16	-2.62	0.356	1.418

[3] For all Mg-Si-N alloy nitride films the melting temperature $T_{m(Si3N4)}$ = 2173 K was used in the calculation of the homologous temperature T_S/T_m.

The main results of sputtered Mg-Si alloy Mg-Si-N alloy nitride and SiN nitride coating are the following:

1. The addition of Si into a single element Mg alloy increases its hardness from 1 GPa up to 11 GPa when Mg is completely substituted by Si. The hardness of pure Mg and pure Si coating is H_{Mg} = 1 GPa and H_{Si} = 11 GPa.
2. The increase of the hardness of Mg-Si to ~10 GPa is, however, insufficient to achieve high values of the ratio $H/E^* \geq 0.1$, the elastic recovery $W_e \geq 60\%$, compressive macrostress ($\sigma < 0$), and dense, voids-free microstructure necessary to prevent cracking of the Mg-Si coating. Therefore, it is necessary to add a third element into the coating.
3. The addition of N into the Mg–Si alloy film strongly increases the hardness H of Mg-Si-N alloy nitride coatings up to high values ranging from ~20 to ~26 GPa. These high values of H fully confirm conditions specified in point 2 and prevent cracking of these Mg-Si-N coatings to cracking even at RT.
4. The hardness H of the Mg-Si-N films increases with decreasing homologous temperature T_S/T_m and is maximum when the ratio T_S/T_m is minimum. This fact is of key importance for a selection of the elemental composition of a protective alloy film which is desired to be hard, super-elastic and resistant to cracking.
5. The pure SiN films are hard, super-elastic and resistant to cracking because they exhibit a high ratio $H/E^* > 0.1$. The hardness of these films increases with increasing (i) homologous temperature (T_S/T_m), (ii) substrate temperature T_S and increasing compressive macrostress ($\sigma < 0$) and decreasing energy $\mathcal{E}_{bi}$ delivered into a growing film by bombarding ions.

In summary, it can be concluded that:

To increase the hardness of the soft single element film with a low melting point requires incorporating into it not only Si but also another third element. The current investigation showed that Si and N are typical elements that strongly increase H of the soft element film such as Mg, Al, Ga, Sn, In, etc.

The Mg-Si alloy is a two-phase material composed of h-Mg and fcc-Mg_2Si phases. The hexagonal h-Mg phase is a crystalline material and fcc-Mg_2Si phase is an amorphous material. These two phases are immiscible. It means that the Mg-Si alloy film is crystalline at high content of Mg and, on other hand, amorphous at high Si content. The film amorphization increases with increasing Si content. This fact was experimentally confirmed, see Figure 5-10 on page 61. This amorphization process strongly influences the film microstructure. It is the main reason why the film microstructure also plays a key role in the formation of new advanced flexible hard protective coatings resistant to cracking, see next section 5.4.6.

5.4.6 The microstructure of sputtered Mg coating from a melted coating material

This section briefly describes the effect of the homologous temperature T_S/T_m and the energy $\mathcal{E}_{bi}$ on the microstructure of sputtered hard protective films. The homologous temperature T_S/T_m can be varied either by the substrate temperature T_S at a constant value of the melting temperature T_m of the coating material or by a constant value of the substrate temperature T_S at different values of T_m, i.e. at a different elemental composition of sputtered films.

The effect of T_S/T_m on the microstructure of sputtered coatings is illustrated on sputtered Mg-Si-N films prepared by a pulsed dual magnetron (PDM) with a closed magnetic field operated with asynchronous pulses. The coatings were sputtered on Si(100) substrates and their mechanical properties are summarized in Table 5-6 in Section 5.4.5 above. The microstructure strongly differs at a low and high (T_S/T_m), see Figure 5-22. In this figure cross-section microstructure of (a) single element soft Mg film sputtered at T_S/T_m = 0.513 and (b) hard 12Mg-24Si-64N nitride alloy film, both sputtered at T_s = 200 °C are compared.

The microstructure of the soft Mg film and the hard 12Mg-24Si-64N film strongly differs because they were sputtered under very different homologous temperatures T_S/T_m = 0.513 and 0.218, respectively. The soft Mg film produced at a high T_S/T_m = 0.513 is ductile and exhibits a microstructure with many large voids typical for the film formed from the melted state. On the other hand, hard, super-elastic 12Mg-24Si-64N nitride alloy film exhibits dense, voids-free non-columnar microstructure typical for hard films with high ratio $H/E^* > 0.1$.

However, the increase of the homologous temperature T_S/T_m by raising the substrate temperature T_S is less effective compared with the increase of T_S/T_m by reducing the melting temperature T_m (soft elements) at T_S = const, see Figure 5-23. In this figure, the microstructure of SiN nitride film sputtered at T_S = 500 °C is displayed. This hard film sputtered at a high T_S = 500 °C (T_s/T_m = 0.356) is formed from non-melted material and exhibits a dense, voids-free microstructure. It means that it is very difficult to create ductile soft films from a melted film material by increasing T_S up to 500 °C.

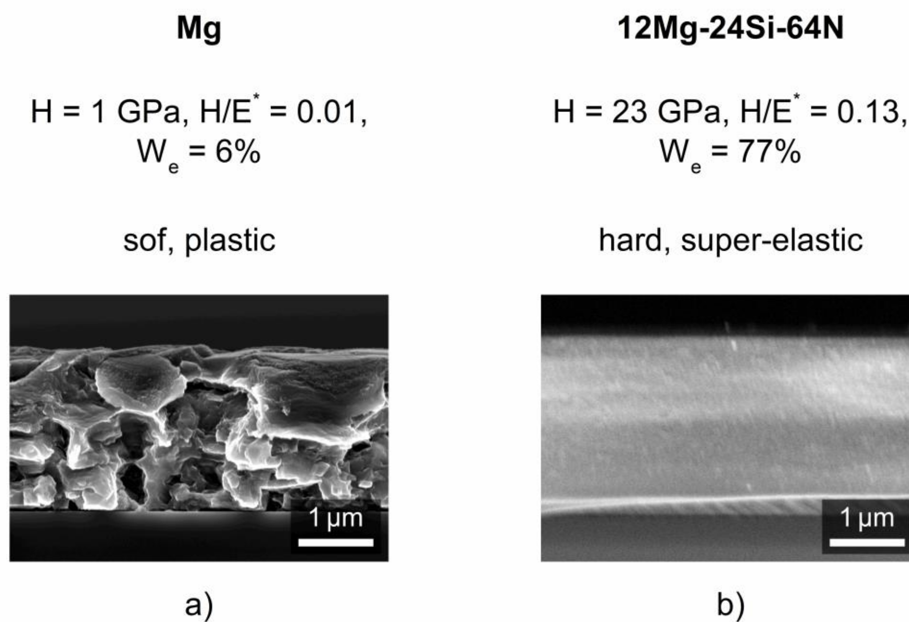

Figure 5-22: Comparison of the cross-section microstructure of the single element Mg film sputtered at T_S/T_m = 0.513 and the 12Mg-24Si-64N alloy nitride film sputtered at T_S/T_m = 0.218 and both deposited on Si(100) substrate.

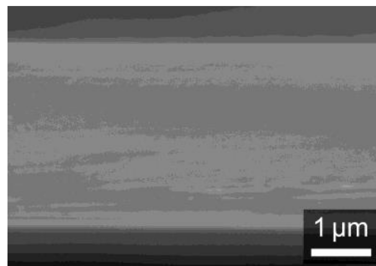

Figure 5-23: Cross-section microstructure of hard, super-elastic stoichiometric $SiN_{x\approx 1}$ nitride film at a high T_S = 500 °C.

5.4.7 Conclusions

In this chapter, two fundamental facts are demonstrated:

1. the hardness H of the hard alloy coatings strongly depend on the homologous temperature T_S/T_m of their coating material and the energy $\mathcal{E}_{bi}$ delivered into them during their growth, and
2. hard alloy coatings are resistant to cracking if they exhibit a high hardness H resulting in high values of (i) the ratio $H/E^* \geq 0.1$ and the elastic recovery $W_e \geq 60\%$, i.e. they are super-elastic.

The main obtained results can be briefly summarized as follows:

1. The hard, protective alloy coatings resistant to cracking must fulfil three conditions: (1) High hardness H resulting in (i) a high ratio $H/E^* \geq 0.1$ and (ii) an elastic recovery $W_e \geq 60\%$, (2) dense, voids-free microstructure, and (3) a small compressive macrostress ($\sigma < |2\ \mathrm{GPa}|$); these are the same conditions which hard protective coatings resistant to cracking based on nitrides, oxides, borides, carbides etc. and their combination must fulfil. The achievement of sufficiently high hardness in alloy coatings resistant to cracking is, however, a very serious problem because alloy coatings are generally soft. Despite this fact, the hard alloy coatings resistant to cracking can be produced by correct selection of (i) the elemental composition of the alloy and (ii) deposition conditions based on the homologous temperature T_S/T_m and energy of ion bombardment $\mathcal{E}_{bi}$, see next points.
2. The microstructure of sputtered films is strongly influenced by the melting temperature T_m via the homologous temperature T_S/T_m, and T_m is in turn strongly influenced by the elemental composition of the hard coatings. That way, the elemental composition strongly influences the coating's microstructure and consequently its mechanical properties via T_m.
3. To reach the desired zone T of the SZD, the energy delivered into growing films by bombarding ions $\mathcal{E}_{bi}$ and condensing fast neutral atoms $\mathcal{E}_{fn}$ related to the sputtering gas pressure p needs to be properly adjusted. The appropriate values of the ratio T_S/T_m decrease with increasing $\mathcal{E}$ and decreasing p. It was demonstrated for hard, super-elastic $ZrSi_x$ alloy coating resistant to cracking,

see also Chapter 5.1. The highest hardness H of sputtered $ZrSi_x$ alloy films is achieved at the lowest ratio T_S/T_m and increased ion bombardment $\mathcal{E}_{bi}$.

4. In the case of a soft element with low T_m such as Mg ($T_{m(Mg)}$ = 922 K), two elements Si and N have to be added to achieve sufficient H resulting in a high ratio $H/E^* > 0.1$. It was demonstrated for hard super-elastic Mg-Si-N nitride alloy coatings, see also Chapter 5.2, and Si-N nitride coatings, see Chapter 5.3.
5. The Si and N are typical elements that strongly increase the hardness of sputtered coatings. This fact was experimentally demonstrated in sputtering of the $ZrSi_x$ alloy, Mg-Si-N alloy nitride and SiN_x nitride protective coatings.
6. The quantity $(T_S/T_m)_{min}$ is a good parameter which makes it possible to find easily the correct elemental composition of alloy film with the highest hardness resulting in a high ratio $H/E^* \geq 0.1$.

In summary, it can be concluded that the production of hard, super-elastic protective alloy coatings resistant to cracking even at room temperature was successfully mastered and conditions under which they can be created were found. These conditions are of general validity and make it possible to produce hard, super-elastic protective alloy coatings made of both hard elements with a high T_m and soft elements with low T_m.

6 CONCLUSIONS

The main aim of the Ph.D. thesis was the detailed investigation of the physical and mechanical properties of alloy films prepared by magnetron sputtering to find the deposition conditions enabling the formation of hard protective coatings with enhanced resistance to cracking. It was demonstrated both theoretically and experimentally that four necessary requirements have to be met when hard, super-elastic alloy films are desired to be sputtered:

- $H/E^* > 0.1$, here H is the hardness, E^* is the effective Young‘s modulus,
- $W_e \geq 60\%$, W_e is the elastic recovery,
- low compressive macrostress ($\sigma \leq |2\ GPa|$),
- and dense, voids-free microstructure corresponding to zone T at Thornton‘s structural zone.

Detailed investigation of three groups of films has been done as summarized below. Moreover, a comprehensive study of the role of the homologous temperature (T_S/T_m, here T_S is the substrate temperature and T_m is the melting point) on the mechanical properties of alloy films was presented.

1. The first aim was to investigate the properties of Zr-Si alloy films and show if there are deposition conditions under which it is possible to sputter hard films with enhanced resistance to cracking. In Chapter 5.1, it was shown that the $ZrSi_x$ alloy films with $x = Si/Zr \approx 1$ composed of one metalloid and one metallic element (Met, Me) are hard and resistant to cracking and exhibit considerably higher values of the hardness H, H/E^* ratio and elastic recovery W_e compared with soft and brittle (Me_1, Me_2) alloy films composed of two metallic elements, for instance, the (Zr, Ti) films. The flexible hard $ZrSi_x$ alloy films with $x \approx 1$ exhibit high values of $H \geq 18$ GPa, $H/E^* \geq 0.1$, $W_e \geq 60\%$, non-columnar dense, voids-free microstructure and compressive macrostress ($\sigma < 0$). The high hardness and enhanced resistance to cracking of films result from a combined action of their elemental composition and compressive stress. The reported results suggest that the replacement of one metal element in the soft brittle (Me_1, Me_2) alloy film by a metalloid element can remove its brittleness and strongly increase its hardness and resistance to cracking.

2. The second aim was to study Mg-Si alloy films and then the influence of nitrogen addition on the properties of the films. In Chapter 5.2, it was shown that Mg-Si alloy films are soft with maximum hardness H < 10 GPa, exhibit low values of the ratio $H/E^* < 0.1$, $W_e < 60\%$, tensile macrostress and columnar microstructure and easily crack. When N was incorporated into the films, the hardness and resistance to cracking were strongly increased. The main conclusion of this experiment is that the hardness H of the alloy film strongly depends on the homologous temperature T_S/T_m of its material in a way that the highest hardness of the single element or a soft alloy film is achieved if T_S/T_m is minimum. It was experimentally demonstrated that the addition of Si and N into the Mg single element film is a very effective way to sputter hard alloy films with H up to ~ 27 GPa resistant to cracking.
3. The third aim was the investigation of Si-N films in order to further increase the hardness of the Mg-Si-N films. In Chapter 5.3, it was shown that at precisely controlled deposition conditions it is possible to reactively sputter Si-N films which are hard with H up to 32 GPa, superelastic, and exhibit enhanced resistance to cracking. As was described in Chapter 5.2, low values of T_S/T_m, important for sputtering films with a maximum hardness, can be achieved either by a high T_m of film material or by a decrease of $T_{S.}$; however, on the Si-N films, it was shown that the use of a high T_S is not optimal for the production of hard alloy films because a crystalline material is formed by slow cooling from the melted film material at high T_S.
4. The fourth aim was to characterize the role of the homologous temperature T_S/T_m. The key importance of this parameter on the hardness of alloy films was demonstrated in Chapter 5.4 using the previous studies on Zr-Si and Mg-Si(-N) films. It was shown that the microstructure of sputtered films is strongly influenced by the melting temperature T_m via the homologous temperature T_S/T_m, and T_m is in turn strongly influenced by the elemental composition of the hard coatings. On the Zr-Si films, it was demonstrated that the appropriate values of the ratio T_S/T_m decrease with increasing energy $\mathcal{E}$ delivered to the growing film and decreasing pressure p. The highest hardness H of sputtered $ZrSi_x$ alloy films is achieved at the lowest ratio T_S/T_m and increased ion bombardment $\mathcal{E}_{bi}$. In the case of a soft element with low T_m

such as Mg ($T_{m(Mg)}$ = 922 K), two elements Si and N have to be added to achieve sufficient H resulting in a high ratio $H/E^* > 0.1$. Using both studies it was shown that the quantity $(T_S/T_m)_{min}$ is a good parameter which makes it possible to find easily the correct elemental composition of alloy film with the highest hardness resulting in a high ratio $H/E^* \geq 0.1$.

REFERENCES

[1] J. S. Chapin, “Sputtering process and apparatus,” 05/438,482, Jan. 31, 1974.

[2] I. Safi, “Recent aspects concerning DC reactive magnetron sputtering of thin films: A review,” *Surf. Coatings Technol.*, vol. 127, no. 2–3, pp. 203–218, May 2000, doi: 10.1016/s0257-8972(00)00566-1.

[3] J. Musil, P. Baroch, J. Vlček, K. H. Nam, and J. G. Han, “Reactive magnetron sputtering of thin films: Present status and trends,” *Thin Solid Films*, vol. 475, no. 1-2 SPEC. ISS., pp. 208–218, Mar. 2005, doi: 10.1016/j.tsf.2004.07.041.

[4] J. Musil, J. Vlček, and P. Baroch, “Magnetron Discharges for Thin Films Plasma Processing,” *Eur. Mater. Res. Soc. Ser.*, pp. 67–110, 2006, doi: 10.1016/B978-008044496-3/50004-6.

[5] P. J. Kelly, G. West, Y. N. Kok, J. W. Bradley, I. Swindells, and G. C. B. Clarke, “A comparison of the characteristics of planar and cylindrical magnetrons operating in pulsed DC and AC modes,” *Surf. Coatings Technol.*, vol. 202, no. 4–7, pp. 952–956, Dec. 2007, doi: 10.1016/j.surfcoat.2007.04.130.

[6] J. Lin *et al.*, “Recent advances in modulated pulsed power magnetron sputtering for surface engineering,” *JOM*, vol. 63, no. 6, pp. 48–58, Jun. 2011, doi: 10.1007/s11837-011-0092-4.

[7] J. T. Gudmundsson, N. Brenning, D. Lundin, and U. Helmersson, “High power impulse magnetron sputtering discharge,” *J. Vac. Sci. Technol. A Vacuum, Surfaces, Film.*, vol. 30, no. 3, p. 030801, May 2012, doi: 10.1116/1.3691832.

[8] K. Hori, T. Namazu, and S. Inoue, “Effect of Cu content on the shape memory behavior of Ti-Ni-Cu alloy thin films prepared by triple-source dc magnetron sputtering,” in *Thin Solid Films*, 2010, vol. 518, no. 21 SUPPL., doi: 10.1016/j.tsf.2010.03.027.

[9] J. F. Chang, H. Y. Ueng, T. F. Young, Y. C. Wang, and W. C. Hwang, “Combined magnetron sputtering and ECR-CVD deposition of diamond-like carbon films,” *Surf. Coatings Technol.*, vol. 157, no. 2–3, pp. 179–184, Aug. 2002, doi: 10.1016/S0257-8972(02)00157-3.

[10] K. Yamamoto, S. Kujime, and K. Takahara, “Properties of nano-multilayered hard coatings deposited by a new hybrid coating process: Combined cathodic arc and unbalanced magnetron sputtering,” *Surf. Coatings Technol.*, vol. 200, no. 1-4 SPEC. ISS., pp. 435–439, Oct. 2005, doi: 10.1016/j.surfcoat.2005.02.175.

[11] J. G. Jones, C. Muratore, A. R. Waite, and A. A. Voevodin, "Plasma diagnostics of hybrid magnetron sputtering and pulsed laser deposition," *Surf. Coatings Technol.*, vol. 201, no. 7 SPEC. ISS., pp. 4040–4045, Dec. 2006, doi: 10.1016/j.surfcoat.2006.08.096.

[12] D. B. Mohan and A. Cavaleiro, "Experimental development and deposition of nanocomposite films by a hybrid dc magnetron sputtering and cluster gun technique," *Vacuum*, vol. 83, no. 10, pp. 1257–1261, Jun. 2009, doi: 10.1016/j.vacuum.2009.03.016.

[13] J. Musil, "Hard and superhard nanocomposite coatings," in *Surface and Coatings Technology*, Mar. 2000, vol. 125, no. 1–3, pp. 322–330, doi: 10.1016/S0257-8972(99)00586-1.

[14] J. Musil *et al.*, "Flexible hard nanocomposite coatings," *RSC Adv.*, vol. 5, no. 74, pp. 60482–60495, 2015, doi: 10.1039/C5RA09586G.

[15] S. Zhao, E. Avendaño, K. Gelin, J. Lu, and E. Wäckelgård, "Optimization of an industrial DC magnetron sputtering process for graded composition solar thermal absorbing layer," *Sol. Energy Mater. Sol. Cells*, vol. 90, no. 3, pp. 308–328, Feb. 2006, doi: 10.1016/j.solmat.2005.03.018.

[16] Y. Song and T. Sakurai, "High-rate, low-temperature radical-assisted sputtering coater and its applications for depositing high-performance optical filters," *Vacuum*, vol. 74, no. 3-4 SPEC. ISS., pp. 409–415, Jun. 2004, doi: 10.1016/j.vacuum.2004.01.008.

[17] S. Niyomsoan, W. Grant, D. L. Olson, and B. Mishra, "Variation of color in titanium and zirconium nitride decorative thin films," *Thin Solid Films*, vol. 415, no. 1–2, pp. 187–194, Aug. 2002, doi: 10.1016/S0040-6090(02)00530-8.

[18] S. P. Murarka, "Silicide thin films and their applications in microelectronics," *Intermetallics*, vol. 3, no. 3, pp. 173–186, 1995, doi: 10.1016/0966-9795(95)98929-3.

[19] M. B. Takeyama, A. Noya, and K. Sakanishi, "Diffusion barrier properties of ZrN films in the Cu/Si contact systems," *J. Vac. Sci. Technol. B Microelectron. Nanom. Struct.*, vol. 18, no. 3, p. 1333, 2000, doi: 10.1116/1.591382.

[20] J. Pelleg, "Schottky barrier formation at Cu/TiB[sub 2]/TiSi[sub 2]/Si interface," *J. Vac. Sci. Technol. B Microelectron. Nanom. Struct.*, vol. 18, no. 3, p. 1338, 2000, doi: 10.1116/1.591383.

[21] P. J. Kelly and R. D. Arnell, "Magnetron sputtering: A review of recent

developments and applications," *Vacuum*, vol. 56, no. 3, pp. 159–172, Mar. 2000, doi: 10.1016/S0042-207X(99)00189-X.

[22] P. Baroch and J. Musil, "Plasma drift in dual magnetron discharge," *IEEE Trans. Plasma Sci.*, vol. 36, no. 4 PART 1, pp. 1412–1413, Aug. 2008, doi: 10.1109/TPS.2008.924483.

[23] J. Musil and P. Baroch, "Discharge in dual magnetron sputtering system," *IEEE Trans. Plasma Sci.*, vol. 33, no. 2 I, pp. 338–339, Apr. 2005, doi: 10.1109/TPS.2005.844996.

[24] H. Holleck, "Material selection for hard coatings," *J. Vac. Sci. Technol. A Vacuum, Surfaces, Film.*, vol. 4, no. 6, pp. 2661–2669, Nov. 1986, doi: 10.1116/1.573700.

[25] H. Adachi and K. Wasa, "Thin Films and Nanomaterials," *Handb. Sputter Depos. Technol. Fundam. Appl. Funct. Thin Film. Nano-Materials MEMS Second Ed.*, pp. 3–39, Nov. 2012, doi: 10.1016/B978-1-4377-3483-6.00001-2.

[26] L. Morresi, "Basics of molecular beam epitaxy (MBE)," *Silicon Based Thin Film Sol. Cells*, no. January 2013, pp. 81–107, 2013, doi: 10.1093/jac/dku047.

[27] J. A. Thornton, "Structure-Zone Models Of Thin Films," *Model. Opt. Thin Film.*, vol. 0821, p. 95, Feb. 1988, doi: 10.1117/12.941846.

[28] B. A. Movchan and A. V. Demchishin, "Study of the structure and properties of thick vacuum condesates of nickel, titanium, tungsten, aluminum oxide and zirconium oxide," *Phys. Met. Mellogr.*, vol. 28, pp. 83–90, 1969.

[29] J. A. Thornton, "High rate thick film growth," *Annu. Rev. Mater. Sci.*, vol. 7, pp. 239–260, Nov. 1977, doi: 10.1146/annurev.ms.07.080177.001323.

[30] J. A. Thornton and D. W. Hoffman, "Stress-related effects in thin films," *Thin Solid Films*, vol. 171, no. 1, pp. 5–31, Apr. 1989, doi: 10.1016/0040-6090(89)90030-8.

[31] J. Musil and J. Šůna, "The Role of Energy in Formation of Sputtered Nanocomposite Films," *Mater. Sci. Forum*, vol. 502, pp. 291–296, Dec. 2005, doi: 10.4028/www.scientific.net/msf.502.291.

[32] J. Soldán and J. Musil, "Structure and mechanical properties of DC magnetron sputtered TiC/Cu films," *Vacuum*, vol. 81, no. 4, pp. 531–538, Nov. 2006, doi: 10.1016/j.vacuum.2006.07.013.

[33] J. Musil, M. Jaroš, R. Čerstvý, and S. Haviar, "Evolution of microstructure and macrostress in sputtered hard Ti(Al,V)N films with increasing energy delivered during their growth by bombarding ions," *J. Vac. Sci. Technol. A Vacuum,*

Surfaces, Film., vol. 35, no. 2, p. 020601, 2017, doi: 10.1116/1.4967935.

[34] A. Anders, "A structure zone diagram including plasma-based deposition and ion etching," *Thin Solid Films*, vol. 518, no. 15, pp. 4087–4090, May 2010, doi: 10.1016/j.tsf.2009.10.145.

[35] T. B. Massalski, "Phase Diagrams," in *Encyclopedia of Materials: Science and Technology*, Elsevier, 2001, pp. 6842–6851.

[36] D. A. Porter and K. E. Easterling, *Phase Transformations in Metals and Alloys*. 1992.

[37] L. D. Landau, E. M. Lifshitz, L. P. Pitaevskii, J. B. Sykes, and M. J. Kearsley, "Statistical Physics," *Course Theor. Physics, §97, Pergamon Press*, vol. 5, p. 544, 1980.

[38] A. Prince and H. M. Otte, "Alloy Phase Equilibria," *Phys. Today*, vol. 19, no. 12, pp. 88–89, Dec. 1966, doi: 10.1063/1.3047876.

[39] P. Gordon, *Principles of Phase Diagrams in Materials Systems*. McGraw-Hill Book Company, 1968.

[40] H. Gleiter, "Nanocrystalline Materials," in *Advanced Structural and Functional Materials*, Berlin, Heidelberg: Springer Berlin Heidelberg, 1991, pp. 1–37.

[41] R. W. Siegel and G. E. Fougere, "Grain size dependent mechanical properties in nanophase materials," in *Materials Research Society Symposium - Proceedings*, 1995, vol. 362, pp. 219–229, doi: 10.1557/proc-362-219.

[42] J. Musil, "Physical and Mechanical Properties of Hard Nanocomposite Films Prepared by Reactive Magnetron Sputtering," *Nanostructured Coatings*, pp. 407–463, 2006, doi: 10.1007/978-0-387-48756-4_10.

[43] P. H. Mayrhofer, C. Mitterer, L. Hultman, and H. Clemens, "Microstructural design of hard coatings," *Progress in Materials Science*, vol. 51, no. 8. Pergamon, pp. 1032–1114, Nov. 01, 2006, doi: 10.1016/j.pmatsci.2006.02.002.

[44] J. Musil and M. Jirout, "Toughness of hard nanostructured ceramic thin films," *Surf. Coatings Technol.*, vol. 201, no. 9-11 SPEC. ISS., pp. 5148–5152, Feb. 2007, doi: 10.1016/j.surfcoat.2006.07.020.

[45] J. Musil, "Hard nanocomposite coatings: Thermal stability, oxidation resistance and toughness," *Surf. Coatings Technol.*, vol. 207, pp. 50–65, Aug. 2012, doi: 10.1016/j.surfcoat.2012.05.073.

[46] J. Musil, "Flexible hard nanocomposite coatings," *RSC Advances*, vol. 5, no. 74. Royal Society of Chemistry, pp. 60482–60495, Jul. 10, 2015, doi:

10.1039/c5ra09586g.

[47] J. Musil, Š. Kos, S. Zenkin, Z. Čiperová, D. Javdošňák, and R. Čerstvý, "β- (Me 1 , Me 2) and MeNx films deposited by magnetron sputtering: Novel heterostructural alloy and compound films," *Surf. Coatings Technol.*, vol. 337, pp. 75–81, Mar. 2018, doi: 10.1016/j.surfcoat.2017.12.057.

[48] S. Vepřek and S. Reiprich, "A concept for the design of novel superhard coatings," *Thin Solid Films*, vol. 268, no. 1–2, pp. 64–71, Nov. 1995, doi: 10.1016/0040-6090(95)06695-0.

[49] J. Musil, "Hard and superhard nanocomposite coatings," in *Surface and Coatings Technology*, Mar. 2000, vol. 125, no. 1–3, pp. 322–330, doi: 10.1016/S0257-8972(99)00586-1.

[50] A. Leyland and A. Matthews, "On the significance of the H/E ratio in wear control: A nanocomposite coating approach to optimised tribological behaviour," *Wear*, vol. 246, no. 1–2, pp. 1–11, Nov. 2000, doi: 10.1016/S0043-1648(00)00488-9.

[51] R. Hauert and J. Patscheider, "From alloying to nanocomposites - Improved performance of hard coatings," *Advanced Engineering Materials*, vol. 2, no. 5. Wiley-VCH Verlag, pp. 247–259, May 01, 2000, doi: 10.1002/(SICI)1527-2648(200005)2:5<247::AID-ADEM247>3.0.CO;2-U.

[52] C. Mitterer, P. H. Mayrhofer, and J. Musil, "Thermal stability of PVD hard coatings," in *Vacuum*, May 2003, vol. 71, no. 1-2 SPEC., pp. 279–284, doi: 10.1016/S0042-207X(02)00751-0.

[53] J. Patscheider, "Nanocomposite hard coatings for wear protection," *MRS Bull.*, vol. 28, no. 3, pp. 180–183, 2003, doi: 10.1557/mrs2003.59.

[54] S. Zhang, D. Sun, Y. Fu, and H. Du, "Recent advances of superhard nanocomposite coatings: A review," *Surf. Coatings Technol.*, vol. 167, no. 2–3, pp. 113–119, Apr. 2003, doi: 10.1016/S0257-8972(02)00903-9.

[55] S. Zhang, D. Sun, Y. Fu, and H. Du, "Toughening of hard nanostructural thin films: A critical review," *Surf. Coatings Technol.*, vol. 198, no. 1-3 SPEC. ISS., pp. 2–8, Aug. 2005, doi: 10.1016/j.surfcoat.2004.10.020.

[56] J. Musil, "Advanced Hard Nanocoatings: Present State and Trends," *Chapter Top 5 Contrib. Mol. Sci. 6th Ed.*, pp. 2–65, 2019, Accessed: Mar. 19, 2020. [Online]. Available: www.avidscience.com.

[57] J. Vlček *et al.*, "Reactive magnetron sputtering of hard Si–B–C–N films with a high-temperature oxidation resistance," *J. Vac. Sci. Technol. A Vacuum, Surfaces,*

Film., vol. 23, no. 6, pp. 1513–1522, Nov. 2005, doi: 10.1116/1.2049298.

[58] J. Musil, “Flexible hard nanocomposite coatings,” *RSC Advances*, vol. 5, no. 74. Royal Society of Chemistry, pp. 60482–60495, Jul. 10, 2015, doi: 10.1039/c5ra09586g.

[59] H. Poláková, J. Musil, J. Vlček, J. Allaart, and C. Mitterer, “Structure-hardness relations in sputtered Ti–Al–V–N films,” *Thin Solid Films*, vol. 444, no. 1, pp. 189–198, 2003, doi: 10.1016/S0040-6090(03)01096-4.

[60] J. Musil, H. Poláková, J. Šuna, and J. Vlček, “Effect of ion bombardment on properties of hard reactively sputtered Ti(Fe)Nx films,” *Surf. Coatings Technol.*, vol. 177–178, pp. 289–298, Jan. 2004, doi: 10.1016/j.surfcoat.2003.09.007.

[61] J. Musil, J. Šícha, D. Heřman, and R. Čerstvý, “Role of energy in low-temperature high-rate formation of hydrophilic TiO2 thin films using pulsed magnetron sputtering,” *J. Vac. Sci. Technol. A Vacuum, Surfaces, Film.*, vol. 25, no. 4, pp. 666–674, Jul. 2007, doi: 10.1116/1.2736680.

[62] M. Jaroš, J. Musil, R. Čerstvý, and S. Haviar, “Effect of energy on structure, microstructure and mechanical properties of hard Ti(Al,V)Nx films prepared by magnetron sputtering,” *Surf. Coatings Technol.*, vol. 332, pp. 190–197, Dec. 2017, doi: 10.1016/j.surfcoat.2017.06.074.

[63] M. Jaroš, J. Musil, R. Čerstvý, and S. Haviar, “Effect of energy on macrostress in Ti(Al,V)N films prepared by magnetron sputtering,” *Vacuum*, vol. 158, pp. 52–59, Dec. 2018, doi: 10.1016/j.vacuum.2018.09.038.

[64] J. Vlček, K. Rusňák, V. Hájek, and L. Martinů, “Reactive magnetron sputtering of CNx films: Ion bombardment effects and process characterization using optical emission spectroscopy,” *J. Appl. Phys.*, vol. 86, no. 7, pp. 3646–3654, Oct. 1999, doi: 10.1063/1.371273.

[65] M. A. Lieberman and A. J. Lichtenberg, “Principles of Plasma Discharges and Materials Processing,” *Princ. Plasma Discharges Mater. Process. Second Ed.*, pp. 1–757, Apr. 2005, doi: 10.1002/0471724254.

[66] P. D. Tall *et al.*, “Materials and Manufacturing Processes Nanoindentation of Ni–Ti Thin Films Nanoindentation of Ni–Ti Thin Films,” *Mater. Manuf. Process.*, vol. 22, pp. 175–179, 2007, doi: 10.1080/10426910601062222.

[67] W. F. Cui and C. J. Shao, “The improved corrosion resistance and anti-wear performance of Zr–xTi alloys by thermal oxidation treatment,” *Surf. Coatings Technol.*, vol. 283, pp. 101–107, 2015, doi: 10.1016/j.surfcoat.2015.10.051.

[68] D. Photiou, N. T. Panagiotopoulos, L. Koutsokeras, G. A. Evangelakis, and G. Constantinides, “Microstructure and nanomechanical properties of magnetron sputtered Ti − Nb films,” *Surf. Coatings Technol.*, vol. 302, pp. 310–319, Sep. 2016, doi: 10.1016/j.surfcoat.2016.06.014.

[69] J. Musil, S. Zenkin, R. Čerstvý, S. Haviar, and Z. Čiperová, “(Zr,Ti,O) alloy films with enhanced hardness and resistance to cracking prepared by magnetron sputtering,” *Surf. Coat. Technol.*, vol. 322, pp. 86–91, 2017, doi: 10.1016/j.surfcoat.2017.05.006.

[70] F. Zhang, C. Li, M. Yan, J. He, Y. Yang, and F. Yin, “Microstructure and nanomechanical properties of co-deposited Ti-Cr films prepared by magnetron sputtering,” *Surf. Coatings Technol.*, vol. 325, pp. 636–642, Sep. 2017, doi: 10.1016/J.SURFCOAT.2017.07.005.

[71] T. Oellers *et al.*, “Microstructure and mechanical properties in the thin film system Cu-Zr,” *Thin Solid Films*, vol. 645, pp. 193–202, Jan. 2018, doi: 10.1016/j.tsf.2017.10.030.

[72] I. Souli, V. L. Terziyska, J. Zechner, and C. Mitterer, “Microstructure and physical properties of sputter-deposited Cu-Mo thin films,” *Thin Solid Films*, vol. 653, pp. 301–308, May 2018, doi: 10.1016/J.TSF.2018.03.039.

[73] C. Wang, T. Wang, L. Cao, G. Wang, and G. Zhang, “Solid solution or amorphous phase formation in Al-Mo alloyed films and their mechanical properties,” *J. Alloys Compd.*, vol. 746, pp. 77–83, May 2018, doi: 10.1016/J.JALLCOM.2018.02.230.

[74] J. Li, J. Wang, A. Kumar, H. Li, and D. Xiong, “High temperatures tribological properties of Ta-Ag films deposited at various working pressures and sputtering powers,” *Surf. Coatings Technol.*, vol. 349, pp. 186–197, Sep. 2018, doi: 10.1016/j.surfcoat.2018.05.066.

[75] B. P. Sahu, C. K. Sarangi, and R. Mitra, “Effect of Zr content on structure property relations of Ni-Zr alloy thin films with mixed nanocrystalline and amorphous structure,” *Thin Solid Films*, vol. 660, pp. 31–45, Aug. 2018, doi: 10.1016/j.tsf.2018.05.050.

[76] S. Veprek, “Recent search for new superhard materials: Go nano!,” *J. Vac. Sci. Technol. A Vacuum, Surfaces, Film.*, vol. 31, no. 5, p. 050822, Sep. 2013, doi: 10.1116/1.4818590.

[77] H. Zeman, J. Musil, and P. Zeman, “Physical and mechanical properties of sputtered Ta–Si–N films with a high (≥40 at %) content of Si,” *J. Vac. Sci. Technol.*

A Vacuum, Surfaces, Film., vol. 22, no. 3, p. 646, 2004, doi: 10.1116/1.1710499.

[78] J. Musil, R. Daniel, P. Zeman, and O. Takai, “Structure and properties of magnetron sputtered Zr-Si-N films with a high (≥25 at.%) Si content,” *Thin Solid Films*, vol. 478, no. 1–2, pp. 238–247, May 2005, doi: 10.1016/j.tsf.2004.11.190.

[79] J. Musil, P. Dohnal, and P. Zeman, “Physical properties and high-temperature oxidation resistance of sputtered Si3N4 MoNx nanocomposite coatings,” *J. Vac. Sci. Technol. B Microelectron. Nanom. Struct.*, vol. 23, no. 4, pp. 1568–1575, 2005, doi: 10.1116/1.1947798.

[80] J. Musil, R. Daniel, J. Soldán, and P. Zeman, “Properties of reactively sputtered W-Si-N films,” *Surf. Coatings Technol.*, vol. 200, no. 12–13, pp. 3886–3895, Mar. 2006, doi: 10.1016/j.surfcoat.2004.12.004.

[81] P. Zeman and J. Musil, “Difference in high-temperature oxidation resistance of amorphous Zr-Si-N and W-Si-N films with a high Si content,” *Appl. Surf. Sci.*, vol. 252, no. 23, pp. 8319–8325, Sep. 2006, doi: 10.1016/j.apsusc.2005.11.038.

[82] R. Daniel, J. Musil, P. Zeman, and C. Mitterer, “Thermal stability of magnetron sputtered Zr-Si-N films,” *Surf. Coatings Technol.*, vol. 201, no. 6, pp. 3368–3376, Dec. 2006, doi: 10.1016/j.surfcoat.2006.07.206.

[83] J. Musil, P. Zeman, and P. Dohnal, “Ti-Si-N films with a high content of Si,” in *Plasma Processes and Polymers*, 2007, vol. 4, no. SUPPL.1, doi: 10.1002/ppap.200731408.

[84] J. Musil and P. Zeman, “Hard a-Si3N4/MeNx nanocomposite coatings with high thermal stability and high oxidation resistance,” in *Solid State Phenomena*, 2007, vol. 127, pp. 31–36, doi: 10.4028/3-908451-33-7.31.

[85] J. Houška, J. Vlček, S. Hřeben, M. M. M. Bilek, and D. R. McKenzie, “Effect of B and the Si/C ratio on high-temperature stability of Si–B–C–N materials,” *EPL (Europhysics Lett.*, vol. 76, no. 3, p. 512, Oct. 2006, doi: 10.1209/EPL/I2006-10283-5.

[86] J. Houška, J. Vlček, Š. Potocký, and V. Peřina, “Influence of substrate bias voltage on structure and properties of hard Si-B-C-N films prepared by reactive magnetron sputtering,” *Diam. Relat. Mater.*, vol. 16, no. 1, pp. 29–36, Jan. 2007, doi: 10.1016/j.diamond.2006.03.012.

[87] Y. Wang, F. Cao, L. Shao, and M. – Hui Ding, “Diffusion barrier capability of Zr–Si films for copper metallization with different substrate bias voltage,” *Thin Solid Films*, vol. 517, pp. 5593–5596, 2009, doi: 10.1016/j.tsf.2009.01.001.

[88] D. Verma, D. Banerjee, and S. K. Mishra, “Effect of Silicon Content on the Microstructure and Mechanical Properties of Ti-Si-B-C Nanocomposite Hard Coatings,” *Metall. Mater. Trans. A Phys. Metall. Mater. Sci.*, vol. 50, no. 2, pp. 894–904, Feb. 2019, doi: 10.1007/s11661-018-5028-y.

[89] R. Hahn, A. Kirnbauer, M. Bartosik, S. Kolozsvári, and P. H. Mayrhofer, “Toughness of Si alloyed high-entropy nitride coatings,” *Mater. Lett.*, vol. 251, pp. 238–240, Sep. 2019, doi: 10.1016/j.matlet.2019.05.074.

[90] J. Musil *et al.*, “Properties of magnetron sputtered Al-Si-N thin films with a low and high Si content,” *Surf. Coatings Technol.*, vol. 202, no. 15, pp. 3485–3493, Apr. 2008, doi: 10.1016/j.surfcoat.2007.12.024.

[91] Soni, S. K. Sharma, and S. K. Mishra, “The effect of Si content on structural, mechanical and optical behaviour of magnetron sputtered Al–Si–N nanocomposite thin films,” *J. Alloys Compd.*, vol. 831, p. 154686, Aug. 2020, doi: 10.1016/j.jallcom.2020.154686.

[92] C. C. Chang, H. W. Chen, J. W. Lee, and J. G. Duh, “Influence of Si contents on tribological characteristics of CrAlSiN nanocomposite coatings,” in *Thin Solid Films*, Jun. 2015, vol. 584, pp. 46–51, doi: 10.1016/j.tsf.2015.02.022.

[93] J. F. Yang, B. Prakash, Y. Jiang, X. P. Wang, and Q. F. Fang, “Effect of Si content on the microstructure and mechanical properties of Mo-Al-Si-N coatings,” *Vacuum*, vol. 86, no. 12, pp. 2010–2013, Jul. 2012, doi: 10.1016/j.vacuum.2012.05.009.

[94] D. H. Jung, K. Il Moon, S. Y. Shin, and C. S. Lee, “Influence of ternary elements (X = Si, B, Cr) on TiAlN coating deposited by magnetron sputtering process with single alloying targets,” in *Thin Solid Films*, Nov. 2013, vol. 546, pp. 242–245, doi: 10.1016/j.tsf.2013.05.046.

[95] P. Mahato, R. J. Singh, and S. K. Mishra, “Nanocomposite Ti-Si-B-hard coatings deposited by magnetron sputtering: Oxidation and mechanical behaviour with temperature and duration of oxidation,” *Surf. Coatings Technol.*, vol. 288, pp. 230–240, Feb. 2016, doi: 10.1016/j.surfcoat.2016.01.039.

[96] R. E. Vernon, “Which elements are metalloids?,” *J. Chem. Educ.*, vol. 90, no. 12, pp. 1703–1707, Dec. 2013, doi: 10.1021/ed3008457.

[97] S. Yanagisawa, “Preparation of Molybdenum Silicide Films by Reactive Sputtering,” *J. Electrochem. Soc.*, vol. 127, no. 5, p. 1120, 1980, doi: 10.1149/1.2129830.

[98] T. Hara and M. Murota, “Interfacial reaction of Ta and Si rich tantalum silicides with Si substrate,” *J. Appl. Phys.*, vol. 68, no. 1, pp. 183–188, 1990, doi: 10.1063/1.347112.

[99] N. G. Galkin, S. V. Vavanova, A. M. Maslov, K. N. Galkin, A. V. Gerasimenko, and T. A. Kaidalova, “Solid phase growth and properties of Mg2Si films on Si(111),” *Thin Solid Films*, vol. 515, no. 22, pp. 8230–8236, Aug. 2007, doi: 10.1016/j.tsf.2007.02.049.

[100] Y. Zhan, X. Zhang, J. Hu, Q. Guo, and Y. Du, “Evolution of the microstructure and hardness of the Ti-Si alloys during high temperature heat-treatment,” *J. Alloys Compd.*, vol. 479, no. 1–2, pp. 246–251, Jun. 2009, doi: 10.1016/j.jallcom.2009.01.017.

[101] Y. Wang, F. Cao, M.-H. Ding, and L. Shao, “Evaluation of the barrier capability of Zr–Si films with different substrate temperature for Cu metallization,” *Appl. Surf. Sci.*, vol. 255, pp. 4738–4741, 2009, doi: 10.1016/j.apsusc.2008.08.082.

[102] H. M. Chen, F. Zheng, H. S. Liu, L. B. Liu, and Z. P. Jin, “Thermodynamic assessment of B–Zr and Si–Zr binary systems,” *J. Alloys Compd.*, vol. 468, no. 1, pp. 209–216, 2009, doi: 10.1016/j.jallcom.2008.01.061.

[103] S. Ogawa *et al.*, “Electrical Properties of (110)-Oriented Nondoped Mg 2 Si Films with p-Type Conduction Prepared by RF Magnetron Sputtering Method,” *J. Electron. Mater.*, vol. 43, no. 6, pp. 2269–2273, 2014, doi: 10.1007/s11664-014-3040-6.

[104] Y. Niu, L. Huang, C. Zhai, Y. Zeng, X. Zheng, and C. Ding, “Microstructure and thermal stability of TaSi2 coating fabricated by vacuum plasma spray,” *Surf. Coatings Technol.*, vol. 279, pp. 1–8, Oct. 2015, doi: 10.1016/j.surfcoat.2015.08.025.

[105] W. Jin *et al.*, “A high-flux-density hollow cathode plasma source for the studies on plasma surface interactions,” *Fusion Eng. Des.*, vol. 125, pp. 635–640, 2017, doi: 10.1016/j.fusengdes.2017.04.127.

[106] K. M. Sree Manu, S. Arun Kumar, T. P. D. Rajan, M. Riyas Mohammed, and B. C. Pai, “Effect of alumina nanoparticle on strengthening of Al-Si alloy through dendrite refinement, interfacial bonding and dislocation bowing,” *J. Alloys Compd.*, vol. 712, pp. 394–405, Jul. 2017, doi: 10.1016/j.jallcom.2017.04.104.

[107] F. Xu and D. Gong, “Improved the elevated temperature mechanical properties of Al-Si alloy deposited with Al-Si coating by magnetron sputtering,” *Vacuum*, vol.

150, pp. 1–7, Apr. 2018, doi: 10.1016/j.vacuum.2018.01.013.

[108] J. E. Mahan, A. Vantomme, G. Langouche, and J. P. Becker, “SemiconductingSi thin films prepared by molecular-beam epitaxy,” *Phys. Rev. B - Condens. Matter Mater. Phys.*, vol. 54, no. 23, pp. 16965–16971, 1996, doi: 10.1103/PhysRevB.54.16965.

[109] M. Naka, T. Shibayanagi, M. Maeda, S. Zhao, and H. Mori, “Formation and physical properties of Al base alloys by sputtering,” *Vacuum*, vol. 59, no. 1, pp. 252–259, 2000, doi: 10.1016/S0042-207X(00)00277-3.

[110] A. Vantomme, G. Langouche, J. E. Mahan, and J. P. Becker, “Growth mechanism and optical properties of semiconducting Mg2Si thin films,” *Microelectron. Eng.*, vol. 50, no. 1–4, pp. 237–242, 2000, doi: 10.1016/S0167-9317(99)00287-7.

[111] M. Naka, M. Maeda, T. Shibayanagi, H. Yuan, and H. Mori, “Formation and properties of Cr-Si sputtered alloys,” in *Vacuum*, May 2002, vol. 65, no. 3–4, pp. 503–507, doi: 10.1016/S0042-207X(01)00463-8.

[112] H. Inui, A. Fujii, T. Hashimoto, K. Tanaka, M. Yamaguchi, and K. Ishizuka, “Defect structures in TaSi2 thin films produced by co-sputtering,” *Acta Mater.*, vol. 51, no. 8, pp. 2285–2296, May 2003, doi: 10.1016/S1359-6454(03)00034-X.

[113] S. Lohfeld and M. Schütze, “Oxidation behaviour of particle reinforced MoSi2 composites at temperatures up to 1700°C part I: Literature review,” *Materials and Corrosion*, vol. 56, no. 2. pp. 93–97, Feb. 2005, doi: 10.1002/maco.200403831.

[114] T. Serikawa, M. Henmi, T. Yamaguchi, H. Oginuma, and K. Kondoh, “Depositions and microstructures of Mg-Si thin film by ion beam sputtering,” *Surf. Coatings Technol.*, vol. 200, no. 14–15, pp. 4233–4239, Apr. 2006, doi: 10.1016/j.surfcoat.2005.01.047.

[115] T. Serikawa, K. Kawabata, and K. Kondoh, “Comparative Study of Mg-Si Films Deposited by DC-and RF-Glow Discharge Sputtering,” *Trans. JWRI*, vol. 36, no. 2, pp. 39–43, 2007.

[116] G. G. Stoney, “The tension of metallic films deposited by electrolysis,” *Proc. R. Soc. London. Ser. A, Contain. Pap. a Math. Phys. Character*, vol. 82, no. 553, pp. 172–175, May 1909, doi: 10.1098/rspa.1909.0021.

[117] N. Guyot, Y. Harmand, and A. Mézin, “The role of the sample shape and size on the internal stress induced curvature of thin-film substrate systems,” *Int. J. Solids Struct.*, vol. 41, no. 18–19, pp. 5143–5154, Sep. 2004, doi: 10.1016/j.ijsolstr.2004.03.015.

[118] A. Mézin, “Coating internal stress measurement through the curvature method: A geometry-based criterion delimiting the relevance of Stoney’s formula,” *Surf. Coatings Technol.*, vol. 200, no. 18–19, pp. 5259–5267, May 2006, doi: 10.1016/j.surfcoat.2005.06.018.

[119] “ISO - ISO 14577-1:2015 - Metallic materials — Instrumented indentation test for hardness and materials parameters — Part 1: Test method.” https://www.iso.org/standard/56626.html (accessed Apr. 01, 2020).

[120] J. Berthonneau, C. G. Hoover, O. Grauby, A. Baronnet, R. J. M. Pellenq, and F. J. Ulm, “Crystal-chemistry control of the mechanical properties of 2:1 clay minerals,” *Appl. Clay Sci.*, vol. 143, pp. 387–398, Jul. 2017, doi: 10.1016/j.clay.2017.04.010.

[121] W. C. Oliver and G. M. Pharr, “An improved technique for determining hardness and elastic modulus using load and displacement sensing indentation experiments,” *J. Mater. Res.*, vol. 7, no. 6, pp. 1564–1583, Jun. 1992, doi: 10.1557/jmr.1992.1564.

[122] J. Musil, F. Kunc, H. Zeman, and H. Poláková, “Relationships between hardness, Young’s modulus and elastic recovery in hard nanocomposite coatings,” *Surf. Coatings Technol.*, vol. 154, no. 2–3, pp. 304–313, May 2002, doi: 10.1016/S0257-8972(01)01714-5.

[123] M. Jirout and J. Musil, “Effect of addition of Cu into ZrOx film on its properties,” *Surf. Coatings Technol.*, vol. 200, no. 24, pp. 6792–6800, Aug. 2006, doi: 10.1016/j.surfcoat.2005.10.022.

[124] R. F. Cook and G. M. Pharr, “Direct Observation and Analysis of Indentation Cracking in Glasses and Ceramics,” *J. Am. Ceram. Soc.*, vol. 73, no. 4, pp. 787–817, Apr. 1990, doi: 10.1111/j.1151-2916.1990.tb05119.x.

[125] T. Tölg, *Fyzikální praktikum*. ZČU, 2002.

[126] N. E. Hussey, K. Takenaka, and H. Takagi, “Universality of the Mott-Ioffe-Regel limit in metals,” *Philos. Mag.*, vol. 84, no. 27, pp. 2847–2864, Sep. 2004, doi: 10.1080/14786430410001716944.

[127] M. Gupta and N. M. L. Sharon, *Magnesium, Magnesium Alloys, and Magnesium Composites*. Wiley, 2011.

[128] J. Il Jang, M. J. Lance, S. Wen, T. Y. Tsui, and G. M. Pharr, “Indentation-induced phase transformations in silicon: Influences of load, rate and indenter angle on the transformation behavior,” *Acta Mater.*, vol. 53, no. 6, pp. 1759–1770, Apr. 2005,

doi: 10.1016/j.actamat.2004.12.025.

[129] J. Musil, V. Poulek, V. Valvoda, R. Kužel, H. A. Jehn, and M. E. Baumgärtner, "Relation of deposition conditions of Ti-N films prepared by d.c. magnetron sputtering to their microstructure and macrostress," *Surf. Coatings Technol.*, vol. 60, no. 1, pp. 484–488, 1993, doi: 10.1016/0257-8972(93)90137-D.

LIST OF THE AUTHOR'S PUBLICATIONS

Papers in international journals

1. J. Musil, S. Zenkin, R. Čerstvý, S. Haviar, **Z. Čiperová**, "(Zr,Ti,O) alloy films with enhanced hardness and resistance to cracking prepared by magnetron sputtering," Surface and Coatings Technology 322 (2017), 86–91, doi: 10.1016/j.surfcoat.2017.05.006.
2. J. Musil, Š. Kos, S. Zenkin, **Z. Čiperová**, D. Javdošňák, R. Čerstvý, "β- (Me_1, Me_2) and MeNx films deposited by magnetron sputtering: Novel heterostructural alloy and compound films," Surface and Coatings Technology 337 (2018), 75–81, doi: 10.1016/j.surfcoat.2017.12.057.
3. J. Musil, Š. Kos, M. Jaroš, R. Čerstvý, S. Haviar, S. Zenkin, **Z. Čiperová**, "Coating of overstoichiometric transition metal nitrides (TMN_x ($x > 1$)) by magnetron sputtering," Japanese Journal of Applied Physics 58 (2019), SAAD10-1-9, doi: 10.7567/1347-4065/aaec83.
4. J. Musil, **Z. Čiperová**, R. Čerstvý, S. Haviar: "Flexible hard Zr-Si alloy films prepared by magnetron sputtering," Thin Solid Films 688 (2019), 1-7, doi: 10.1016/j.tsf.2019.03.028.
5. J. Musil, **Z. Čiperová**, R. Čerstvý, Š. Kos, Š: "Hard alloy films with enhanced resistance to cracking," Vacuum (2021), in press, doi: 10.1016/j.vacuum.2021.110186.
6. J. Musil, Š. Kos, **Z. Čiperová**: "Effect of melting temperature T_m on properties of hard alloy coatings," prepared for publication (2021).

Participation at international conferences

Oral presentations at international conferences

1. J. Musil, Š. Kos, G. Remney, R. Čerstvý, S. Haviar, S. Zenkin, **Z. Čiperová**, M. Jaroš "Overstoichiometric transition-metal nitride coatings: Is magnetron sputtering a way to form hard dinitride coatings?," 10th Anniversary International Symposium on Advanced Plasma Science and its Applications for Nitrides and Nanomaterials/ 11th International Conference on Plasma-Nano Technology and Science (ISPlasma 2018/ IC-PLANTS 2018), Nagoya, Japan, March 4 – 8, 2018.

2. **Z. Čiperová**, J. Musil, S. Zenkin, R. Čerstvý, S. Haviar: "(Zr,Ti,O) alloy films with enhanced hardness and resistance to cracking prepared by magnetron sputtering," 17th Joint Vacuum Conference (JVC-17), Olomouc, Czech Republic, September 10 – 14, 2018.
3. **Z. Čiperová**, J. Musil, Š. Kos, M. Jaroš: " Overstoichiometric transition metal nitride films," 46th International Conference on Metallurgical Coatings and Thin Films (ICMCTF 2019), San Diego, CA, USA, May 19 – 24, 2019.
4. **Z. Čiperová**, J. Musil, R. Čerstvý, S. Haviar: "Flexible hard Zr-Si alloy films prepared by magnetron sputtering," European Congress and Exhibition on Advanced Materials and Processes (EUROMAT 2019), Stockholm, Sweden, September 1 – 5, 2019.
5. **Z. Čiperová**, J. Musil: " Hard alloy films with enhanced resistance to cracking," 18th International Conference on Thin Films and 18th Joint Vacuum Conference (ICTF-JVC 2020), Budapest, Hungary (online), November 22 – 26, 2020.

Poster presentations at international conferences

1. **Z. Čiperová**, J. Musil, S. Zenkin, R. Čerstvý, S. Haviar: "Hard (Zr,Ti) alloy films with small amount of oxygen resistant to cracking," 16th International Conference on Reactive Sputter Deposition (RSD 2017), Plzeň, Czech Republic, December 4 – 6, 2017.
2. **Z. Čiperová**, J. Musil, S. Zenkin, R. Čerstvý, S. Haviar: "Hard (Zr,Ti) alloy films with small amount of oxygen resistant to cracking," 16th International Conference on Plasma Surface Engineering (PSE 2018, September 17 - 21, 2018.
3. **Z. Čiperová**, J. Musil, Š. Kos, M. Jaroš: "Overstoichiometric $TMN_{x>1}$ transition metal nitride films," 10th International Conference on Fundamentals and Industrial Applications of HIPIMS and International Conference on Sputter Technology, Braunschweig, Germany, June 19 – 20, 2019.
   - winner of Young Scientist Awards for the best poster

ABSTRACT

The thesis is dedicated to magnetron sputtering of flexible hard alloy films, comprehension of the complicacy of their formation and the relation of the properties of the films with the deposition conditions. The text is divided into six chapters.

Chapter 1 is a general introduction and Chapter 2 gives a more detailed insight on magnetron sputtering, film growth and it explains the crucial terms for a present study: enhanced hardness and resistance to cracking, the energy of ion bombardment which is a very important parameter controlling the properties of the films, and it also introduces the problems of preparation of hard and flexible alloy films. Chapter 3 presents the aims of the thesis. Experimental details are given in Chapter 4 – it is explained how the deposition system works and what are its crucial parameters, and the thin film characterization used for this research is introduced.

The main part of the thesis is Chapter 5. It contains four individual studies which, altogether, deal with the problematics of the magnetron sputtering of the hard alloy films with enhanced resistance to cracking.

The first Subchapter 5.1 reports on the preparation of Zr-Si alloy films. It shows that Si-rich Zr-Si alloy films formed by a pulsed dual magnetron are hard with hardness $H \approx 20$ GPa, high ratio $H/E^* > 0.1$, elastic recovery $W_e > 60\%$, compressive macrostress ($\sigma < 0$) and dense, voids-free microstructure. These alloy films exhibit strongly enhanced resistance to cracking.

The second Subchapter 5.2 deals with sputtering of Mg-Si alloy films and with Mg-Si-N nitride films. Firstly, the experiments were done in order to confirm that the replacement of one metal element in a metal-metal alloy film by a metalloid is an effective way to increase its hardness and resistance to cracking as have been shown for the Zr-Si films. It turned out that the addition of Si to Mg is not sufficient, however, the further addition of N led to the formation of hard Mg-Si-N films with enhanced resistance to cracking.

Subsequently, the Si-N nitride films were produced and the complex study of their preparation and properties is given in Subchapter 5.3. The influence of substrate temperature and nitrogen partial pressure during the deposition on the elemental composition and mechanical properties of the Si-N films is investigated in detail. It is shown that Si-N films exhibit hardness up to 32 GPa and enhanced resistance to cracking.

Finally, the last Subchapter 5.4 connects the previous research by interpretation of the effect of homologous temperature T_S/T_m on the alloy film properties. The main finding is that the minimal value of $(T_S/T_m)_{min}$ of the curve T_S/T_m = f (elemental composition) determines an optimal elemental composition of the coating with a maximal hardness H_{max}. It is of key importance since it allows easy finding the correct elemental composition of the binary alloy films with H_{max}

Chapter 6 then summarizes the main conclusions of the presented studies. It is followed by the register of references used for this research and by the list of my publications and participation at international conferences.

ANOTACE

Tato dizertační práce se zabývá magnetronovým naprašováním tvrdých a zároveň flexibilních slitinových tenkých vrstev, porozumění problematiky jejich přípravy a vztahu mezi jejich vlastnostmi a depozičními podmínkami. Text dizertace je rozdělen do šesti kapitol.

Kapitola 1 je obecný úvod a obsahem Kapitoly 2 je detailnější pohled na magnetronové naprašování a růst tenkých vrstev. V této kapitole jsou vysvětleny základní pojmy důležité pro předkládanou práci: zvýšená tvrdost, odolnost vůči vzniku trhlin a energie iontového bombardu, což je velmi důležitý parameter pro řízení vlastností tenkých vrstev. Představuje také základní principy a omezení přípravy tvrdých flexibilních slitinových vrstev. V Kapitole 3 je seznam cílů dizertační práce. Experiment je popsán v Kapitole 4 – ta představuje depoziční aparaturu a její fungovaní, kritické parametry depozic a metody charakterizace tenkých vrstev potřebných pro tento výzkum.

Hlavní částí práce je Kapitola 5. Ta sestává ze čtyř samostaných studií, které se věnují problematice magnetronového naprašování tvrdých slitinových vrstev odolných vůči vzniku trhlin.

První Podkapitola 5.1 se věnuje slitinovýcm vrstvám Zr-Si. Je ukázáno, že Zr-Si vrstvy s vysokým podílem Si připravené pulzním duálním magnetronem mají vysokou tvrdost $H \approx 20$ GPa, vysoký podíl $H/E^* > 0.1$, elastickou vratnost $W_e > 60\%$, tlakové pnutí ($\sigma < 0$) a hustou mikrostrukturu bez pórů. Tyto slitinové vrstvy vykazují velmi zvýšenou odlnost vůči vzniku trhlin.

Druhá Podkapitola 5.2 pojednává o slitinových vrstvách Mg-Si a o nitridových vrstvách Mg-Si-N. První experimenty byly provedeny s účelem potvrzení zjištění z předchozí sutide Zr-Si vrstev, že nahrazení jednoho kovového prvku ve slitinové vrstvě sestávající ze dvou kovů polokovovým prvkem je účinný způsob ke zvýšení její tvrdosti a odolnosti vůči vzniku trhlin. Ukázalo se, že přidání Si k Mg není dostačující, ale přidání N vedlo k naprášení tvrdých Mg-Si-N vrstev se zvýšenou odolností vůči vzniku trhlin.

Následně byly vyrobeny Si-N nitridové vrstvy. Podkapitola 5.3 obsahuje komplexní studii jejich přípravy a vlastností. Prostor je věnován vlivu teploty substrátu a parciálnímu tlaku dusíku během depozice na prvkové složení a mechanické vlastnosti Si-N vrstev. Je ukázáno, že Si-N vrstvy dosahují tvrdosti až 32 GPa a zvýšené odolnosti vůču vzniku trhlin.

Poslední Pokapitola 5.4 interpretuje vliv homologické teploty T_S/T_m na vlastnosti slitinových vrstev a spojuje tak předchozí studie. Hlavním výsledkem je ukázaní, že minimální hodnota $(T_S/T_m)_{min}$ křivky T_S/T_m = f (prvkové složení) určuje optimální prvkové složení vrstvy s nejvyšší tvrdostí H_{max}. Toto zjištění je klíčové, protože dovoluje snadno nalézt správné prvkové složení binárních slitinovývh vrstev s nejvyšší dosažitelnou tvrdostí H_{max}.

Kapitola 6 shrnuje hlavní výsledky představených studiíí. Následuje seznam zdrojů a použité literatury a výčet mých publikací a účastí na mezinárodních konferencích.